Università degli Studi di Ferrara

UCA Universidad de Cádiz

INTERNATIONAL DOCTORAL COURSE IN
"EARTH AND MARINE SCIENCES (EMAS)"

CYCLE XXXVI

COORDINATOR Prof. PAOLO CIAVOLA

CHARACTERIZATION OF SUBMARINE GAS EMISSIONS

-

Scoglio d'Affrica case study

Scientific Disciplinary Sector (SDS) GEO/02

Candidate
Dott.ssa Anna Saroni

Supervisor
Prof.ssa Roberta Ivaldi

Co-Supervisor
Prof. Massimo Coltorti

Years 2020/2023

A Giorgia ed Elena, due grandi donne
che mi accompagnano nella vita

Acknowledgments

Prof. Massimo Coltorti per aver sempre creduto nella riuscita di questo lavoro.

Prof.ssa Roberta Ivaldi per l'entusiasmo e la fiducia riposta nei giovani.

Dott.ssa Federica Maurantonio per la collaborazione ed i dati di campionamento del 2022.

L'Istituto Idrografico della Marina Militare e l'Istituto di Ingegneria del Mare (INM) del CNR di Genova, per i dati forniti ed il supporto sia nei campionamenti che nelle successive elaborazioni.

Dott. Daniele Casalbore per i video forniti per la quantificazione del gas emesso e la disponibilità alla collaborazione.

Dott.ssa Martina Pierdomenico e dott. Daniele Spatola per la partecipazione attive alle campagne di campionamento.

Dott.ssa Alessandra Sciarra e dott. Marco Liuzzo per le revisioni costruttive.

Prof. Argnani Andrea per la curiosità dimostrata sull'argomento, la disponibilità al confronto e le valide osservazioni.

HYDRA Institute per aver reso fruibili le riprese del 2011.

Dott.ssa Sina Schorn e dott.ssa Jana Milucka per avermi introdotto al mondo della biogeochimica.

Prof. Paolo Ciavola, prof. Riccardo Caputo e prof. Michele Morsilli per le osservazioni costruttive ed i consigli.

Antonella Finotti, Giovanni Saroni ed Elena Saroni, per avermi sempre confortato e non avermi mai fatto mollare nei momenti più difficili.

Vadim Cebotari per la condivisione di sogni e aspirazioni ed il costante conforto.

Giorgia Zanellati per la pazienza, le risate e la convivenza nei momenti di stesura del lavoro.

Silvia Balzan per le esperienze condivise.

Grazie a tutti coloro che hanno contribuito in diversi modi a sostenermi in questo lavoro.

ABSTRACT

From 2017 to 2022, the Scoglio d'Affrica area located in the Northern Tyrrhenian sea had been surveyed and monitored after a transient event of gas and fluid emission from the seafloor that originated a geyser above the sea level. These transient phenomena occur very localized both in space and in extremely short time. The complexity of these kind of events requires an integrated monitoring system, which allows us to characterize the seafloor morphology and recent dynamics through a multidisciplinary research.

Seabed gas emission phenomena in the area were detected both by visual observations and by using a high resolution swath bathymetry. In addition, temperature, conductivity and salinity parameters of the water column were analyzed. The data collected identified new features of recent seafloor dynamics and gas emissions related to mud volcanism, obtaining in-depth information on the temporal and spatial evolution of seafloor morphology related to gas emissions in the area.

There are at least four mud volcanic structures in this area with different evolutionary records of the seafloor, including fracture formation, sediment consolidation and variation in seafloor morphology and depth. Bathymetric maps, 3D reproductions, and surface differences of the structures analyzed over the years were produced from multibeam acoustic echosounder data. Finally, thanks to available videos and direct observations of mud volcanoes, an estimate of methane emitted into the atmosphere from three emissive areas was assessed.

Morphological and vertical variations were identified in one of the four volcanoes. These were related to the origin and amount of gas emitted, showing that surface dynamics prevailed over deep dynamics. It was therefore possible to have an estimate of the volcano's inflation/deflation cycles due precisely to the mechanisms of mobilization of gas and mud in the subsurface, their outflow with consequent aggravation of the overlying load and creation of voids in the underlying sediments, as well as mud compaction and creation of overpressures.

Finally, the four identified mud volcanoes were schematized into three types of undersea features, conditioned by the surface dynamics of fluid upwelling and the state of mud volcanoes activity.

RIASSUNTO

Dal 2017 al 2022, l'area dello Scoglio d'Affrica nel Tirreno settentrionale, è stata investigata e monitorata in seguito ad un evento transitorio di emissione di gas e fluidi dal fondale marino che ha dato origine ad un geyser sopra il livello del mare. Questi fenomeni transitori si verificano in modo molto localizzato sia nello spazio che in tempi estremamente brevi. La complessità di questo tipo di eventi richiede un sistema di monitoraggio integrato, che permetta di caratterizzare la morfologia del fondo marino e le dinamiche recenti attraverso una ricerca multidisciplinare.

I fenomeni di emissione di gas dal fondale marino nell'area sono stati rilevati sia tramite osservazioni dirette che utilizzando un ecoscandaglio multifascio ad alta risoluzione. Inoltre, sono stati analizzati i parametri di temperatura, conduttività e salinità della colonna d'acqua. I dati raccolti hanno permesso di identificare nuove caratteristiche della dinamica recente del fondo marino e delle emissioni di gas legate al vulcanismo di fango, ottenendo informazioni approfondite sull'evoluzione temporale e spaziale della morfologia del fondale marino legata all'attività delle emissioni di gas nell'area.

In quest'area sono presenti almeno quattro strutture vulcaniche di fango con diversi record evolutivi di fondo, tra cui la formazione di fratture, il consolidamento dei sedimenti e la variazione della morfologia e della profondità del fondale. Mappe batimetriche, riproduzioni 3D e superfici differenziali delle strutture analizzate negli anni sono state prodotte grazie ai dati di ecoscandaglio acustico multifascio. Infine, grazie ai video disponibili ed alle osservazioni dirette dei vulcani di fango, è stato possibile valutare una stima del metano emesso in atmosfera da tre aree emissive.

Variazioni morfologiche e verticali sono state identificate in uno dei quattro vulcani. Queste sono state messe in relazione all'origine ed alla quantità di gas emesso, evidenziando come prevalgano dinamiche superficiali rispetto a quelle profonde. Si è pertanto potuto avere una stima dei cicli di inflazione/deflazione del vulcano dovuti appunto ai meccanismi di mobilitazione di gas e fango nel sottosuolo, alla loro fuoriuscita con conseguente aggravio del carico soprastante e creazione di vuoti nei sedimenti sottostanti, così come alla compattazione del fango ed alla creazione di sovrapressioni.

Infine, i quattro vulcani di fango individuati sono stati ricondotti a tre tipi di strutture sottomarine, condizionate dalle dinamiche superficiali di risalita dei fluidi e dallo stato di attività degli stessi.

TABLE OF CONTENTS

1. INTRODUCTION

1.1 Environmental implications

1.1.1 Methane as a greenhouse gas

International attention regarding the natural and anthropogenic forces contributing to climate change leads to an increasing need for monitoring and quantification of atmospheric gas emissions, with a focus on greenhouse gases such as CO_2 and CH_4. While the amounts of anthropic greenhouse gas emissions are fairly well defined and, according to the Intergovernmental Panel on Climate Change (IPCC), are responsible for the increasing in greenhouse gases in the atmosphere over the last 150 years, those produced in nature are, even today, very uncertain.

Atmospheric methane (CH_4), along with CO_2, is one of the most important greenhouse gases with a global warming potential of 25 CO_2-eq in 100 years (Capaccioni et al., 2015) and is emitted from a variety of sources both natural (e.g, wetlands, termites, oceans, freshwaters, emissions from deep reservoirs in both sedimentary and volcanic environments) and anthropogenic (e.g., rice fields, livestock farms, biomass burning, oil and gas extraction, landfills and waste dumps). The growth rate of this gas in the atmosphere is given by a balance between surface emissions and the oxidation process.

Especially regarding natural sources, which create about 36% of global methane emissions, there are still difficulties in attributing specific contributions to different sources, which may be biogenic or abiotic (Bousquet et al., 2006; Kirschke et al., 2013; Turner et al., 2017). The natural exhalation, or seepage, of CH_4 from the lithosphere is an important source for the atmosphere and it is comparable (from 27 to 63 $Tg(CH_4)\ yr^{-1}$) (Etiope and Schwietzke, 2019), if not higher, than other sources traditionally considered by the IPCC, such as biomass burning, termites and various industrial activities. Significant amounts of methane are in fact released by macro- and micro-seepage phenomena, spread at faults, mud volcanoes and submarine emissions. Geological emission represents the second most important natural source of CH_4, after wetlands (Kirschke et al., 2013).

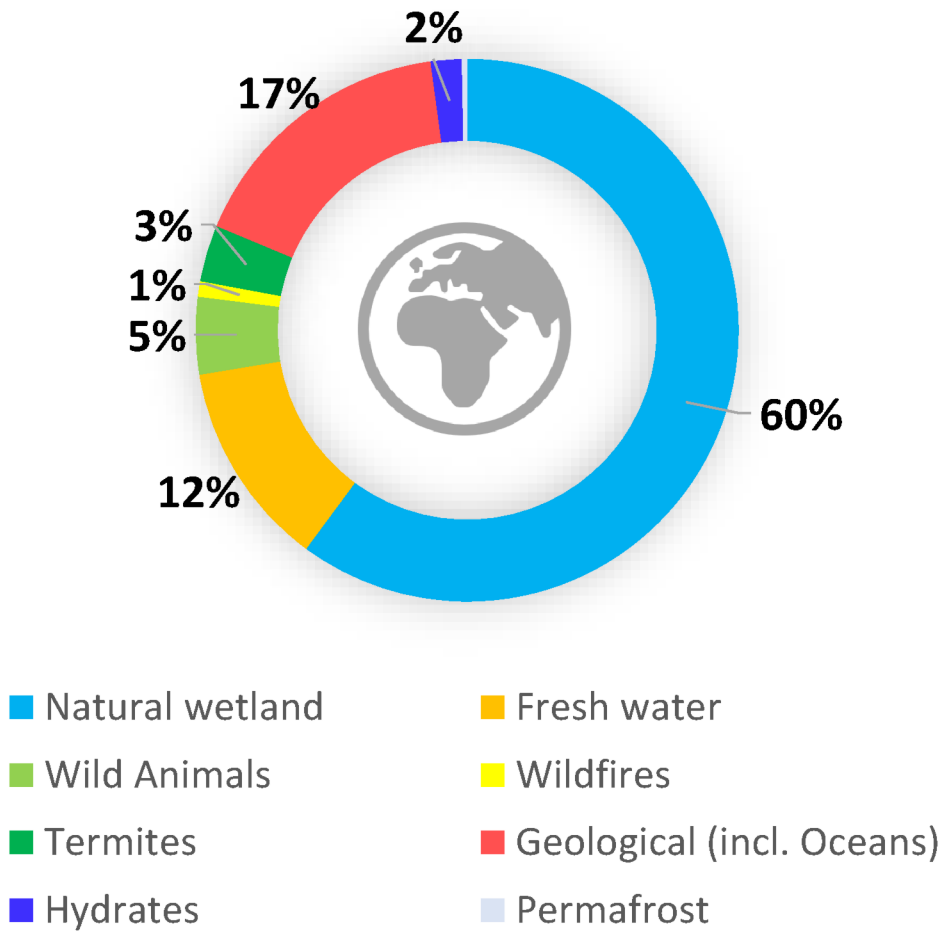

Figure 1 – CH_4 natural sources (data from Kirschke et al., 2013).

Sedimentary basins contribute 90% (Etiope and Klusman, 2002) of total geogenic methane emissions, while those associated with geothermal and volcanic events are less than 10% (Etiope et al., 2007). In fault zones, diffuse CH_4 emission from the soil can reach hundreds of mg m^{-2} d^{-1} (Etiope, 2009), preventing the biogeochemical oxidation process in the soil that would reduce it to CO_2 from taking place.

1.1.2 Submarine gas emissions contribution

Compared to surface emissions, marine emissions face additional difficulties in characterization, as the depth of the seafloor acts as an obstacle to the visibility and monitoring of gases. Additionally, some emissions occur intermittently with poor flow or change location over time, depending on primary (sediment type) or secondary (presence of fractures) permeability characteristics. In these cases, even manual sampling becomes challenging.

Due to these factors, the contribution of submarine gases to the global emission budget remains uncertain. Several studies state different range of emission regarding the global ocean CH_4 budget. Saunois et al. (2016) indicate a range between 5 to 25 Tg (CH_4) yr^{-1}, while

Rosentreter at al. (2021) indicate a range between 4.8 and 28.4 Tg (CH_4) yr^{-1}. Weber et al. (2019) reduce the range of total oceanic CH_4 emissions to 6-12 Tg yr^{-1}.

In particular, regarding mud volcanoes, the estimated total methane emissions emitted to the atmosphere from submarine mud volcanoes located far from the coast amount to 27 Tg yr^{-1} (Milkov et al., 2003; Judd, 2004). However, this value is subject to significant uncertainties, primarily because the total number of mud volcanoes worldwide and their temporal variability in relation to emissions are still unknown factors, as reported by a 2014 study conducted by Freseker et al.

There are also minor emissions that could make a notable contribution to the global emission context. For instance, CH_4 emissions from aquatic plant ecosystems are estimated to range between 0.09 and 2.7 Tg yr^{-1}, as stated by Garcias-Bonet and Duarte (2017). Additionally, abiotic methane produced through serpentinization mechanisms, may also contribute to overall emissions (Etiope and Sherwood Lollar, 2013).

1.2 Geological hazard: mud volcanoes

Under specific conditions, submarine emissions can pose geological hazards, especially when shallow water environments, ports, or fishing areas coincide with explosive eruptions. Mud volcanoes, in particular, have the potential to trigger explosive eruptions due to their process of formation that combines gas overpressure (resulting from high pore fluid pressure at significant depths) and the gravitative instability of shales (Niemann and Boetius, 2010; Mazzini and Etiope, 2017).

1.2.1 Activity, morphology and geology of mud volcanoes

Mud volcanoes, cone-shaped structures composed of sediment (mud), are formed in sedimentary basins through the fluidization of gas and water during their ascent through faults or fissures to the surface. Typically, mud volcanoes exist as a group of cones and crater systems rather than a single isolated cone (Mazzini and Etiope, 2017). The shape and size of these structures vary depending on factors such as the viscosity and density of the expelled material, the duration of eruption events, and the stage of development of the mud volcano (Niemann and Boetius, 2010). Consequently, mud volcanoes can exhibit a range of characteristics, including varying circumferences from a few meters to kilometers, plano-conical shapes that rise above the surface, or negative funnel-shaped forms. Their heights can span from a few decimeters to hundreds of meters.

In their comprehensive examination of mud volcanism, Mazzini and Etiope (2017) highlight four primary characteristics that define a mud volcano:

1. The expulsion of a three-phase system comprising gas, water, and sediment, occasionally including oil.

2. The presence of gas and saline water linked to a diagenetic or catagenetic hydrocarbon production system (accordingly gas is dominated by methane and subordinately C_{2+} hydrocarbons with low amounts of CO_2, N_2, He).
3. The involvement of sedimentary rocks exhibiting gravitational instability due to rapid sedimentation, resulting in the formation of mobile shales, diapirs, or diatremes.
4. The frequent occurrence of breccia within the material discharged by the mud volcano. The gas emitted by mud volcanoes is typically methane, originating either from microbial sources or as a result of thermogenic processes.

During the upwelling process, solid clasts can become incorporated along with the mud and fluids, resulting in the formation of "mud breccia," which stands out in contrast to the surrounding host sediments (Dimitrov, 2002). This mud breccia consists of a mixture of water, mud, and clasts of various sizes, representing a combination of different lithologies from various stratigraphic horizons that have been brecciated through the feeder channel (Mazzini and Etiope, 2017). These clasts can range in diameter from a few millimeters to more than 10 meters (Dimitrov, 2002).

When there is significant overpressure, a mud volcano undergoes a violent eruption, expelling large quantities of gas along with the mud breccia. These eruption conditions are periodically reached as the volcano accumulates increasing overpressure at depth. However, for the majority of their lifespan, mud volcanoes remain in a dormant or sleeping phase. During this period between eruptions, only gas and water seepages of variable intensity occur, including non-visible mini-seepage. Even when a mud volcano is considered extinct, eruptions cease, but weak gas seepage may persist (Mazzini and Etiope, 2017).

Mud volcanism is a result of various geological processes. Tectonic accretion and faulting play significant roles, while rapid sediment burial due to slope failures or high sedimentation rates, fluid emissions from mineral dehydration, as well as volcanic and seismic activities, also contribute to their formation (Dimitrov, 2002; Mellors et al., 2007; Milkov, 2000; Mazzini and Etiope, 2017).

Mud volcanoes can be found both onshore and offshore, distributed globally across active margins such as compressional zones of accretionary complexes, thrust and overthrust belts, passive margins, deep sedimentary basins associated with active plate boundaries, as well as delta regions or areas affected by salt diapirism (Dimitrov, 2002; Mazzini and Etiope, 2017 and references therein). Examples of offshore mud volcanoes can be observed in various locations including the Black Sea, the Gulf of Cadiz, the Caspian Sea, the Mediterranean Sea, the Gulf of Mexico, the Indian Ocean, the Caribbean Sea, the Norwegian Sea, the Atlantic Ocean, the Pacific Ocean, and the China Sea (Mazzini and Etiope, 2017 and references therein).

1.2.2 Gas chemistry

The prevalent compound of the gas released by mud volcanoes is usually methane, often above 80 vol%. Other minor gases are carbon dioxide (CO_2), nitrogen (N_2), alkanes (ethane to butane) and trace amounts of helium (He) (Milkov et al., 2003; Mazzini and Etiope, 2017).

As a hydrocarbon gas, molecular and isotopic composition is a diagnostic method to interpret the origin of the gas, its maturity (generation temperature or thermal stress) and alterations (fig. 2). In particular, the genetic diagrams use molecular ratios of alkanes (methane CH_4 or C_1, ethane C_2H_6 or C_2, propane C_3H_8 or C_3), stable carbon ($^{12}C/^{13}C$ or $\delta^{13}C$) and hydrogen ($^{1}H/^{2}H$ or $\delta^{2}H$) isotope composition of C_1 and $\delta^{13}C$ of carbon dioxide (CO_2) (Milkov and Etiope, 2018; Etiope and Sherwood Lollar, 2013). The standards they refer to are VPDB (Vienna Pee Dee Belemnite) and VSMOW (Vienna Standard Mean Ocean Water). These binary diagrams include $\delta^{13}C$ -C_1 versus $C_1/(C_2 + C_3)$ proposed by Bernard et al. (1977), $\delta^{13}C$-C_1 versus $\delta^{2}H$-C_1 proposed by Schoell (1983) and Whiticar et al. (1986), and $\delta^{13}C$-C_1 versus $\delta^{13}C$-CO_2 proposed by Gutsalo and Plotnikov (1981). A recent revision on these genetic diagrams was proposed by Milkov and Etiope in 2018, considering an expanded dataset and the different processes that can alter the composition of the gas.

Global dataset of analysed gas from onshore mud volcanoes show that they are mostly of thermogenic origin (76%), that means they are produced by thermal degradation of organic matter or oil cracking (catagenesis) in relatively deep sediments at temperatures typically up to 230–240 °C ($\delta^{13}C$-$CH_4 \approx -46.4$‰ VPDB as average of 201 mud volcanoes) (Etiope et al., 2009a).
Microbial contribution is extremely low (4%) and the rest is of mixed origins (20%) (Etiope et al., 2009a). Microbial gas is produced at lower temperature and in more recent or shallower sediments (diagenesis) by methanogenic microbes.

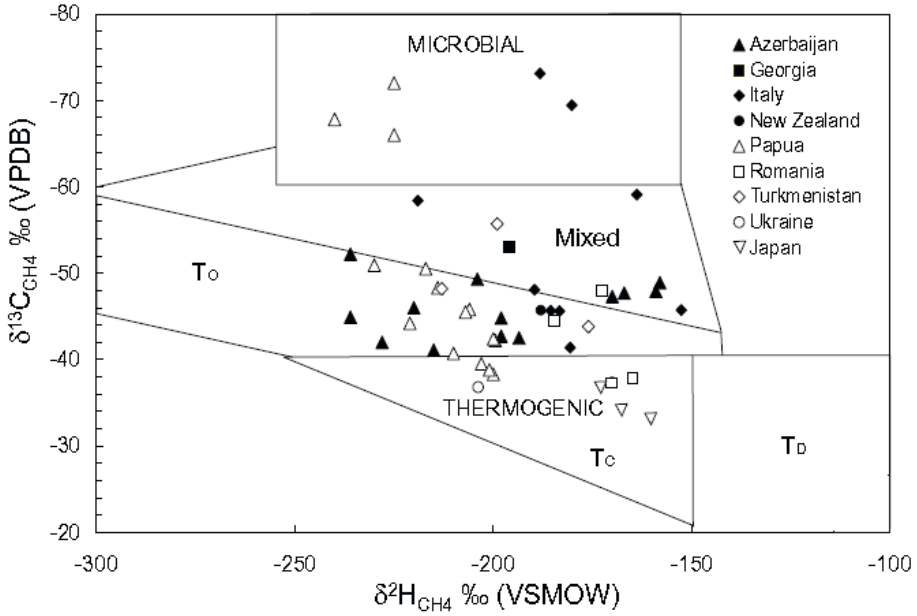

Figure 2 - Stable C and H isotope composition of methane released from MV worldwide (from Mazzini and Etiope, 2017). TO: thermogenic with oil; TC: thermogenic with condensate; TD: dry thermogenic.

Regarding mud volcanoes, the gas that reach the surface has no difference in isotopic composition, but for slow degassing mud volcanoes it has less ethane and propane (i.e., it is dryer, with a higher $C_1/(C_2+C_3)$ ratio) than the one originated in the reservoir. This happens because ascending gas significantly interacts (with longer residence times) with water and sediments or because a secondary methanogenesis occurs, following oil biodegradation, increasing C_1. Vigorous and erupting mud volcanoes, instead, have the same molecular composition of reservoir gas (Etiope et al., 2009a).

Another important characteristic of mud volcano gas is the frequent occurrence of CO_2 with positive $\delta^{13}C$ values, often >5‰ VPDB (heavy CO_2), together with a ^{13}C enrichment in C_2+ alkanes. This is due to petroleum biodegradation. During this process, microorganisms gradually destroy n-paraffins (n-alkanes or normal alkanes) and oil density and viscosity increase. Following that, residual and heavy CO_2 is obtained after consumption by secondary methanogenesis in relatively shallow (<2000 m deep) reservoirs (Etiope et al., 2009b and references therein; Mazzini and Etiope, 2017).

1.2.3 Acoustic investigations

Detecting submarine gas emissions using acoustic investigation is a valuable scientific approach that offers insights into the behavior and distribution of gas seeps in the marine environment (Krylov, A. A. et al., 2023). Acoustic techniques, such as multibeam echosounders and sub-bottom profilers, provide a non-invasive means of remotely detecting and mapping gas seep locations and their associated geological structures. These methods rely on the detection and analysis of acoustic signals reflected or refracted by gas bubbles or gas-saturated sediments.

Multibeam echosounders, with their high-resolution bathymetric capabilities, are one of the reliable techniques to identify and investigate submarine mud volcanoes, together with mud diapirs, brine lakes and pools and pockmark fields. By measuring the backscattered intensity of the acoustic signals, it is possible to distinguish areas with high gas content from surrounding sediments. Sub-bottom profilers, on the other hand, utilize low-frequency sound waves that penetrate into the sediment layers beneath the seafloor. By analyzing the reflected signals, these profilers can identify acoustic anomalies associated with gas-filled layers or subsurface gas accumulations.

The existence of mud volcanoes or other centers of fluid/mud expulsion can often be inferred from the presence of distinct local topographic features characterized by unique relief and strong acoustic backscatter signals (Milkov, 2000). In various studies conducted in the Mediterranean Sea and the Gulf of Cadiz, significant patches of high acoustic backscatter have been observed, indicating the presence of mud volcanoes (e.g., Fusi and Kenyon 1996; Volgin and Woodside 1996; Sautkin et al. 2003; Huguen et al. 2004; Lykousis et al. 2009; Dupré et al. 2010; Mascle et al., 2014).

The strength of backscatter signals is influenced by sediment properties, including composition and micro-relief. Mud breccias, which contain clasts, gas bubbles, irregular mudflows, and exhibit bioactivity, are particularly effective in generating high backscatter intensities (Mascle et al., 2014).

Acoustic techniques provide a means of monitoring gas seep activity over time and identifying temporal variations in gas release and seabed morphology (Foucher et al., 2010; Feseker et al., 2014). Furthermore, acoustic methods can be complemented with additional sensors, such as underwater cameras or gas sensors, to enhance the characterization of gas seep features. Acoustic imaging combined with visual observations can provide a comprehensive understanding of seafloor gas seepage and its relation to seafloor geomorphology. This non-invasive approach provides valuable insights into the dynamics of gas seepage, contributing to our understanding of gas fluxes in the marine environment and their implications for biogeochemical processes, climate, and geohazard assessment.

1.3 Scope of work

This project involves the study and geochemical monitoring of gaseous manifestations present near the Scoglio d'Affrica in the Tyrrhenian Sea, where mud volcanoes (MVs) have been detected at shallow depths. This shallow-water setting is an ideal field for experimentation because many of the seeps are at depths that can be safely reached by divers, allowing to test and validate monitoring techniques which can then also be applied to deep-water environments.

The goal is to investigate the surface expression of the shallow water MVs, with a focus on the more recent active one. Field data collected at the surface of the MVs during 2017, 2018, 2019 and 2022 are compared, bringing evidence of and discuss changes in the morphology and fluid activity over five years. The high-resolution data available allow to

study the more recent and present-day extrusive activity, possibly representative of the past and the future, and to make an estimation of the volumes of gas and mud potentially extruded by individual MVs. A conceptual model is proposed to explain the observed structures of the Scoglio d'Affrica MVs, their involved fluid sources and their development over time.

2. SCOGLIO D'AFFRICA CASE STUDY

2.1 Geological overview

The Northern Apennine Orogeny, which began in the late Eocene due to the convergence resulting from the closure of the Tethys Ocean (Carminati and Doglioni, 2012), is closely connected to the geological past of the Northern Tyrrhenian Sea. Following this collision, an extensive tectonic regime gained prominence over time. The interior section of the Apenninic orogenic belt underwent stretching, enabling the formation of the Tyrrhenian Basin and the generation and ascent of anatectic melts caused by the uplift of the asthenospheric mantle (Pandeli et al., 2013). Various magmatic bodies formed on several islands in the Northern Tyrrhenian Sea, including Capraia (between ~7.2 and ~4.8 Ma; Carminati and Doglioni, 2012), western and eastern Elba, Montecristo (~7.1 Ma; Carminati and Doglioni, 2012), and Giglio (~5 Ma; Carminati and Doglioni, 2012). These volcanic formations, along with the mainland Tuscany, constitute the Tuscan Magmatic Province. The stretching of the crust in the Northern Tyrrhenian Sea resulted in the creation of consistently oriented normal fault systems with north-south and northwest-southeast trends (Keller and Coward, 1996 and references therein). These faults delineate various small Neogene sedimentary basins surrounded by structural ridges, which are characteristic of the Tuscan shelf (Pascucci et al., 1999). The most tectonically active area is the Elba-Pianosa Ridge, an uplifting anticline oriented in a north-south direction that separates the Tuscan shelf from the Corsica basin (fig. 3). The Elba Pianosa Ridge has uplifted because of the intrusion by volcanic and granitic rocks that led to an uplift of sedimentary layers (e.g. Pianosa Island). The Messinian deposits on both the western and eastern flanks of the ridge show signs of tilting due to the Messinian–early Pliocene uplift (Mauffret et al., 1999). Nevertheless, the structure of the Pianosa Ridge is intricate, and the uplift is also attributed to Miocene compressional tectonics.
The Corsica basin is filled with sedimentary deposits dating from the Eocene to the present, accumulating to a thickness of about 8.5 kilometers (Mauffret et al., 1999).

The study area lies within the Elba-Pianosa Ridge, which emerges above the sea surface at Pianosa Island and Scoglio d'Affrica. The ridge comprises a thick (over 3000 meters) siliciclastic succession from the Eocene-Oligocene, where gas pockets were discovered in Eocene, Oligocene, and Miocene turbiditic deposits during AGIP drilling projects in the 1970s and 1980s. The two wells, Martina 1 (–3,296 m) and Mimosa 1 (–3,826 m) drilled by AGIP on the Elba-Pianosa Ridge revealed four depositional units, all separated by

unconformities (Z, X, A, B) recognized by truncation in seismic stratigraphic analysis (Cornamusini et al., 2002; Cornamusini and Pascucci, 2014; fig. 4):

1. SUB 1 is early to middle Eocene.
2. SUB 2 are Oligocene strata that overlain Sub 1.
3. LIT 0 are late Burdigalian deposits that overlain the Oligocene strata in the well Martina 1.
4. LIT 7 are Pleistocene sediments. They overlain Oligocene strata in Mimosa well and Miocene deposits in Martina well.

Pre-Eocene substrate is not possible to determine. The seismic Line M12 B that crosses the Scoglio d'Affrica Islet (fig. 5) and seismic Line T1 (fig. 6) show a chaotic or quasi-transparent seismic facies, similar to that defined by Pascucci et al. (1999) for Jurassic limestones of the Tuscan Nappe.

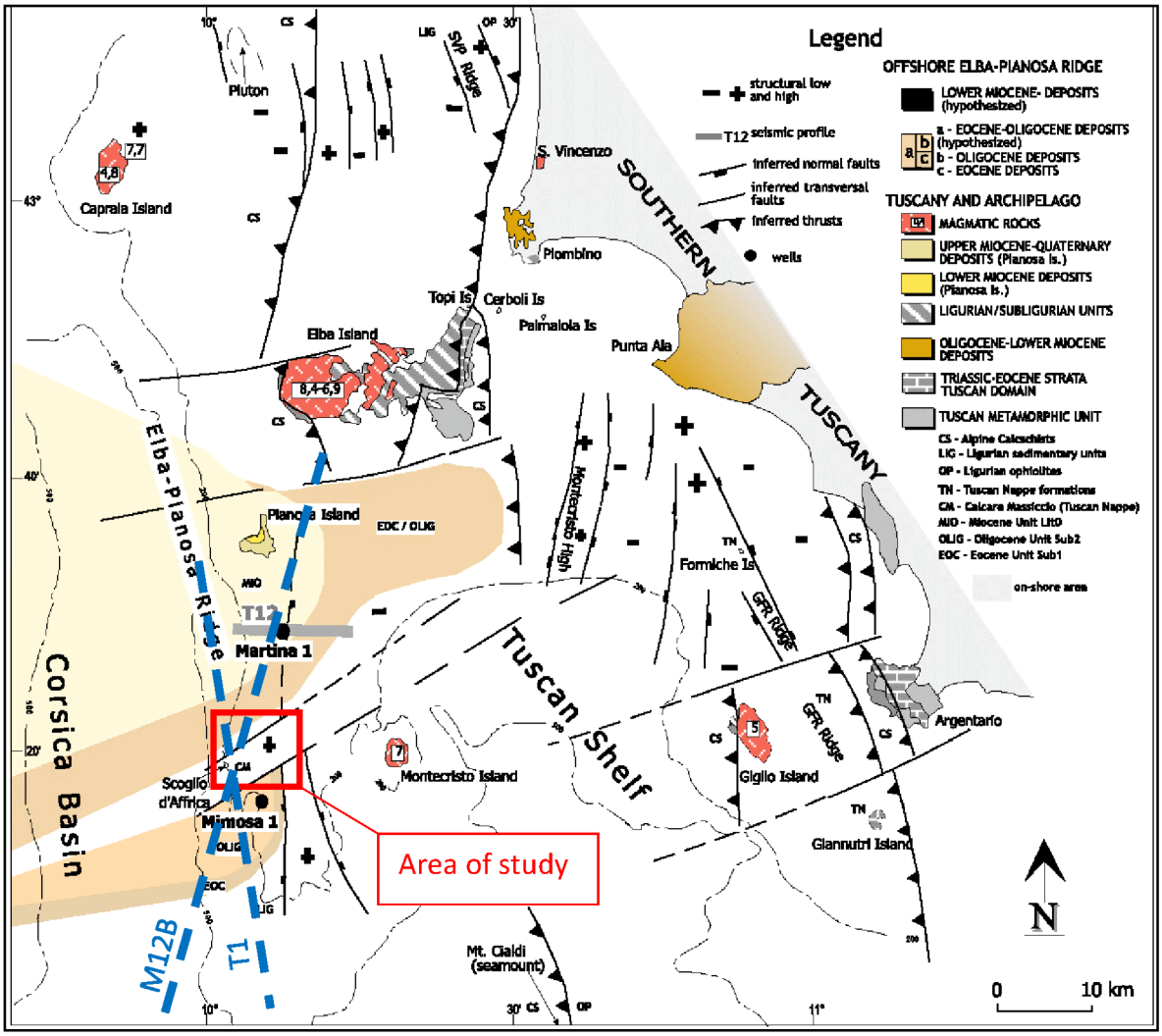

Figure 3 - Structural scheme of the northern Tyrrhenian Sea, distribution of Eocene, Oligocene, and Miocene deposits and location of Martina 1 and Mimosa 1 wells. Dashed blue lines are CROP-Mare 12B and industrial seismic profile Line T1 (Cornamusini and Pascucci, 2014).

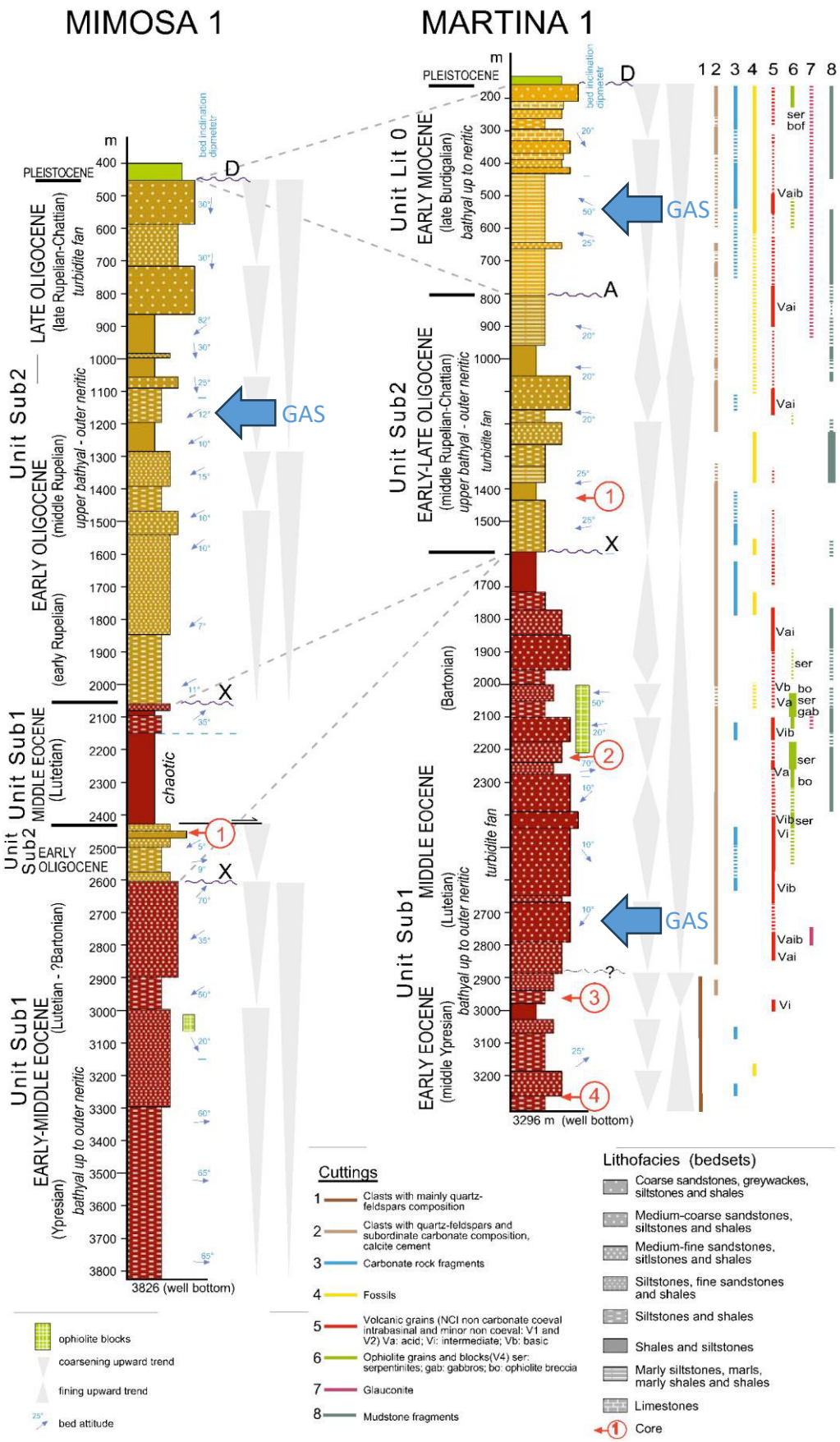

Figure 4 - Synthetic stratigraphy of the two wells Mimosa 1 and Martina 1, showing the unconformity bounded units, the lithofacies and the distributions of the marker granules or fragments as recognized from the cutting analysis (ser, serpentinites; bo, ophiolitic breccias; gab, gab- bros; Va, acid volcanites; Vi, intermediate volcanites; Vb, basic volcanites). Main seismic unconformities (after Cornamusini et al., 2002): X at the base of the Unit Sub2; A at the

base of the Unit Lit0; D at the base of the Unit Lit7 (from Cornamusini and Pascucci, 2014). Blu arrows indicate gas presence.

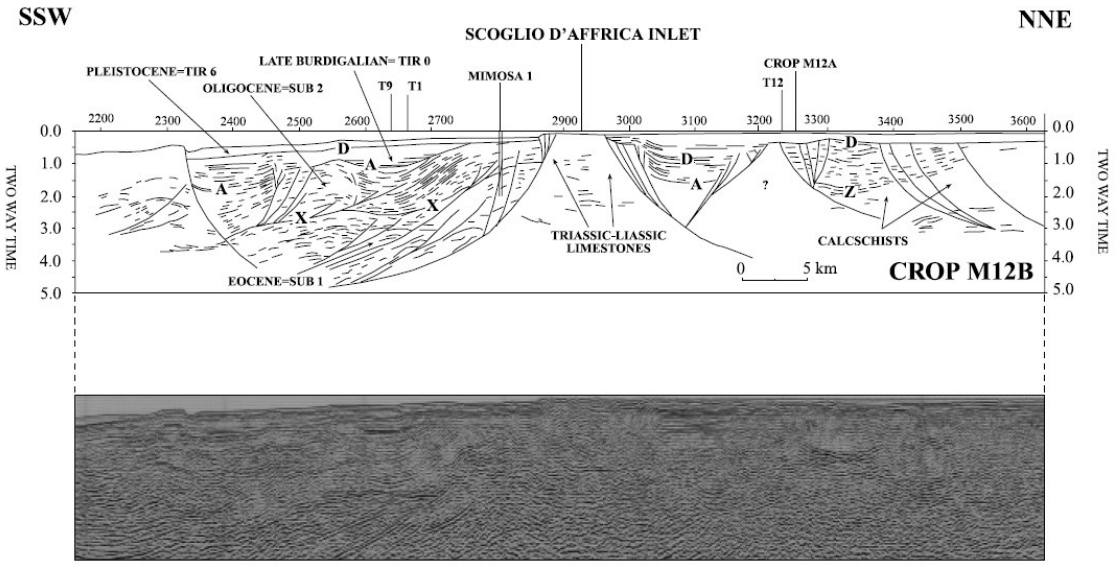

Figure 5 - Line drawing and original of the migrated CROP M12B profile (from Cornamusini et al., 2002). Z=bottom of the Eocene strata; X=bottom of Oligocene strata; A=bottom of late Burdigalian-?Serravallian strata; B=bottom of late Miocene-Presents deposits. Location is in fig. 3.

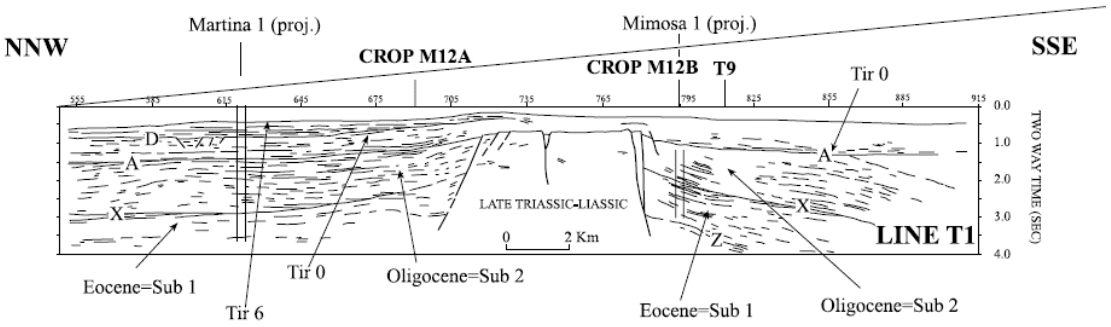

Figure 6 – Line drawing of the seismic profile Line T1 (after Lazzarotto et al., 1995). Z=bottom of Eocene Sub 1 strata; X=bottom of Oligocene Sub 2 strata; A=bottom of late Burdigalian-?Serravallian Tir 0 strata; B=bottom of late Tortonian-Messin ian Tir 2 deposits; C=bottom of Pliocene Tir 4/5 deposits; D=base of Quaternary Tir 6 deposits (from Cornamusini et al., 2002). Location is in fig. 3.

Pianosa Island consists of Lower Miocene (Burdigalian) to Pleistocene shallow marine and continental deposits, such as the Marina del Marchese, Golfo della Botte, and Pianosa Formations (Cornamusini et al., 2002 and references therein). On the other hand, Scoglio d'Affrica is composed of shallow marine organic limestone with abundant algal components and frequent malacofauna. These sediments are dated from the Pleistocene to Holocene, corresponding to the age of the Tuscan Nappe (Motteran and Ventura, 2005). Two specific lithofacies were identified, both associated with high-energy environments: packstones-wackestones, representing a seashore depositional environment, and coral lithofacies (grainstone) situated above the former lithofacies (Motteran and Ventura, 2005). These sediment layers are mostly horizontal and form a transgressive sequence over the carbonate rocks of the Tuscan Nappe (Cornamusini et al., 2002). Cornamusini et al. (2002) also indicate the presence of high-angle normal faults bordering the islet, which were active during post-Burdigalian time. Regarding the seafloor around Scoglio d'Affrica,

morphological terraces, faults and methane activity had already been reported by Barletta et al. (1969).

2.2 Geomorphological overview

Scoglio d'Affrica MV consists of a group of mounds and cones systems that extend in an area of about 24 km^2 on a N-S elongated ridge at a medium of -25 m water depth. Three morphological highs with conical shape associated to methane emissions are already documented in literature (see mounds 1, 2 and 3 in fig. 7, Meister et al., 2018; Casalbore et al., 2020; Saroni et al., 2020). These are shallow water areas with conical shape rising above the surface reaching up to -7 m depth and characterized by the presence of blocks and mud. During 2019 campaign, another mound was identified, located south of the previous ones, at a depth of about -15 m (mound 4).

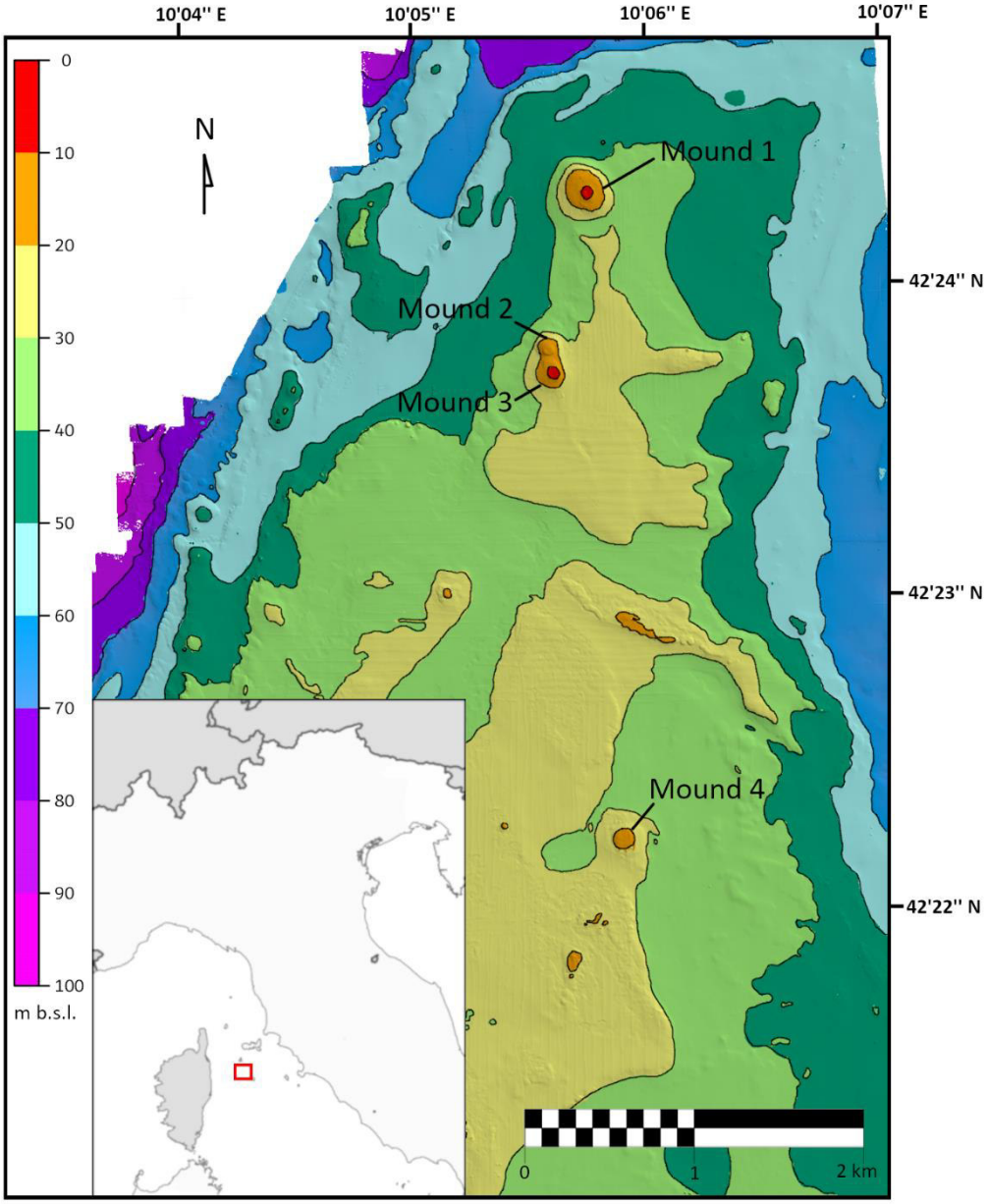

Figure 7 - Reproduction of bathymetry by multibeam echosounder from 2019 campaign.

According to literature (e.g. Saroni et al., 2020; Casalbore et al., 2020; Ferretti et al., 2021; Spatola et al., 2022) five main seafloor morphological features can be identified in the area (fig. 8). These features are associated with tectonic, fluid-related and erosive-depositional processes:

1. Escarpments
2. Ridges
3. Morphological highs
4. Pockmarks
5. Channelised features

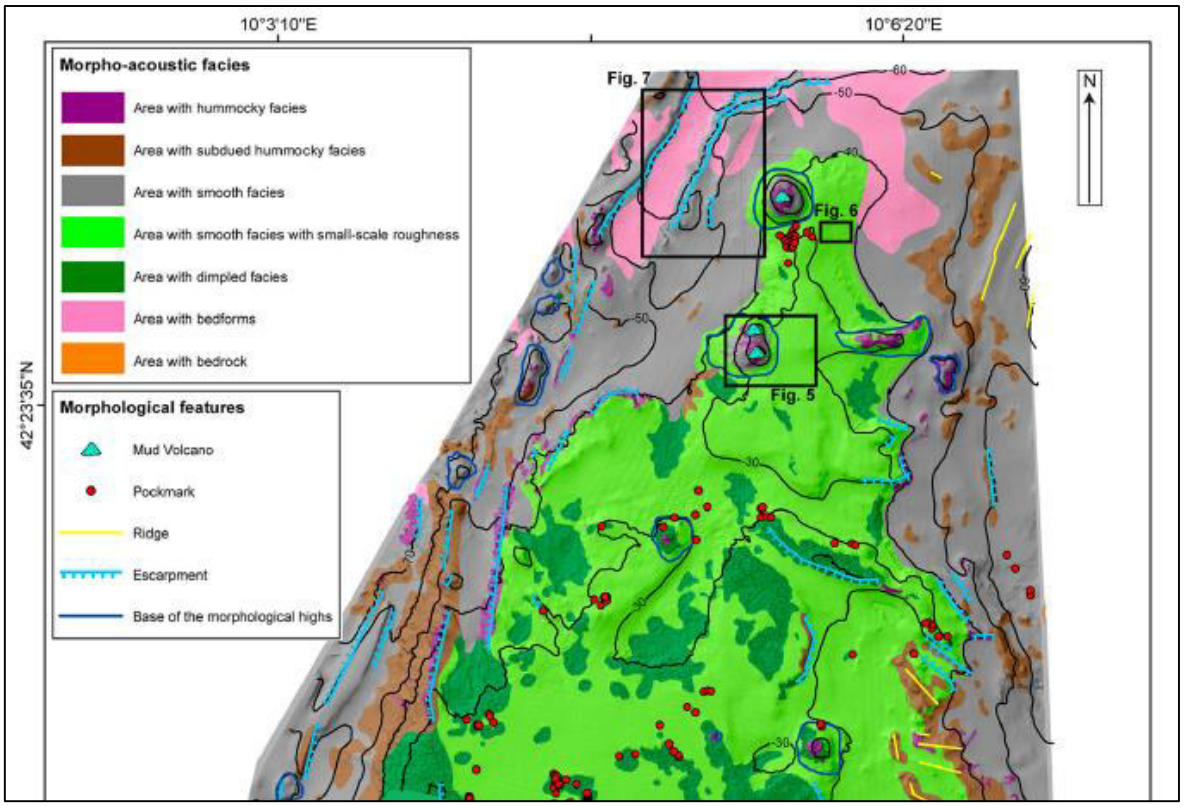

Figure 8 – Extract of the bathy-morphologic map of the offshore sector around the Scoglio d'Affrica islet, showing the main morpho-acoustic facies and morphological features identified by Spatola et al. 2022.

2.3 Gas chemistry

According to Saroni et al. (2020), methane is the dominant gas component emitted from the mud volcano, comprising approximately 95.5% to 96.82% of the total volume. Other gases present include carbon dioxide (0.97% to 1.30%), nitrogen (0.41% to 0.84%), ethane (0.026% to 0.036%), and helium (up to 0.0046%). The $CH_4/(C_2H_6+C_3H_8)$ ratio ranges from from ~2670 to ~3700, indicating significantly high values compared to most thermogenic gases. Low C_1/C_{2+} ratios (<103) clearly indicate the contribution of thermogenic hydrocarbons in the fluids, while higher C_1/C_{2+} ratios (>103) do not exclude the involvement of thermogenic hydrocarbons (Bernard et al., 1978; Kim et al., 2012).

The isotopic composition of CH_4 shows a narrow range of variation in the samples (fig. 9). The δ^2HCH_4 values range from -163 to -168‰ vs VSMOW, while the $\delta^{13}CCH_4$ values range from -34.9 to -36.8‰ vs VPDB. CO_2 exhibits a significant enrichment in heavy carbon isotopes, with $\delta^{13}CCO_2$ ranging from +15.3 to +21.7‰ vs VPDB. The $^3He/^4He$ ratios, normalized to the atmospheric ratio (denoted as Ra = $1.39 \cdot 10^{-6}$ Mamyrin and Tolstikhin, 1984; Clarke et al., 1976; Sano et al., 2008; Mabry et al., 2013), are consistent among all the gas seeps, measuring 0.01 Ra. The $^4He/^{20}Ne$ ratios, ranging from 75 to approximately 330, are at least two orders of magnitude higher than the air ratio ($^4He/^{20}Ne$ = 0.318 Sano and Wakita, 1985), indicating a minimal contribution from atmospheric gas. The $CH_4/^3He$ ratios vary from $1.24 \cdot 10^{12}$ to $1.76 \cdot 10^{12}$.

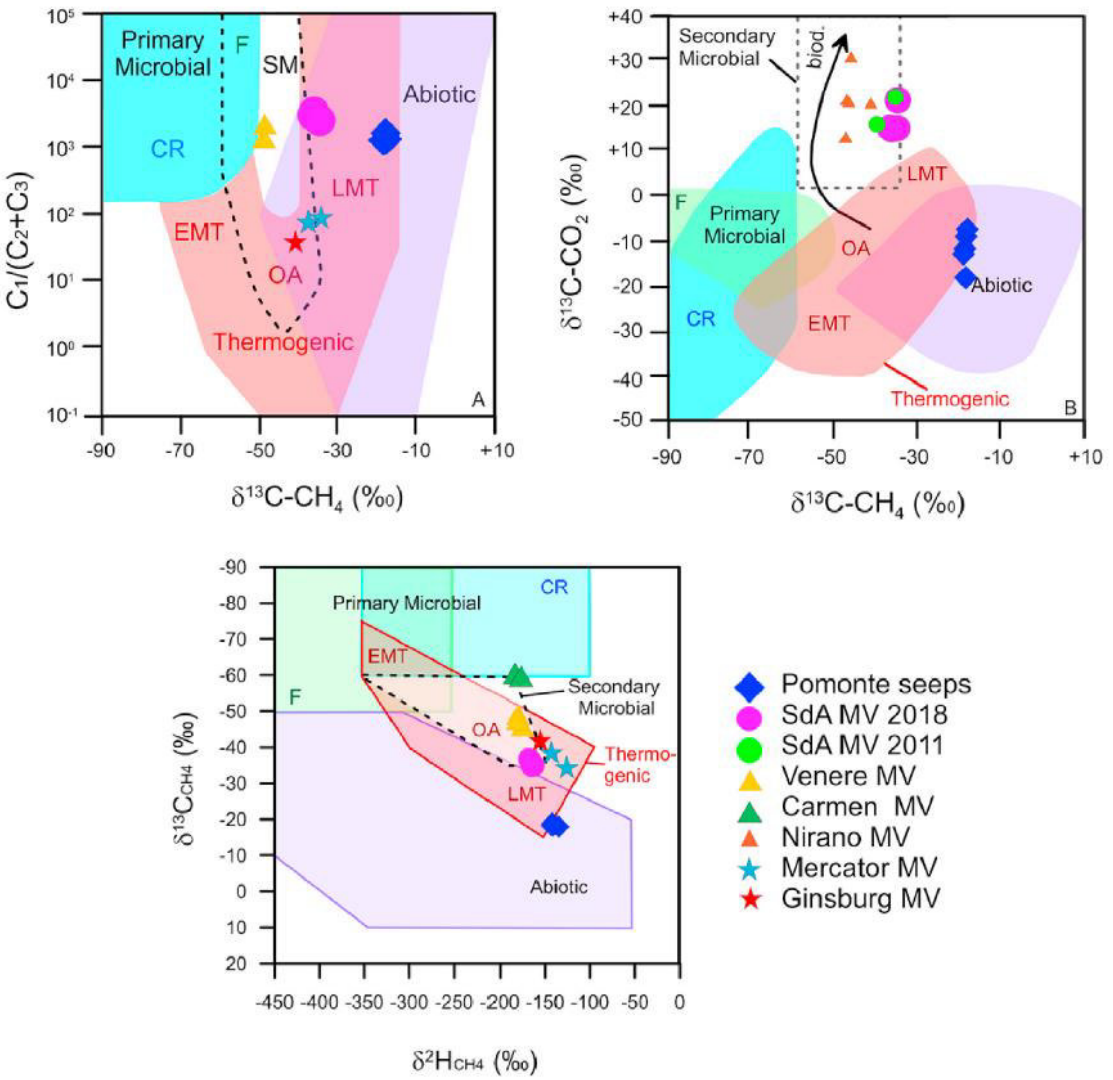

Figure 9 - A, B, C: Scoglio d'Affrica mud volcano 2018 gas (SdA MV 2018) compared with 2011 (Meister et al., 2018) and Pomonte gases (Sciarra et al., 2019), together with other MVs gases from literature, inserted into the revised genetic diagrams from Milkov and Etiope (2018) (from Saroni et al., 2020)

3. DETECTION TECHNIQUES

3.1 Idro-oceanographic campaigns

In this study data from four idro-oceanographic campaigns are compared. The campaigns were organized in collaboration with the University of Ferrara, Marina Militare Italiana, Istituto Nazionale di Geofisica e Vulcanologia (INGV) Roma, INGV Palermo, Istituto di Ingegneria del Mare (INM) of the Consiglio Nazionale delle Ricerche (CNR) in Genova, the University of Rome.

Table 1 – Idro-oceanographic campaigns.

	2017 campaign	2018 campaign	2019 campaign	2022 campaign
Date	From 23/06/2017 to 30/07/2017	From 19/06/2018 to 30/07/2018	From 04/06/2019 to 17/06/2019	From 22/07/2022 to 24/07/2022
Ship	Nave Aretusa MBN 1206	Nave Aretusa MBN 1206	Nave Magnaghi	Nave Galatea
Multibeam	Konsberg EM 2040 and Konsberg EM 2040C	Konsberg EM 2040 and Konsberg EM 2040C	Konsberg EM 2040 and Konsberg EM 2040C	Konsberg EM 2040

3.2 Multibeam echosounder EM2040

The seafloor mapping, water column analysis, and seabed characterization were conducted using a Multibeam EM2040 Kongsberg Echosounder with a 75% and 50% overlap, an ideal tool for any high resolution mapping and inspection application. This technology allows to ensure the minimum standards required by the IHO (International Hydrographic Organization) publication S-44. The EM 2040 has a frequency range of 200-400 kHz: for the purpose of the survey the 400 kHz was used: it is provided for inspection work with the utmost resolution, with the simultaneous acquisition of water column and backscatter data. The Seafloor Information System and CARIS HIPS & SIPS 4.3 were utilized as interfacing and post-processing software respectively.

The multibeam echosounder is a specialized sonar system employed to gather information about the seafloor. It emits sound waves in a fan-shaped pulse beneath the ship's hull. Its functioning is based on the measuring of the travel time of the sound waves from the emitter to the seabed and back to the receiver. Beamforming techniques are utilized to extract directional information from the returning soundwaves, allowing for the generation of a swath of depth readings from a single pulse. This technology enables the determination of water depth and the detection of disturbances in the water column caused by variations in density, such as fish aggregations or gas emissions. The basic

components of the system include a transmit transducer, a receive transducer, a processing unit, and a hydrographic workstation.

3.2.1 Estimated error

The Total Propagated Uncertainty (TPU) considers the estimated error of each measured parameter (v_S, tide, attitude, measurement of distance and angles, movement, offsets, squats, etc.). It is expressed as a dimensional value separated into its horizontal components (THU) and vertical (TVU) one of which publication S-44 "IHO Standards for Hydrographic Surveys" (Edition 6.1.0, September 2022) indicates the limits for the various survey orders.

The vertical uncertainty of the surveys carried out is around an average of 0.4 meters with a standard deviation of 0.1 m.

3.3 CTD multiparameter probe (conductivity, temperature, depth)

CTD stands for conductivity, temperature, and depth, and refers to probes used to detect how the conductivity and temperature of water changes relative to depth. They consist of sensors to measure water pH, oxygen, nitrate and chlorophyll levels, turbidity, and water current velocities, providing important information about physical, chemical, and even biological properties of the water column. CTD measurements can therefore be used to detect evidence of volcanoes, hydrothermal vents and mud volcanoes that cause changes to the physical and chemical properties of seawater. CTD data are also important in acquiring sound velocity profiles of the water column for accuracy of multibeam bathymetry measurements.

3.4 Visual observations and quantification of extruded material and gas

Visual observations in the Scoglio d'Affrica area over the years were performed both by diving and by Remotely Operated Vehicles (ROVs).

Calculations of bubble sizes, numbers and emission frequency were done by analyzing video recordings frame by frame. Individual frames were analyzed using the program VLC. The volume was calculated by assuming that:

- gas bubbles have the same average size for each sampling site;
- gas bubble is approximated to a sphere;
- gas bubble vertical velocity is constant;
- gas bubbles rise in a vertical path;
- difference in depth and pressure are not taken into account.

The volume flux was calculated in cubic meters (m^3) per minute (min) by multiplying the average bubble volume with the number of emitted bubbles per minute. The calculated fluxes have been converted to an annual basis.

3.4.1 Estimated error

The major uncertainty in estimating the gas volume flux is due to uncertainties in measuring the bubble radius by visual quantification. It is also very likely that additional bubbles emanating from the seepage site and from other sites nearby remained undetected. The number of emitted bubbles per minute was calculated from ROV/camera observation periods ranging from a few seconds to minutes; as a consequence, temporal variability of emissions is not taken into account in the calculations and the error in the number of bubble per second increased due to the multiplications in order to achieve a frequency per year.

3.4.2 Mound 1

In 2011 the HYDRA Institut für Meereswissenschaften recorded the presence of gas emissions and fresh mud eruption at mound 1. The video is published on YouTube platform (HYDRA, 2011).

Based on the video (fig. 10) and the report made by the Hydra Institute, at least fourteen gas emission spots were identified. The radii of the bubbles were estimated using, where possible, the human figure in the video.

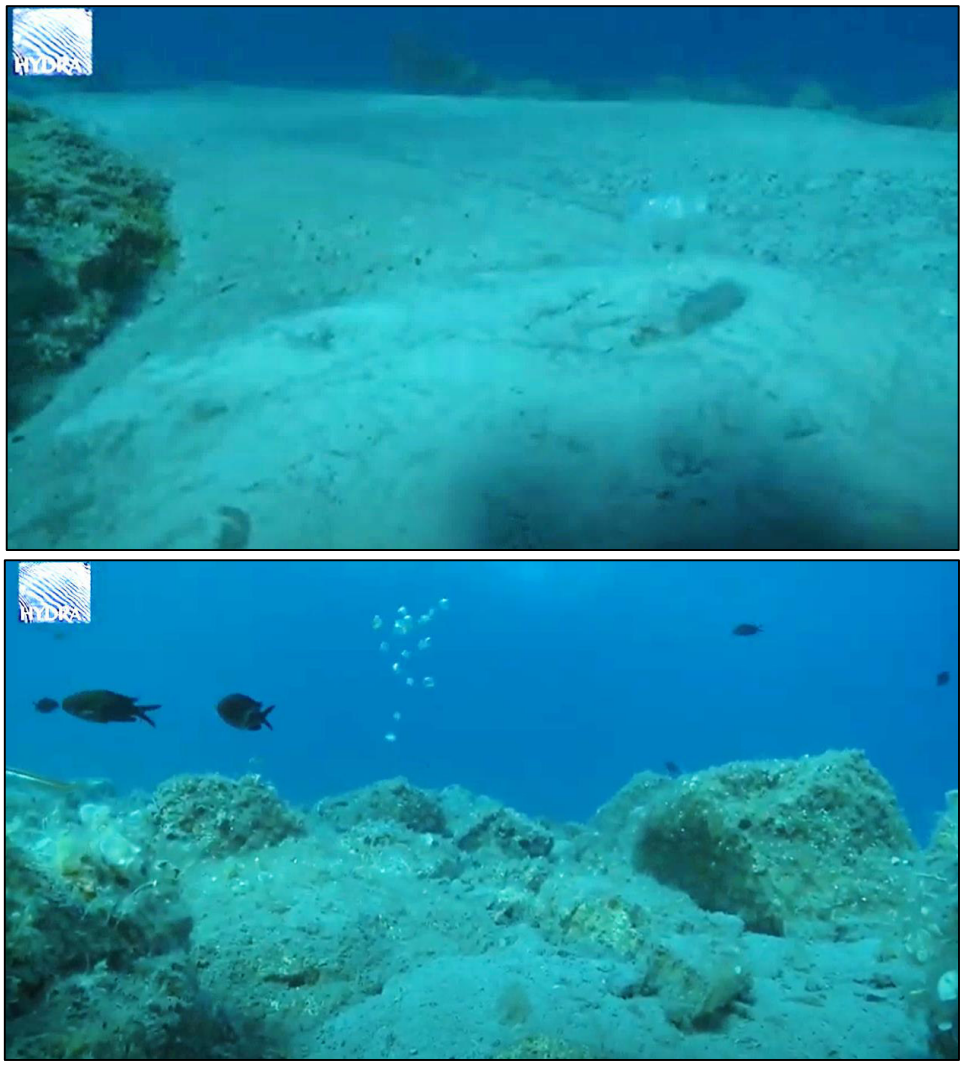

Figure 10 – Frames of the video at mound 1 (from **HYDRA, 2011**).

3.4.3 Mound 2

In 2018 video recordings and a photo mosaic of the top of mound 2 were performed by diving (Saroni et al., 2020). Considering the results of the 2018 diving campaign and the photo-mosaic reproduction of the seabed (fig. 12) (Saroni et al., 2020), at mound 2 the range of flux had been estimated considering:

- N. 7 emission sites with bubbles diameter between 1 and 5 mm (sampling sites 2, 4, 5, 6, 8, 9, 10 in fig. 12-13);
- N. 3 emission sites with bubbles dimeter between 5 and 10 cm (sampling sites 1, 3, 7 in fig. 12-13).

The bubble diameter was estimated using an object of known size (e.g. target number 3 of 15 cm length, see fig. 11) and by direct observations. In 2019 the ROV e-URoPe (e-Underwater Robotic Pet) of the CNR-INM was used in order to explore the Scoglio d'Affrica area, included mound 2 (Ferretti et al., 2021). The video frames were used in order to estimate the frequency for the 1÷5 mm diameter bubbles.

Figure 11 – Frame of the video at sampling site 3 at mound 2.

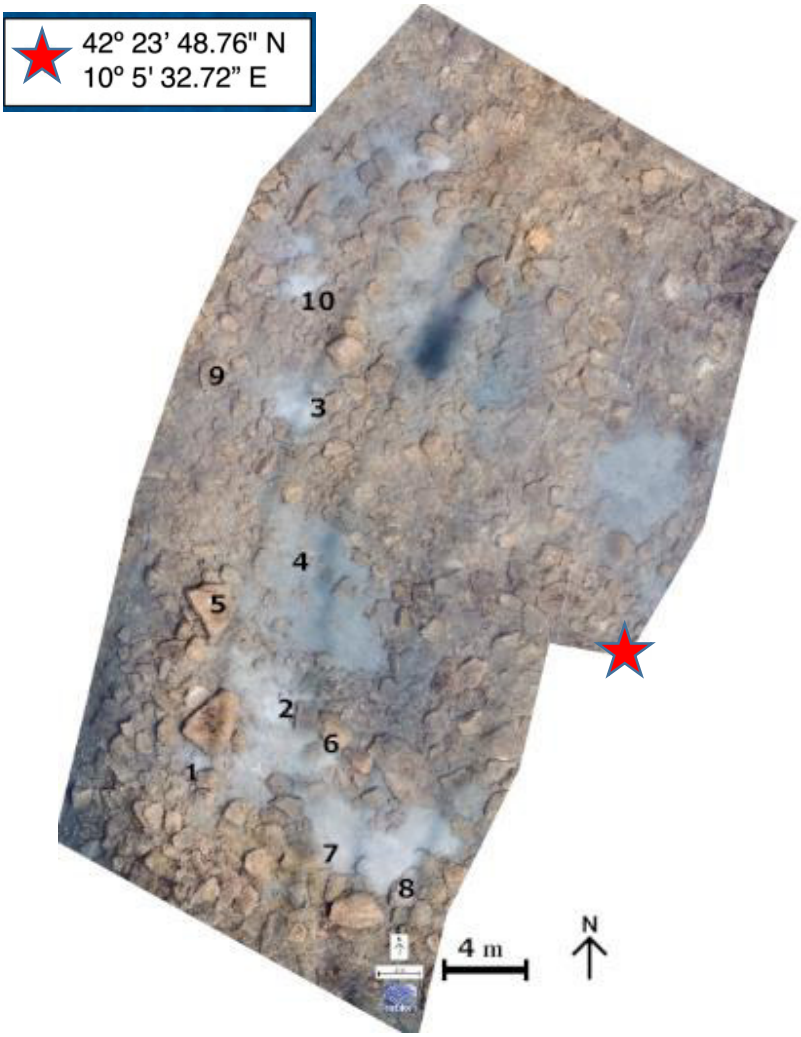

Figure 12 – Photo mosaic of the emission area in 2018 at Scoglio d'Affrica mud volcano. At least 10 sites of emission are recognizable (from Saroni et al., 2020).

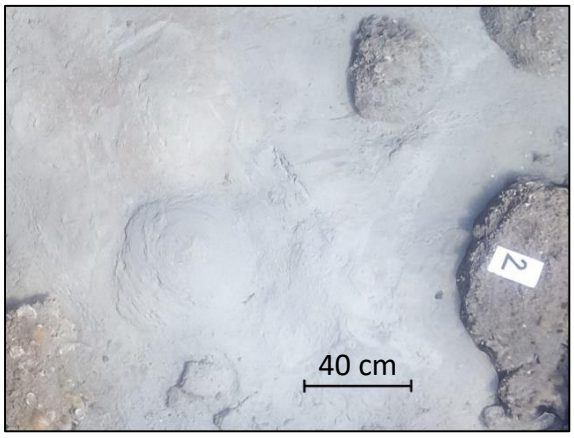

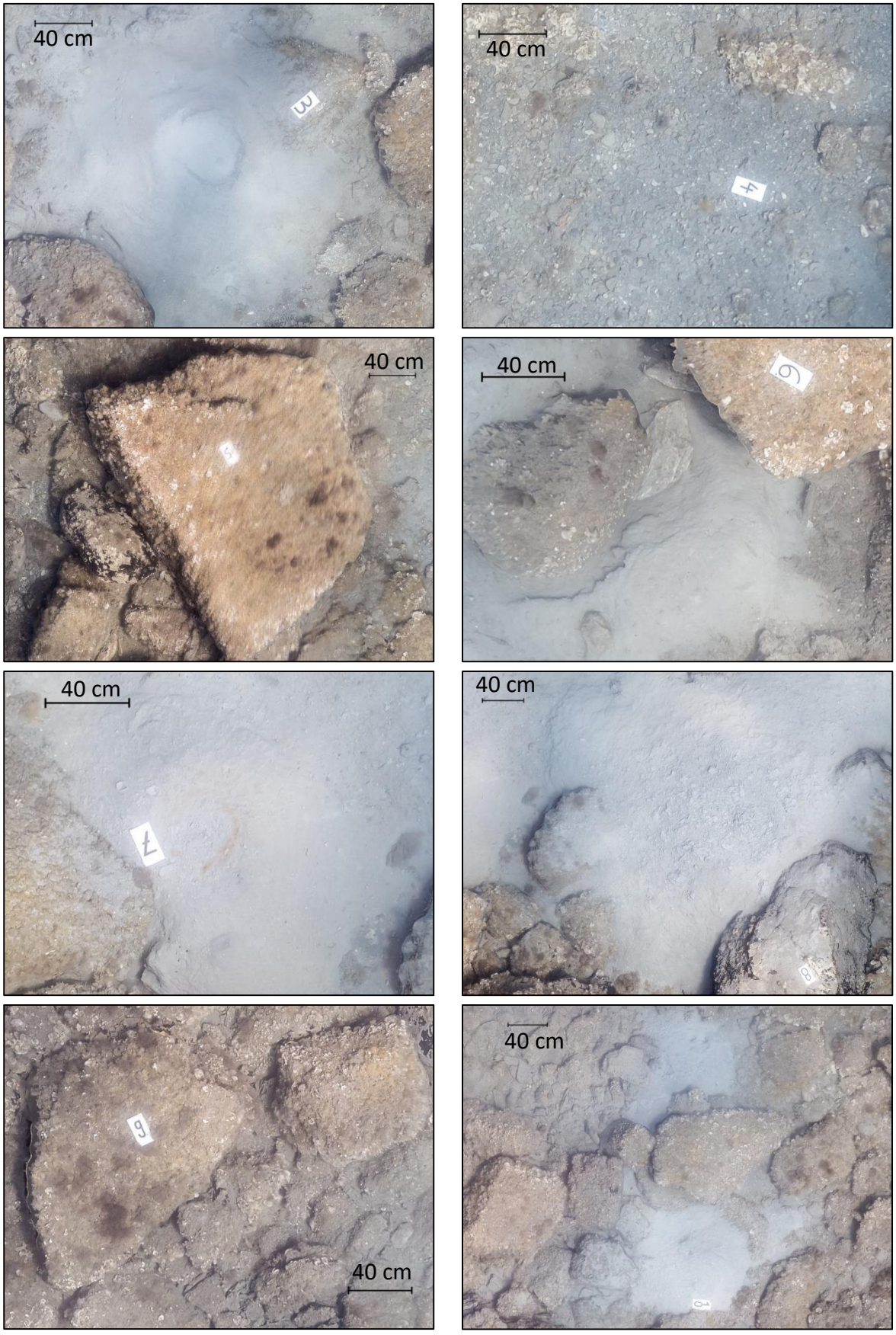

Figure 13 – Zoom in of sites of emission at mound 2.

3.4.4 Mound 3

As Casalbore et al. (2020) reported, on March 21st 2017 (5 days after the explosive event) a ROV survey was carried out aboard a small vessel of the Italian Coast Guard in order to assess seafloor characteristics and gas seepage in correspondence of mound 3. A single dive was performed using the ROV Pollux III (Global Electric Italiana), equipped with a Sony CCD 1/3" navigation camera, a Sony HDRCX115E high-definition camera and a GoPro camera. Due to the lack of an underwater positioning system, the ROV track was inferred from the boat GPS. Considering the shallow water setting of the explored area and the fact that the ROV was kept a few meters away from the boat, a maximum location error of ±10 m can be inferred.

At mound 3 there were no reference objects, so the bubble radius estimation was done considering an average diameter of 3 mm for all the bubbles (fig. 14).

Figure 14 – Frame of the video at sampling site 3 at mound 2.

There are no visual observations of mound 4.

4. RESULTS

4.1 Seafloor morphology

4.1.1 Mound 1

Fig. 15-16-17 show the bathymetry at mound 1 in 2017, 2019 and 2022.

The base of the mound has a diameter of about 390 m and is located at a depth of -30 m in the eastern and southern flanks and -45 m in the western and northern flanks. The top of the mound consists of a crater with an irregular rim of about 60 m diameter that reaches -7 m water depth. The bottom of the N and S-W flanks are characterized by the presence of landslide crowns. The estimated volume of the mud volcano (considering a truncated-conical shape) is about $1{,}5 \cdot 10^3$ m^3.

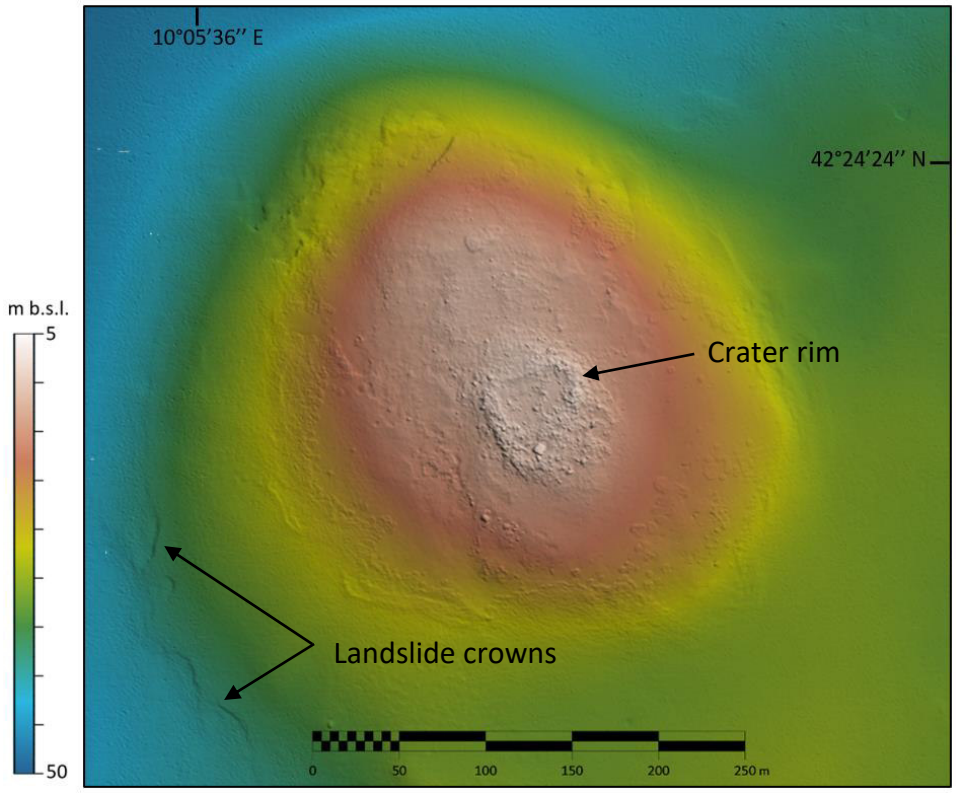

Figure 15 – Mound 1 bathymetry in 2017.

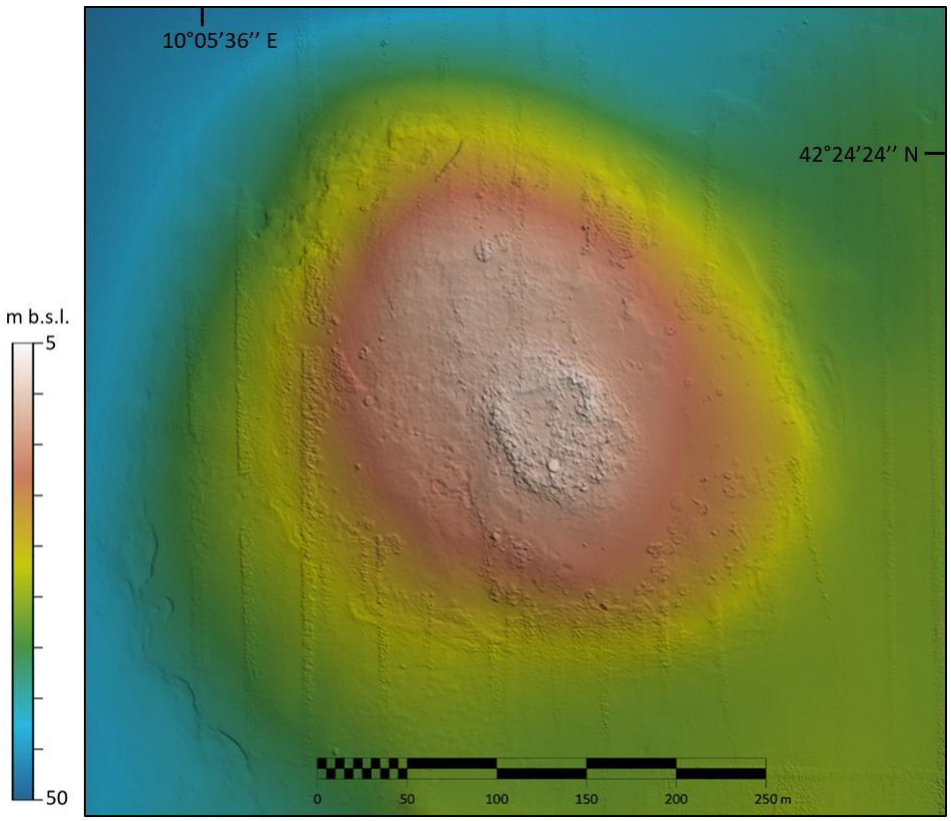

Figure 16 – Mound 1 bathymetry in 2019.

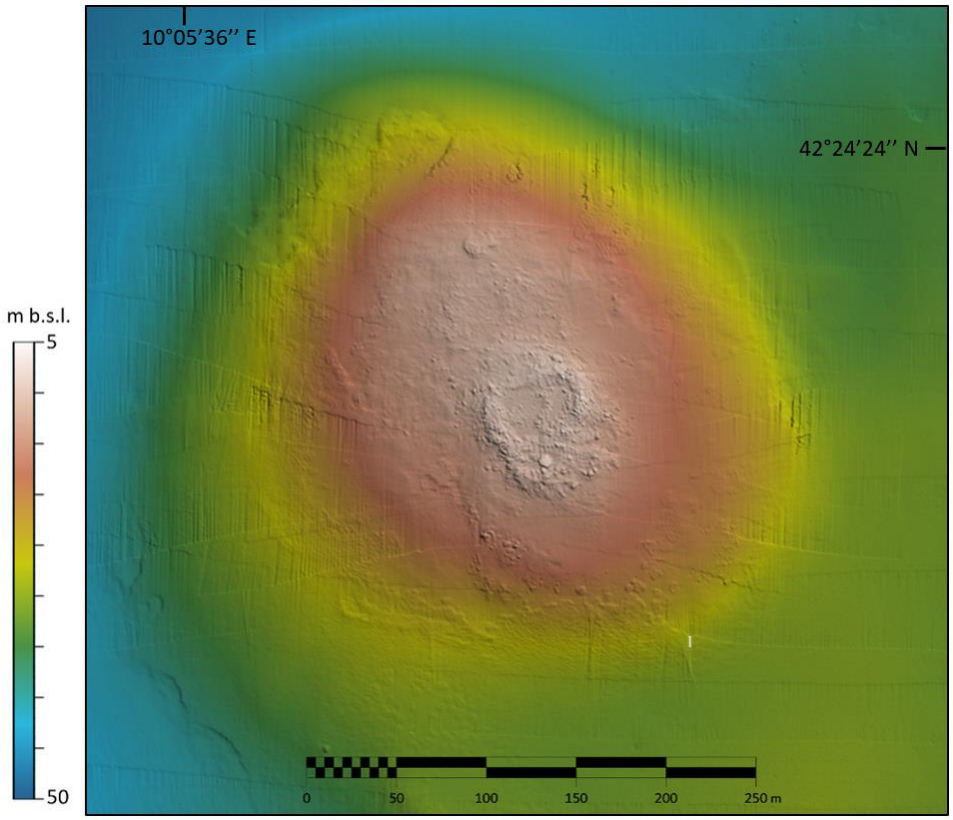

Figure 17 – Mound 1 bathymetry in 2022.

4.1.2 Mounds 2 and 3

The investigated area consists of two circular mounds (mound 2 and 3 in fig. 18) separated by an 80 m broad saddle. The top of mound 2 reaches a diameter of approximately 40 m, while the top of the mound 3 has a diameter of approximately 55 m. Fig. 18 underlines several lobate flows especially on the west slope of mound 3 and some landslide crowns north of mound 2 and south of mound 3.

At mound 3 it is possible to identify a rim, some moats and raised central bulges of freshly extruded sediment in the crater, as also reported in Evans et al. (2008) and in Cuffaro et al. (2019) (fig. 18).

The estimated volume of the mound 2 (considering a truncated-conical shape) is about $0{,}16 \cdot 10^3$ m^3 and of the mound 3 is about $0{,}29 \cdot 10^3$ m^3.

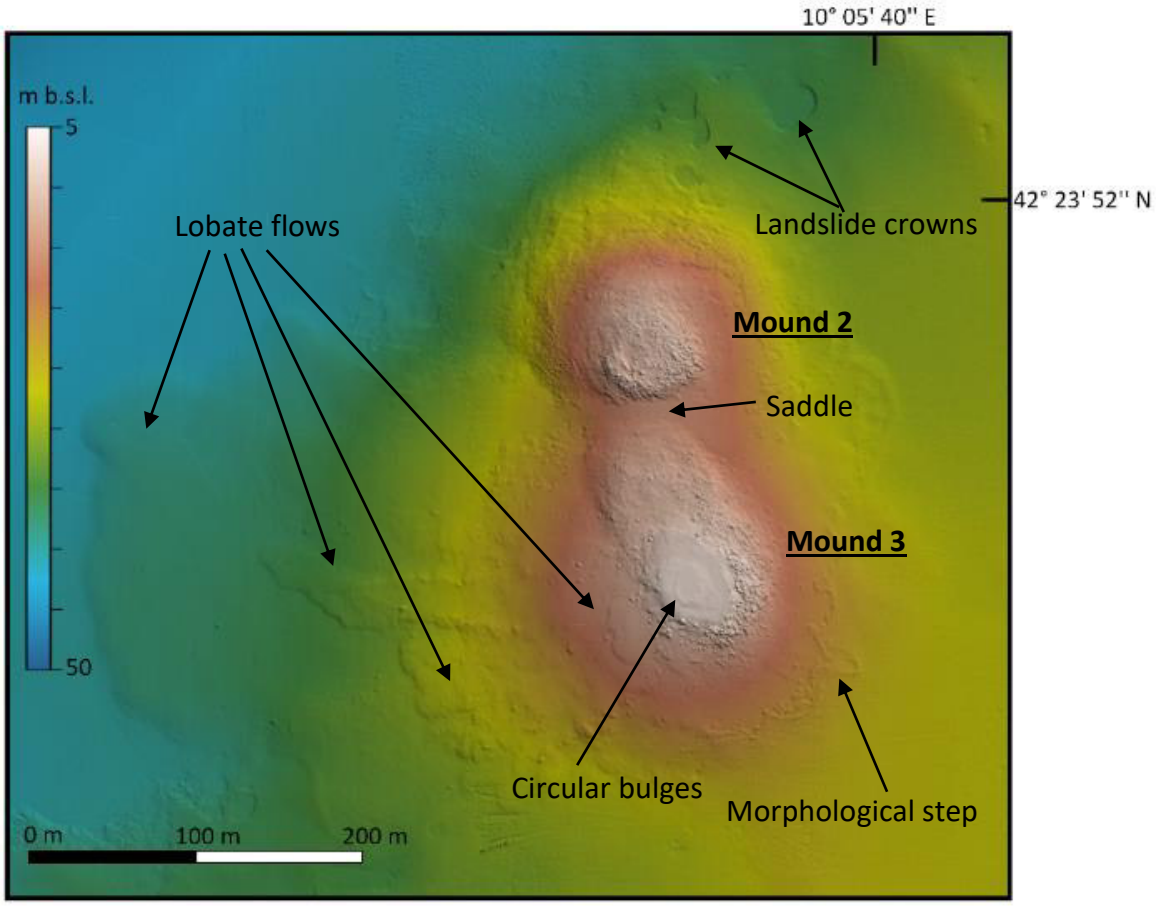

Figure 18 - Mounds 2 and 3 bathymetry in 2017.

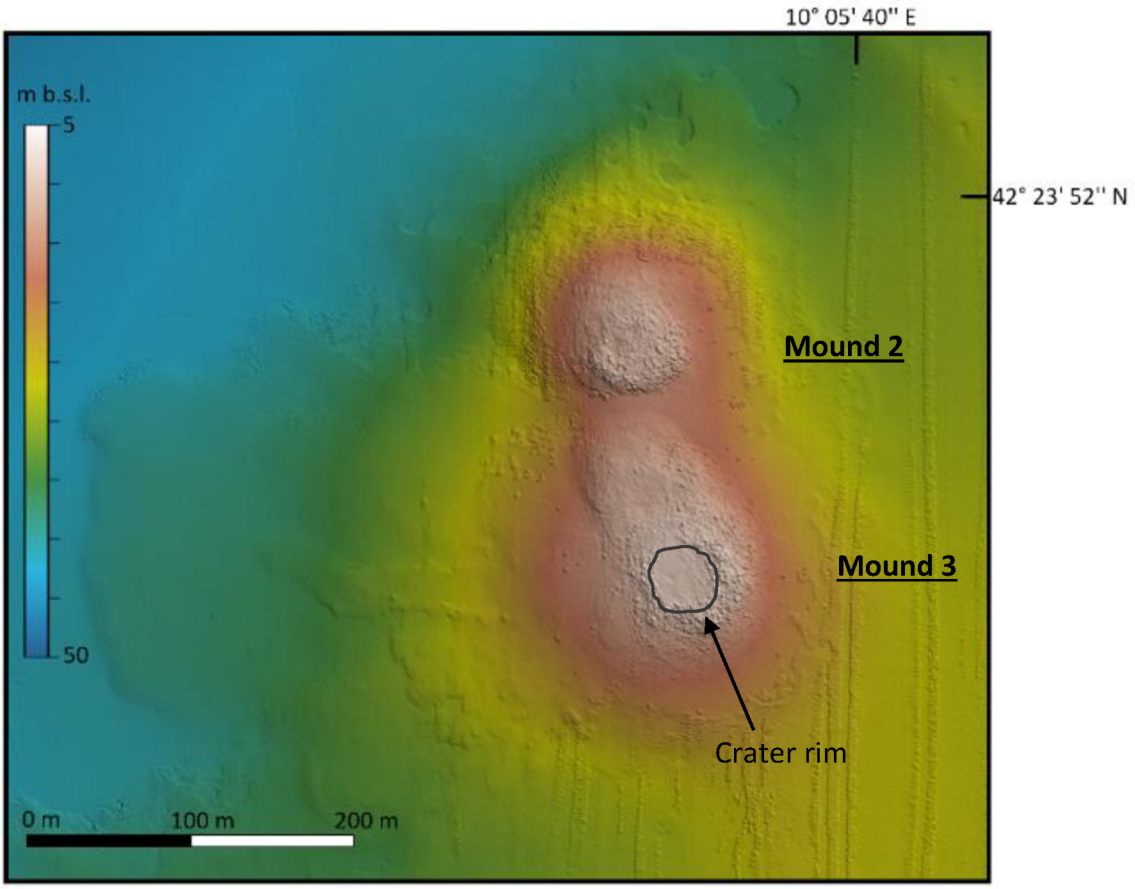

Figure 19 - Mounds 2 and 3 bathymetry in 2019.

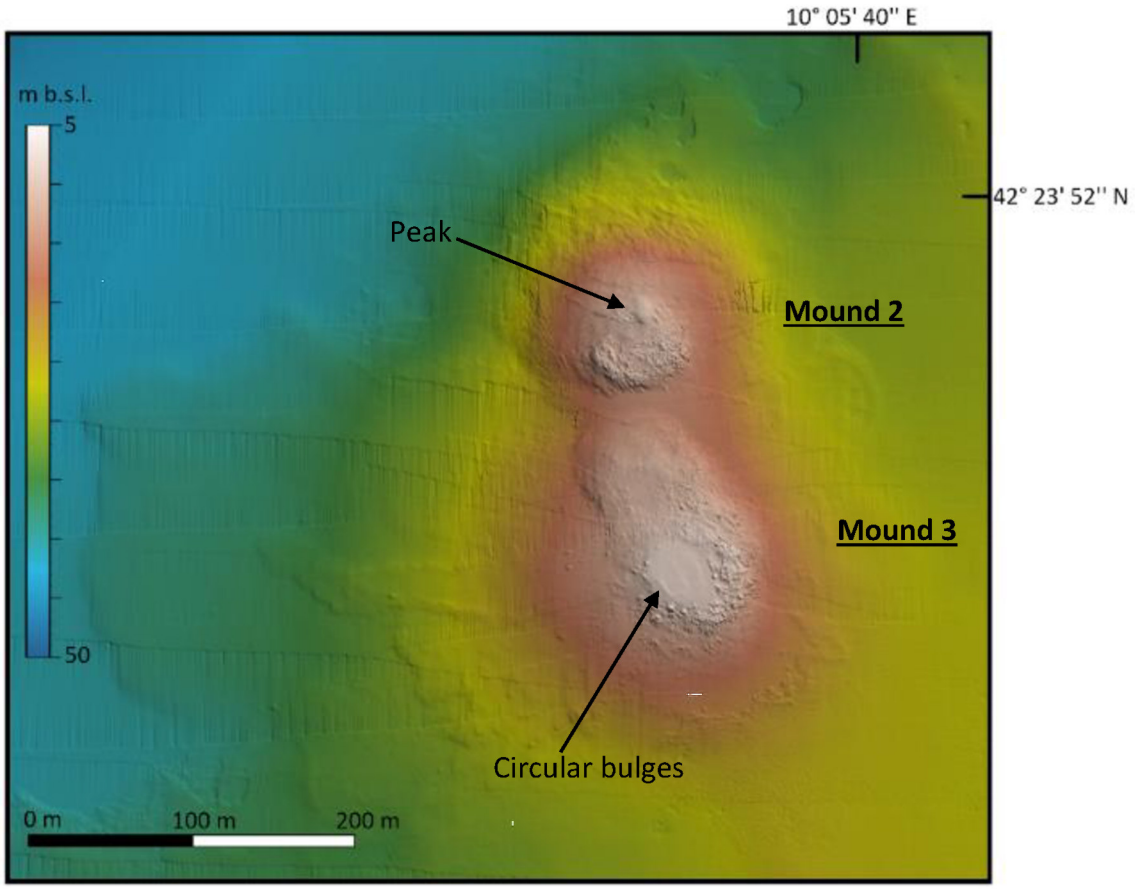

Figure 20 - Mounds 2 and 3 bathymetry in 2022.

4.1.3 Mound 4

Mound 4 has a clear circular shape with a top diameter of about 110 m and a bottom diameter of about 190 m. The surrounding sea bottom is at a depth of about -25 m, while the top of the mound reaches -15.3 m depth. Fig. 21-22-23 show the bathymetry at mound 4 from 2017 to 2022. The mound is characterized by the presence of several fractures and depression forms, localized at the top, on the north-west slope and in the south.
The approximated volume of the mound is about $0{,}18 \cdot 10^3$ m^3.

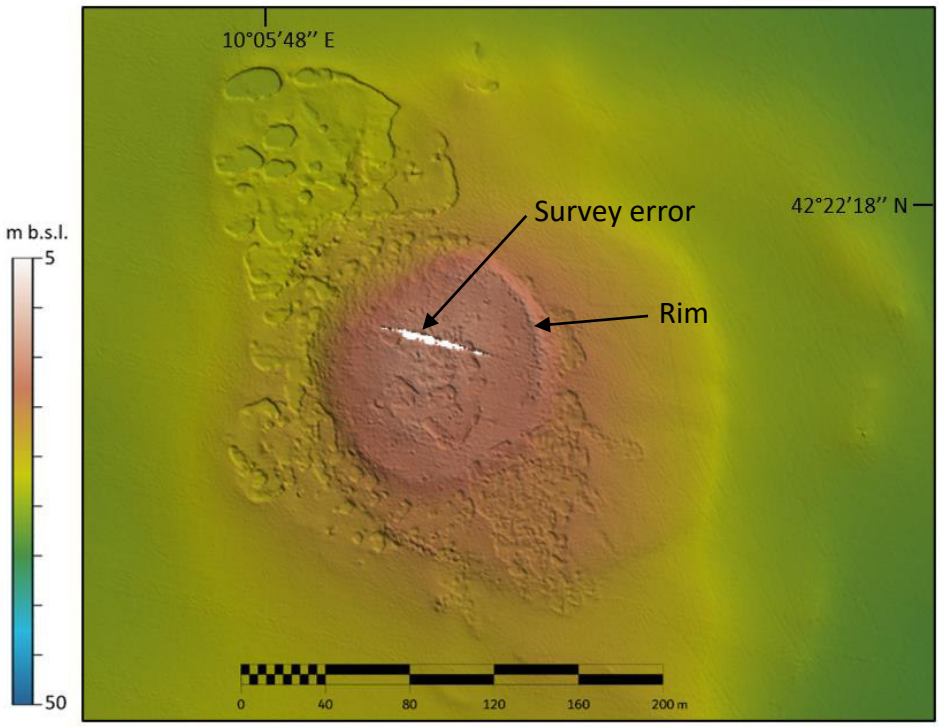

Figure 21 – Mound 4 bathymetry in 2017.

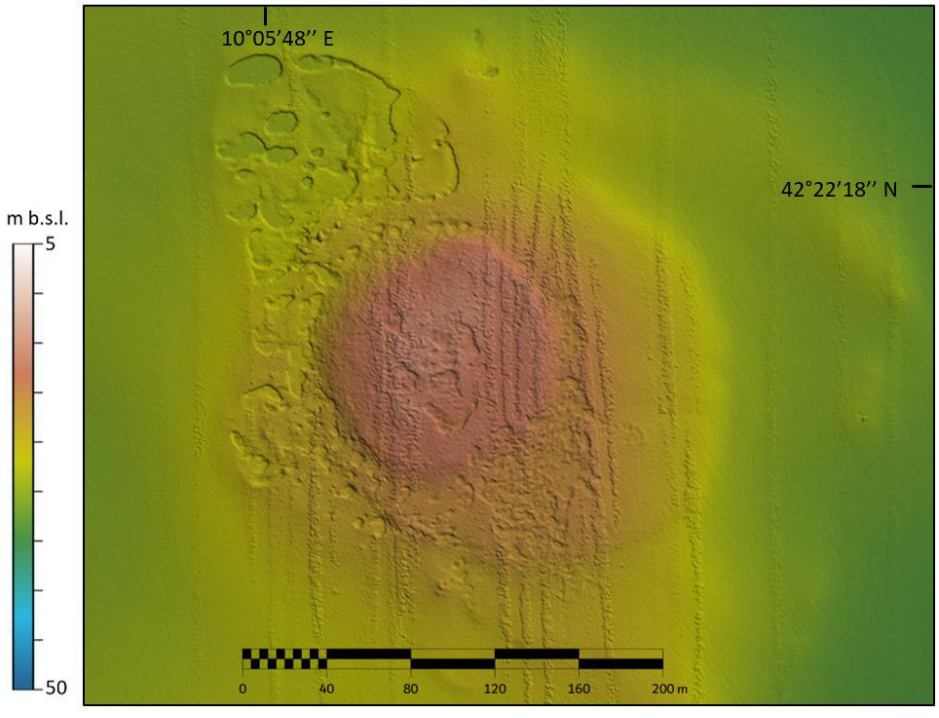

Figure 22 – Mound 4 bathymetry in 2019.

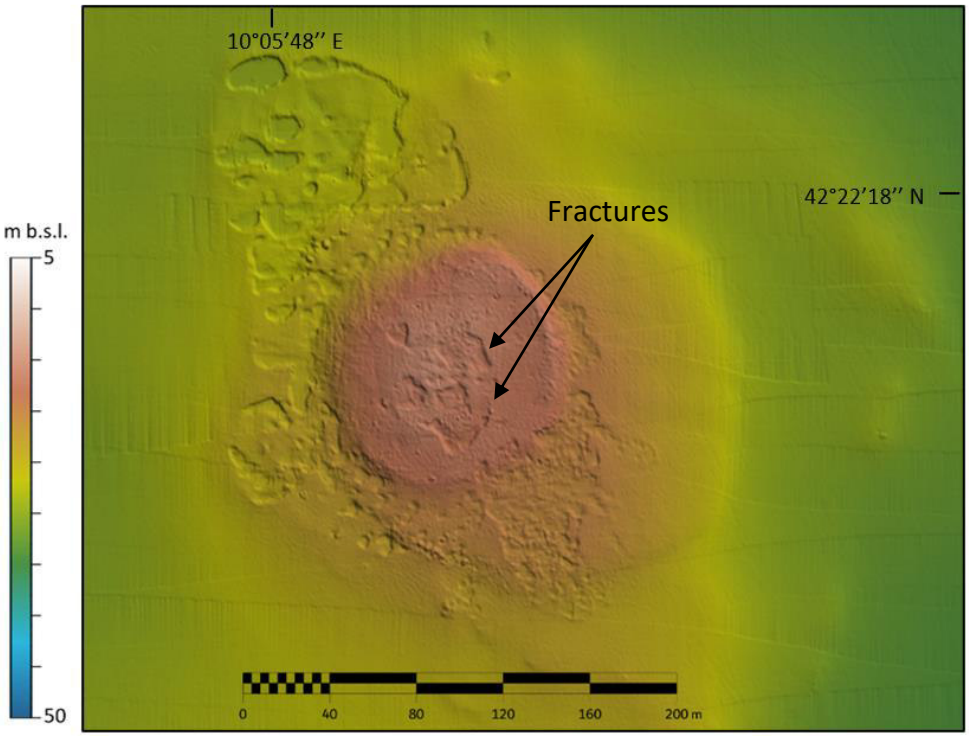

Figure 23 – Mound 4 bathymetry in 2022.

4.2 Quantification of the emitted gas

4.2.1 Mound 1

The volume of gas emitted at mound 1 in one year is about $4 \cdot 10^7$ m^3 (percentage error of 70%).

Table 2 – Quantification of the emitted gas at mound 1.

Site	Bubble average radius (mm)	Bubbles min^{-1}	Gas flow rate (m^3 yr^{-1})
1	37.5 ± 12.5	8 ± 1	675,282 ± 307,613
2	1.5 ± 1.0	467 ± 13	1,540,358 ± 1,070,916
3	1.5 ± 1.0	216 ± 12	712,966 ± 514,920
4	1.5 ± 1.0	190 ± 10	627,146 ± 451,105
5	1.5 ± 1.0	300 ± 20	990,230 ± 726,169
6	1.5 ± 1.0	180 ± 9	594138 ± 424,385
from 7 to 14	1.5 ± 1.0	1220 ± 40	4,026,937 ± 2,816,655
Tot.			**37,355,617** ± 26,028,350

4.2.2 Mound 2

The volume of gas emitted at mound 2 in one year is about $8 \cdot 10^6$ m^3 (percentage error of 65%).

Table 3 – Quantification of the emitted gas at mound 2.

Site	Bubble average radius (mm)	Bubbles min^{-1}	Gas flow rate (m^3 yr^{-1})
1	25 ± 10	5	275,064 ± 110,026
2	1.5 ± 1.0	320 ± 10	1,056,246 ± 737,172
3	50 ± 10	5	550,128 ± 110,026
4	1.5 ± 1.0	320 ± 10	1,056,246 ± 737,172
5	1.5 ± 1.0	320 ± 10	1,056,246 ± 737,172
6	1.5 ± 1.0	320 ± 10	1,056,246 ± 737,172
7	25 ± 10	5	275,064 ± 110,026
8	1.5 ± 1.0	320 ± 10	1,056,246 ± 737,172
9	1.5 ± 1.0	320 ± 10	1,056,246 ± 737,172
10	1.5 ± 1.0	320 ± 10	1,056,246 ± 737,172
Tot.			**8,493,976** ± 5,490,277

4.2.3 Mound 3

The volume of gas emitted at mound 3 in one year is about $5 \cdot 10^7$ m^3 (percentage error of 71%).

Table 4 – Quantification of the emitted gas at mound 3.

Site	Bubble average radius (mm)	Bubbles min^{-1}	Gas flow rate (m^3 yr^{-1})
1	1.5 ± 1.0	222 ± 7	733,936 ± 512,590
2	1.5 ± 1.0	3200 ± 100	10,562,458 ± 7,371,715
3	1.5 ± 1.0	893 ± 33	2,948,686 ± 2,075,816
5	1.5 ± 1.0	600 ± 30	1,980,461 ± 1,419,330
6-7-8-9	1.5 ± 1.0	2550 ± 150	8416958 ± 6,106,421
4-10-11	1.5 ± 1.0	647 ± 15	2,136,813 ± 1,476,659
Tot.			**56,303,813** ± 40,235,113

4.3 Water column analysis - CTD multiparameter probe

4.3.1 Mound 1

The results of the CTD sampling are reported in figures 24-25-26. As reported in tab. 5, samples n. 2, 3, 4 were taken nearby the mud volcano, while samples 1, 5, 6 were taken in the mud volcano area.

Table 5 – Coordinates of the CTD sampling at mound 1.

ID	Coordinates WGS-84	Sampling map
1	42° 24' 20.79'' N; 10° 5' 43.36'' E	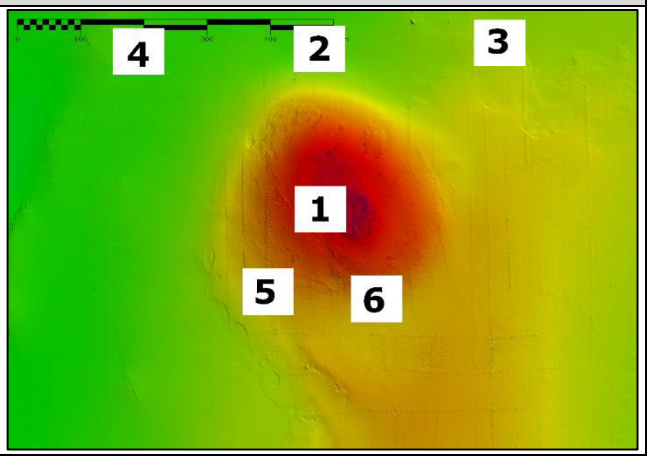
2	42° 24' 29.20'' N; 10° 5' 43.44'' E	
3	42° 24' 29.52 N; 10° 5' 55.78'' E	
4	42° 24' 29.14'' N; 10° 5' 31.39'' E	
5	42° 24' 16.53'' N; 10° 5' 39.47'' E	
6	42° 24' 15.60'' N; 10° 5' 48.13'' E	

The temperature of samples 1, 5, 6 ranges from 21.88 °C (1) at surface to a temperature of 16.81 °C at -26.15 m depth (6). The temperature of samples 2, 3, 4 ranges from 20.60 ° C (3) at surface to a temperature of 14.70 °C at -48.03 m depth (4).

At -10.12 m depth, the temperature of samples 1 is 18.95 °C, while the temperature of sample 3 at -10.18 m depth is 19.90 °C.

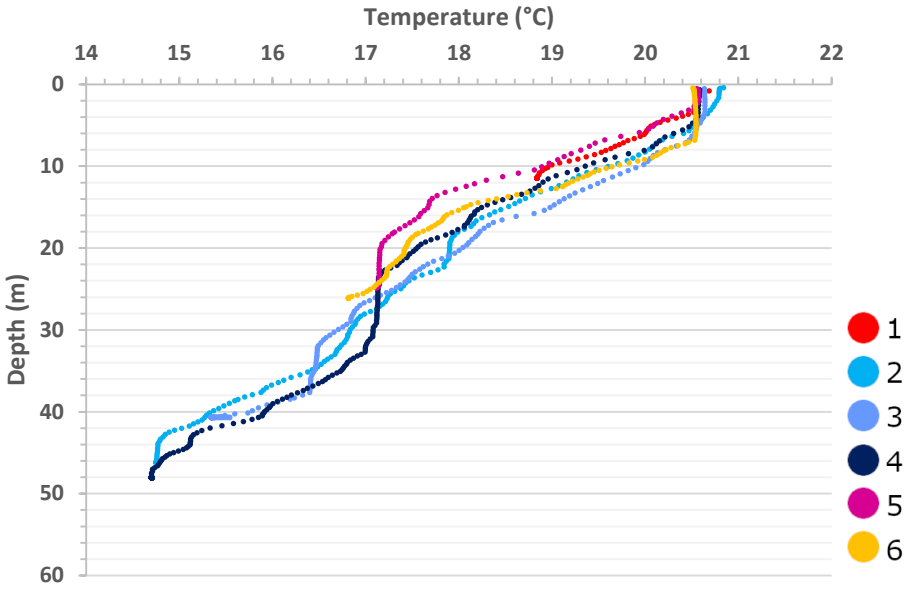

Figure 24 – CTD temperature results relative to depth at mound 1.

Without considering the first meter and a half of data from the surface, the salinity of samples 1, 5, 6 ranges from 37.81 PSU (1) at -1.64 m depth to a salinity of 38.00 PSU at -20.27 m depth (6). The salinity of samples 2, 3, 4 ranges from 37.75 PSU (3) at -1.49 m depth to a salinity of 38.12 PSU at -40.68 m depth (3).

At -10.12 m depth, the salinity of samples 1 is 37.91 PSU, similar to the salinity of sample 3 (37.95 PSU) at the same depth.

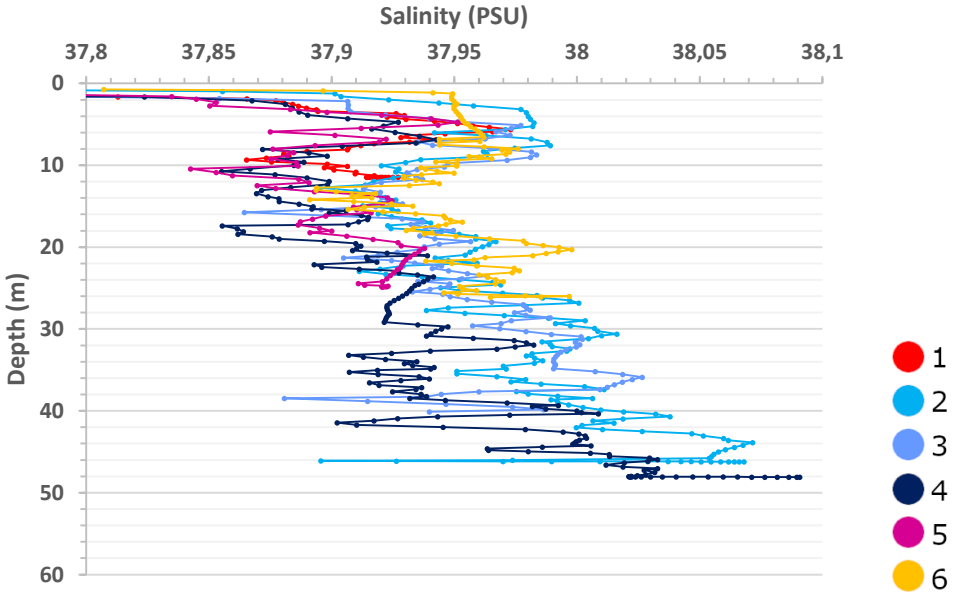

Figure 25 – CTD salinity results relative to depth at mound 1.

Without considering the first meter and a half of data from the surface, the conductivity of samples 1, 5, 6 ranges from 52.09 mS cm^{-1} at -5.82 m depth (6) to a conductivity of 47.90

mS cm^{-1} at -26.15 m depth (6). The conductivity of samples 2, 3, 4 ranges from 52.30 mS cm^{-1} at -1.99 m depth (3) to 45.83 mS cm^{-1} at 46.10 m depth (2).
At -10.12 m depth, the conductivity of samples 1 is 50.30 mS cm^{-1}, while the conductivity of sample 3 at -10.18 m depth is 51.38 mS cm^{-1}.

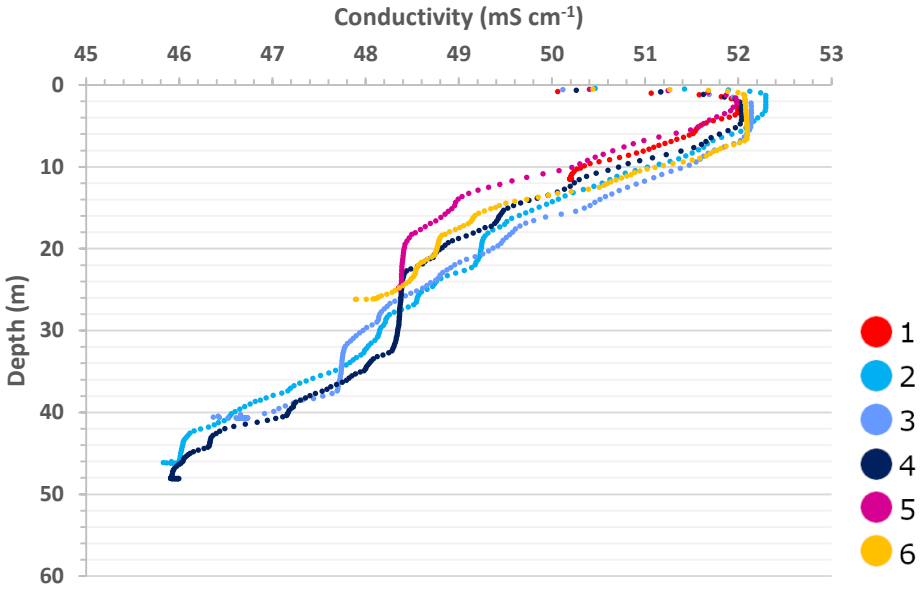

Figure 26 – CTD conductivity results relative to depth at mound 1.

4.3.2 Mounds 2 and 3

Table 6 shows the location of the CTD sampling at mounds 2 and 3. Samples n. 1, 5, 9 and 13 were taken nearby the mud volcano, while samples 17, 18, 19 were taken at mound 2 and samples 20, 21, 22, 23 at mound 3. The results are represented in figures 27-28-29.

Table 6 – Coordinates of the CTD sampling at mounds 2 and 3.

ID	Coordinates WGS-84	
1	42° 23' 52.42 N; 10° 5' 42.53'' E	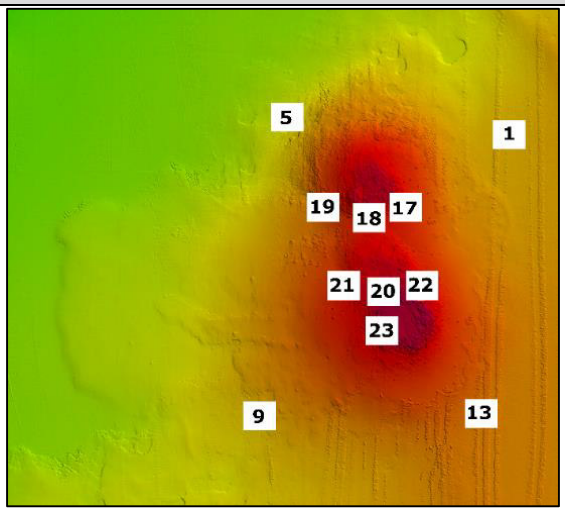
5	42° 23' 53.22 N; 10° 5' 28.68'' E	
9	42° 23' 39.87 N; 10° 5' 28.12'' E	
13	42° 23' 39.91 N; 10° 5' 40.84'' E	
17	42° 23' 49.13 N; 10° 5' 36.74'' E	
18	42° 23' 49.12 N; 10° 5' 34.02'' E	
19	42° 23' 49.15 N; 10° 5' 31.90'' E	
20	42° 23' 45.70 N; 10° 5' 35.35'' E	
21	42° 23' 45.73 N; 10° 5' 33.29'' E	
22	42° 23' 45.58 N; 10° 5' 37.38'' E	
23	42° 23' 43.93'' N; 10° 5' 35.36'' E	

The temperature of samples 1, 5, 9, 13 ranges from 20.63 °C (1) at surface to a temperature of 14.88 °C at -39.95 m depth (5). The temperature of samples 17, 18, 19 ranges from 20.76 ° C (19) at surface to a temperature of 16.81 °C at -20.78 m depth (17). The temperature of samples 20, 21, 22, 23 ranges from 20.80 ° C (21) at surface to a temperature of 17.71 °C at -18.40 m depth (22).

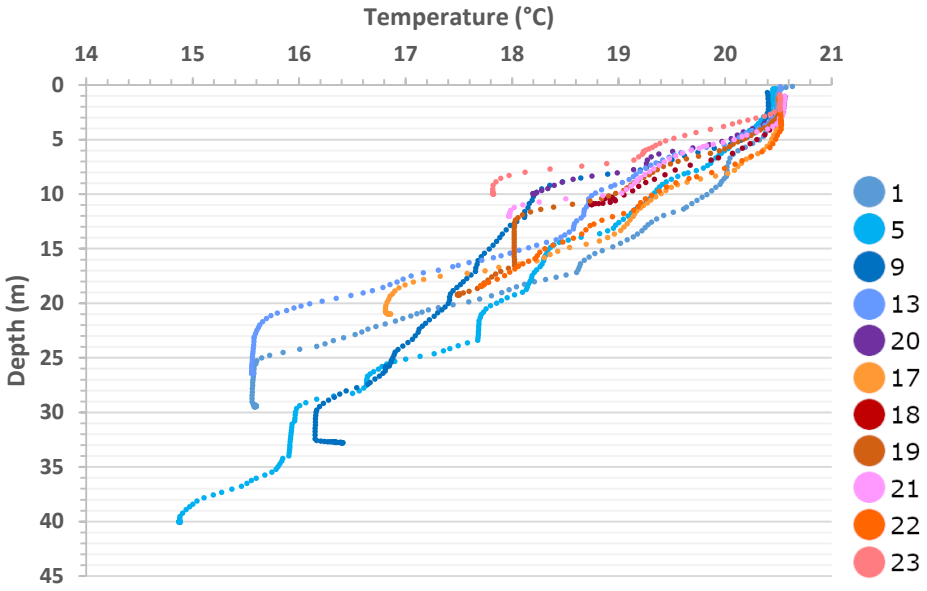

Figure 27 – CTD temperature results relative to depth at mounds 2 and 3.

The salinity of samples 1, 5, 9, 13 ranges from 37.53 PSU (13) at surface to a salinity of 38.06 PSU at -22.76 m depth (13) and at -40.00 m depth (5). The salinity of samples 17, 18, 19 ranges from 37.41 PSU (17) at surface to a salinity of 38.04 PSU at -6.51 m depth (19). The salinity of samples 20, 21, 22, 23 ranges from 37.52 PSU (22) at surface to a salinity of 37.99 PSU at -4.59 m depth (20).

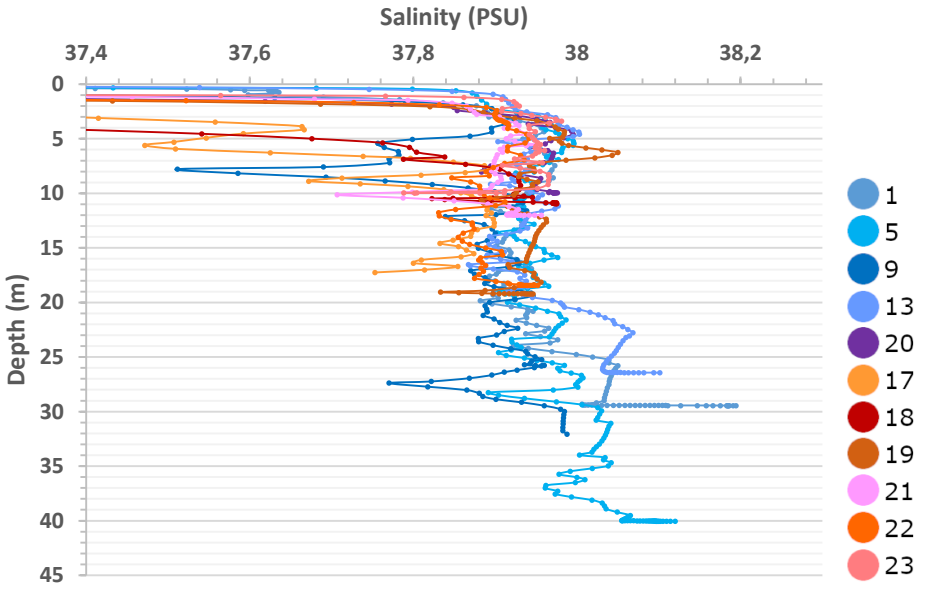

Figure 28 – CTD salinity results relative to depth at mounds 2 and 3.

The conductivity of samples 1, 5, 9, 13 ranges from 52.00 mS cm^{-1} at -2.53 m depth (13) to a conductivity of 46.14 mS cm^{-1} at -40.00 m depth (5). The conductivity of samples 17, 18, 19 ranges from 51.98 mS cm^{-1} at -3.12 m depth (19) to 48.05 mS cm^{-1} at -20.20 m depth (17). The conductivity of samples 20, 21, 22, 23 ranges from 52.03 mS cm^{-1} at -3.79 m depth (22) to 48.94 mS cm^{-1} at –9.96 m depth (23).

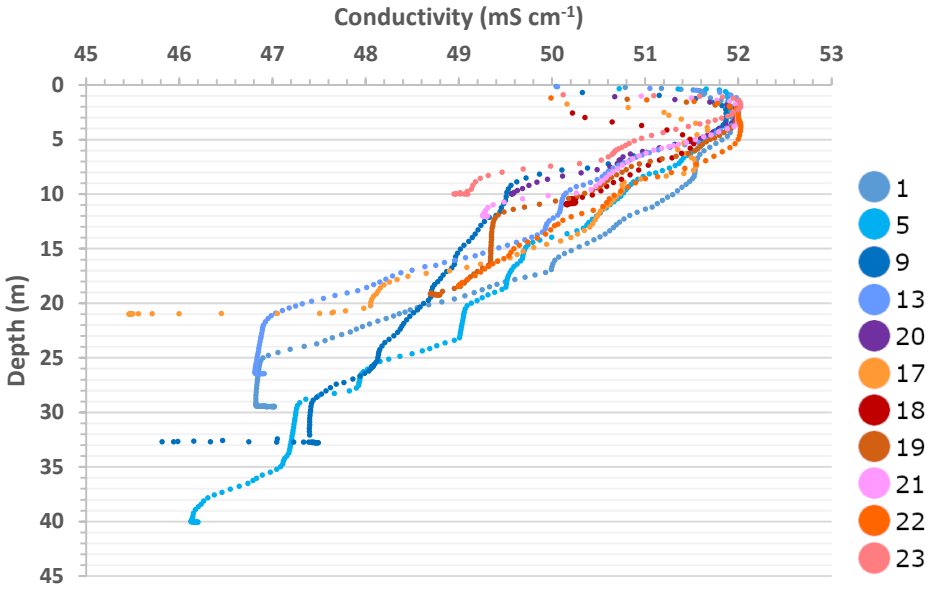

Figure 29 – CTD conductivity results relative to depth at mounds 2 and 3.

4.3.3 Mound 4

Table 7 shows the location of the CTD sampling at mound 4. Samples base4 and base1 were taken far from the mud volcano area, while samples 1 to 7 were taken at mound 4. The results are represented in figures 30-31-32.

Table 7 – Coordinates of the CTD sampling at mound4.

ID	Coordinates WGS-84	
1	42° 22' 17.37'' N; 10° 5' 53.57'' E	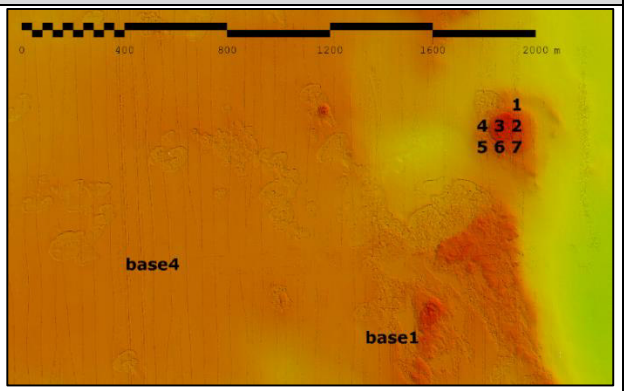
2	42° 22' 15.70'' N; 10° 5' 53.86'' E	
3	42° 22' 15.51'' N; 10° 5' 51.24'' E	
4	42° 22' 15.46'' N; 10° 5' 48.85'' E	
5	42° 22' 13.82'' N; 10° 5' 48.68'' E	
6	42° 22' 13.68'' N; 10° 5' 51.24'' E	
7	42° 22' 13.84'' N; 10° 5' 53.89'' E	
Base 1	42° 21' 51.33'' N; 10° 5' 34.82'' E	
Base 4	42° 21' 69.71'' N; 10° 5' 19.80'' E	

The temperature of samples 1 to 7 are similar to one another. Between -6 and -10 m depth the temperature decreases faster than from 0 to -6 m depth and from -6 to -23 m depth.

(2.30 °C in 2.53 m). At surface the temperature starts from 21.32 °C (4) and decreases with depth until 16.39 °C at -22.84 m depth (5).
The two samples taken outside the mound 4 area show a minimum of 15.97 °C at -24.83 m depth (base4) and a maximum of 21.06 °C (base1) at surface.

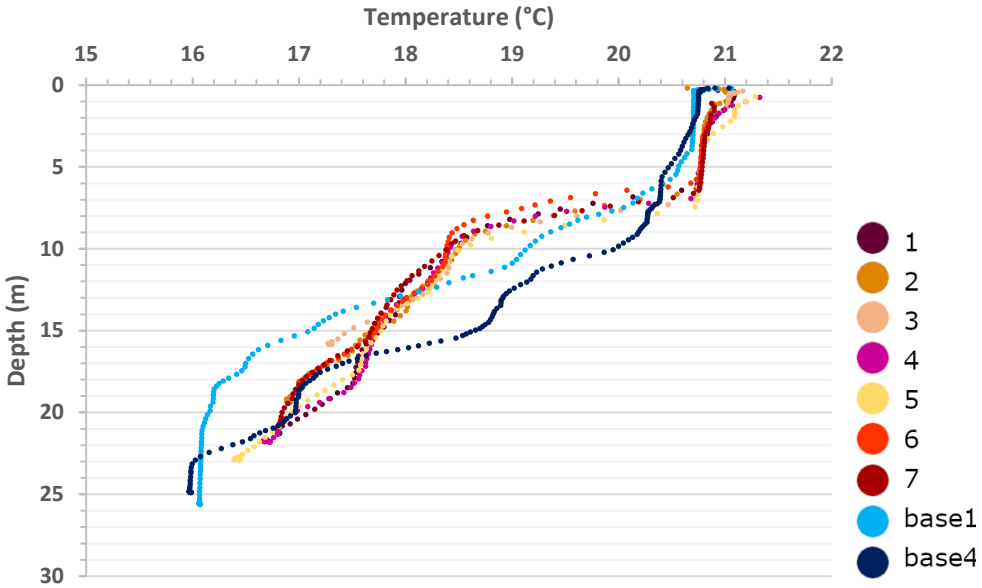

Figure 30 – CTD temperature results relative to depth at mound 4.

Regarding samples 1÷7, figure 31 shows a minimum of 37.59 PSU (3) at -7.30 m depth and a maximum of 38.09 at -22.84 m depth (5). Near surface and for the first 13 m depth the salinity does not exceed 37.8 PSU.
Sample base1 remains in the same range of salinity of the previous samples, instead the sample base4 has a higher salinity between surface and -13.50 m depth, reaching more than 38 PSU.

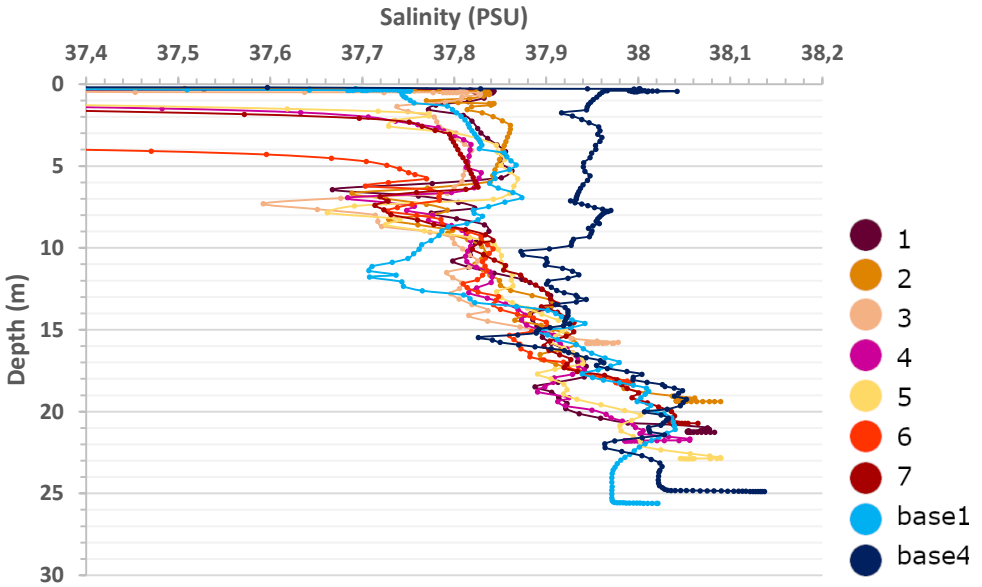

Figure 31 – CTD salinity results relative to depth at mound 4.

The conductivity of samples 1÷7 are similar to one another. Between -6 and -10 m depth the conductivity decreases faster than from 0 to -6 m depth and from -6 to -23 m depth. At surface the conductivity starts from 52.54 mS cm^{-1} (1) and decreases with depth until 47.77 mS cm^{-1} at -22.88 m depth (5).
The two samples taken outside the mound 4 area show a minimum of 47.25 mS cm^{-1} at -24.52 m depth (base4) and a maximum of 52.43 mS cm^{-1} (base4) at surface.

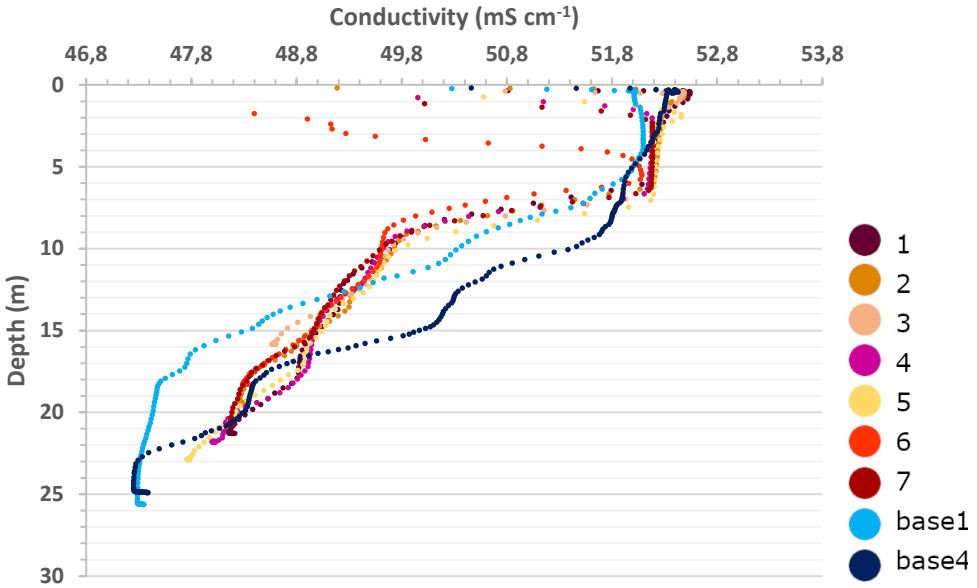

Figure 32 – CTD conductivity results relative to depth at mound 4.

5. DISCUSSION

5.1 Relation between local geology and gas emissions

Methane production in marine environment occurs through either the microbial degradation or thermogenic degradation of organic matter. At temperatures below 80 °C (Schoell, 1988; Whiticar, 1994) only biogenic methane forms by microbial activity through fermentation and CO_2 reduction in shallower burial depths during diagenesis (fig. 33).

Methanogenesis is a biological process that involves anaerobic microorganisms (called methanogens) in the production of methane as part of their metabolism. They use methanogenesis as a form of anaerobic respiration and they are very oxygen-sensitive; for this reason, they live in strictly anaerobic habitats (Madigan et al., 2015).
Methanogens are *Archaea* that can form methane in three different ways, according to the type of organic compounds they utilize in the process:

1. Hydrogenoclastic methanogenesis ($CO_2 + H_2$)
2. Methylamine-based methanogenesis
3. Acetoclastic methanogenesis

Several coenzymes participate in these processes either carrying carbon compounds or donating electrons (Madigan et al., 2015).
In coastal waters, the production of methane mainly occurs in sediments by anaerobic methanogens decomposing organic matter (Garcias-Bonet and Duarte, 2017).
From the anoxic layers, three main mechanisms of methane transport lead it to the aerobic ones, where it can be consumed by methanotrophic bacteria inhabiting the oxic sediments:

1. Gas bubbles
2. Plant-mediated transport
3. Diffusion

After diagenesis, humic substances are no longer present and the organic matter consists mainly of kerogen. Exceeding 70 °C thermal degradation of kerogen begins (Dieckmann et al. 1998; Dieckmann 2005; Horsfield et al. 2006), leading to the formation of primary petroleum. At this point, also thermogenic gas occurs within or after the "oil window" maturation level (catagenesis or metagenesis) in deep hydrocarbon reservoirs.
According to Saroni et al., 2020, methane at Scoglio d'Affrica MVs has a predominant secondary microbial origin and a minor thermogenic component ($\delta^{13}C\text{-}CH_4$ mean around -35.8‰ vs. VPDB, positive $\delta^{13}C\text{-}CO_2$ values up to +21.7‰ vs. VPDB and Bernard ratios around 3000). Helium is entirely produced within the crust from radiogenic decay ($^3He/^4He$ of 0.01 Ra, $^4He/^{20}Ne$ from 75 to approximately 330).

5.1.1 Shallow reservoir

Considering the geothermal gradient in Martina 1 well, located ~14 km north of the Scoglio d'Affrica (fig. 33), the shift from diagenesis to catagenesis occurs at a depth > 1500 m,

corresponding to a temperature > 60 °C (see green dotted line in fig. 34). Therefore, the secondary microbial component of methane, due to the terminal product of oil biodegradation (Zeikus, 1977; Head et al., 2003; Larter et al., 2005; Milkov, 2020; fig. 33), is consistent with the gas found in Martina 1 and Mimosa 1 wells in Miocene-Oligocene deposits, respectively between 542÷547 m (Camera dei Deputati, 1984) and between 1133÷1180 m and 1247÷1278 m (AGIP, 1987).

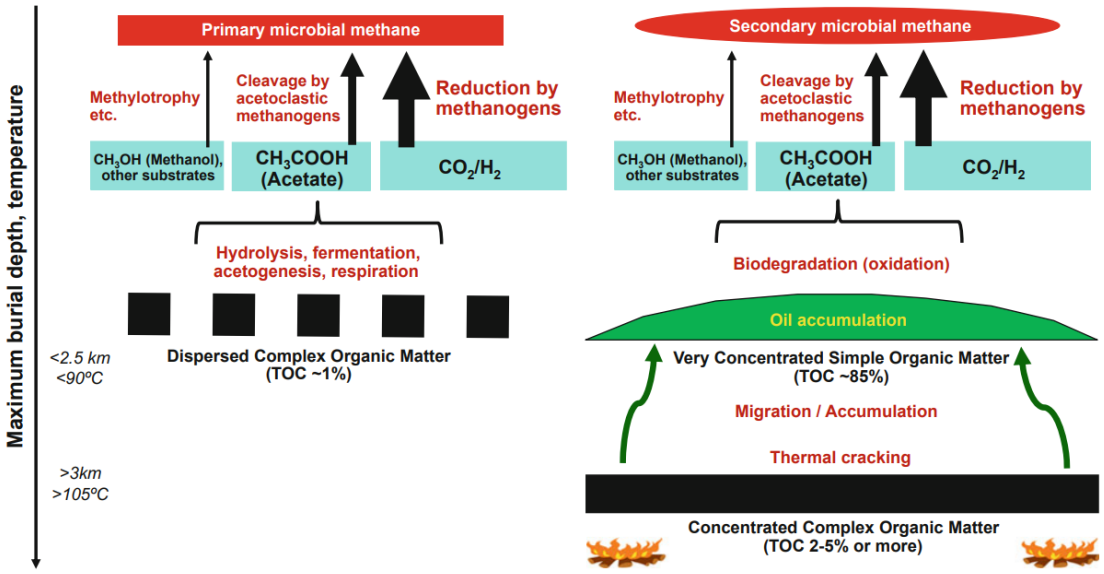

Figure 33 – Formation of primary microbial methane (left panel) and secondary microbial methane (right panel) in the subsurface) (from Milkov, 2020).

5.1.1 Deep reservoir

On the other hand, thermogenic CH_4 is typically generated within deeper sediments and under temperatures that range from 70 to 160 °C (Mahlstedt, 2020). Therefore, the presence of a minor thermogenic component of methane could derive directly from a depth > 1800 m corresponding to a temperature > 70 °C, consistently with the gas found in Eocene deposits in Martina 1 well between 2720÷2830 m depth (Puma Petroleum, 2007).

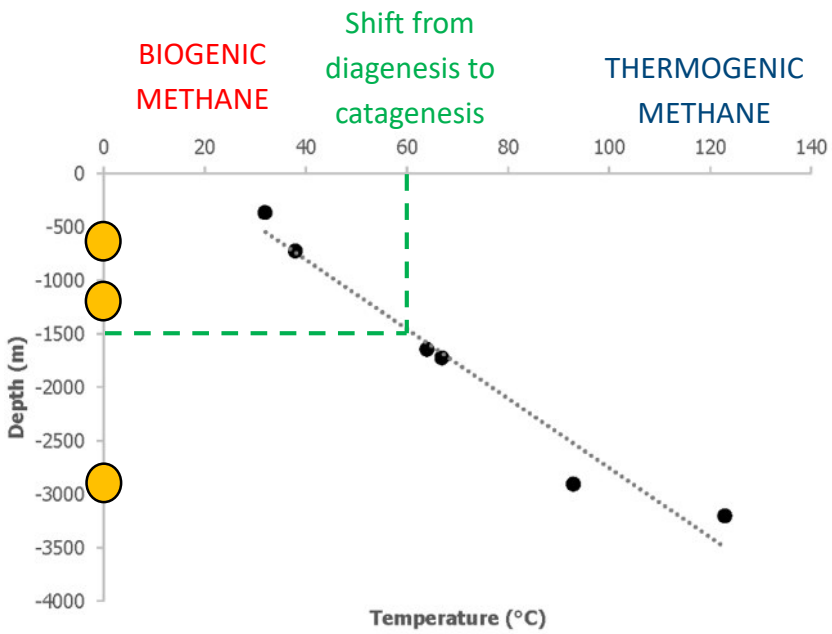

Figure 34 - Temperature vs depth diagram in Martina 1 well, located ~14 km north of the Scoglio d'Affrica (data from GeoThopica). Yellow dots indicate the gas reservoirs depth found in Martina 1 and Mimosa 1 wells.

5.2 Water column

The results of the CTD analysis support the fact that emissions at Scoglio d'Affrica are cold. Indeed, there are no difference in temperature between MVs areas and the nearby water column.

Water above mud volcanoes could show variations in salinity due to a high level of deep source fluid emission (Mazzini et al., 2004). The salinity and conductivity sampled at the four mounds do not show significant trend in order to identify possible mud volcano influences in the water column.

The results can be explained by the following reasons:

- salinity in the water column is influenced by mixing processes and dispersion between seawater and emitted fluids;
- MVs fluid flow was not very active at the moment of sampling or in general the MV emits few deep fluids;
- interstitial water (seawater) prevails in underground shallow mixing processes with deep fluids.

Previous data (Saroni, 2019) showed that waters and porewaters sampled by diving at mound 2, are enriched in Mg. Mg is an insoluble-fluid element, thus the interaction with the sediment, that in the area has a prevalent mineralogic composition characterized by Mg-calcite (Ferretti et al., 1993), cannot be the cause to these high values.

Mg/Cl ratio is considered an indicator of the mixing of the mud volcano fluid and seawater (Mazzini et al., 2004; Mazurenko et al., 2002). A high ratio means that a small fraction of the mud volcano fluid is present in the water sample. In Scoglio d'Affrica samples, Mg/Cl ratio ranges between 0.05 to 0.08 (Saroni, 2019; fig. 35) and it is very similar to the seawater ratio (~0,05). The same situation is reported for other submarine mud volcanoes, such as the Odessa mud volcano in the Black Sea (Mazzini et al., 2004; fig. 35) and the Ginsburg mud volcano in its upper intervals of sediment (Mazurenko et al., 2002).

High level of mud volcanic activity and a deep source of erupted fluids can also be interpreted from variations in Ca and chlorinity (Mazzini et al., 2004 and references therein). Differently from the Dvurechensky mud volcano (Mazzini et al., 2004 and references therein), that is characterized by extremely high chlorinity (three times exceeding of sea water), Ca^{2+} (2 times more than seawater) and a low concentration of Mg^{+}, the chlorinity and Ca in Scoglio d'Affrica samples do not show particular variations compared to seawater concentrations (Saroni, 2019).

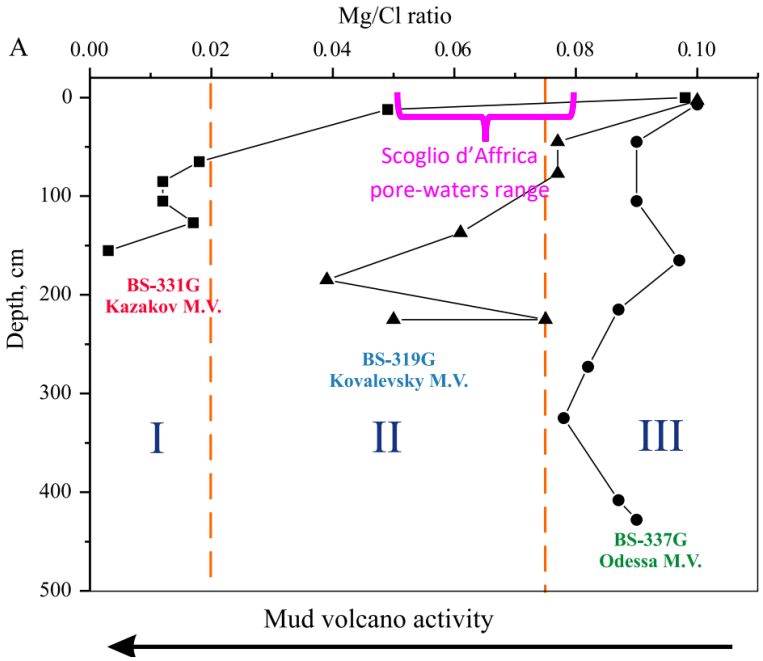

Figure 35 - Three examples of Mg/Cl distribution: I—drastic decrease indicating high content of mud volcano fluids; II—mixed sea water and mud volcano fluids; III—small variation from initial seawater composition, form Mazzini et al., 2004.

Considering also previous data, the hypothesis that MVs fluid flow was not very active at the moment of sampling can be discarded for two reasons: (i) as visual observation over the years demonstrated, the emissions at mound 2 are constant; (ii) the presence of deep fluids is verified by Mg anomalies in pore-waters. Therefore, the most probable processes in action are both shallow mixing processes in the subsurface and in the water column between seawater and deep fluids. This would contribute significantly to reduce the salinity of emitted fluids in the water column. In general, the farther away from the mud volcano, the more mixing processes between seawater and fluids emitted at depth increase.

5.3 Gas quantification

The estimated gas emitted from the three mounds reported in tables 2-3-4 suggests an analogy between mound 1 and mound 3, where the emitted gas during active phases is around $100 \cdot 10^3$ m^3 d^{-1}. Instead at mound 2 the gas flux is around $20 \cdot 10^3$ m^3 d^{-1}.
The difference of gas amount between mound 2 and mounds 1 and 3 could be justified by the fact that they have a different temporal activity. Mounds 1 and 3 emit a huge quantity of gas by explosive events in relatively short time, while mound 2 emits constantly.
Anyway, considering the estimated error (between 65 and 70%), the two measures could be comparable. It seems that following a major eruption event, with active phases still ongoing, the gas emission rates appear consistent across all three mounds.

In literature previous data in the area reported $30 \cdot 10^3$ m^3 d^{-1} at Mimosa 1 well (AGIP, 1987) and 700 m^3 d^{-1} for the area around Scoglio d'Affrica islet (Del Bono and Giammarino, 1968). At mound 2, the gas emission rate is similar to that observed at the Mimosa 1 well. However, the flux in the region studied by Del Bono and Giammarino (1968) is an order of magnitude lower. This could be explained by the fact that the emissions described by Del Bono and Giammarino (1968) were diffuse and not coincident with a mud volcano structure but in the middle of *Posidonia oceanica* meadows. Moreover, seagrass ecosystems, such as sediments colonized by eelgrass (*Zoster sp*.) and turtlegrass (*Thalassia sp.*) are recognized as important sources of methane to the atmosphere (Oremland, 1975; Garcias-Bonet and Duarte, 2017) with estimated emissions ranging from about 0.1 to 2.7 Tg (CH_4) yr^{-1} (Rosentreter et al., 2021; Garcias-Bonet and Duarte, 2017; Al-Haj and Fulweiler, 2020). These ecosystems have the ability to release significant quantities of labile organic carbon into the underlying sediments. In particular, a recent study revealed that *Posidonia oceanica* clearly contributes to methane release to the atmosphere (0.0003 to 0.033 Tg (CH_4) yr^{-1} for the Mediterranean Sea; Schorn et al., 2022). Differently from terrestrial peat ecosystems, no methane is produced from competitive substrates, such as hydrogen or acetate, as these substrates are likely used up by the abundant sulphate reducing bacteria. Methylotrophic methanogenesis is the sole detected pathway of methane production and together with fast advective and plant-mediated transport and with an inefficient microbial methane filter in these sediments, contribute to an elevated methane emission rate from seagrass sediments (Schorn et al., 2022). Significantly, the methane emissions into the water column and the methane-producing potential of the deceased seagrass sediment remained largely comparable to those of the living seagrass meadow, suggesting that methane production continues long after the living plant's disappearance (Schorn et al., 2022).
According to the above, both for the presence of *Posidonia oceanica,* that can influence the results, and for the different area and seabed structures, the gas flux considered by Del Bono and Giammarino (1968) is not comparable to the flux rate of mounds 1, 2 and 3.

Considering also the volume of the mud volcanoes (see results section), at Scoglio d'Affrica it is plausible that, despite the high error in the measurements, the major quantity of gas

and mud is emitted during huge eruptive events, as suggested by the volume of mounds 1 and 3 and the amount of gas estimated just after the emission events ($100 \cdot 10^3$ m^3 d^{-1}).
In order to calculate the methane emitted in the area, previous results of the gas analysis were considered. According to Saroni et al. (2020), the average methane percentage in the gas samples is 96.28 % of the total gas emitted. According to that, the total amount of methane emitted at Scoglio d'Affrica area from mound 1, 2 and 3, considering a hypothetical contemporary active phase of the three mounds, is about $98 \cdot 10^6$ m^3 yr^{-1}.

5.4 Emitted gas to the atmosphere and global budget

Weber et al. (2019) demonstrated that the rapid decline in CH_4 transfer to the atmosphere (due to diffusion processes in the water column) is observed in relation to the release depth and bubble size (Fig. 36). They also consider that the vast majority of bubbles escaping seafloor sediments (~99% by volume) are between 2 and 8 mm in diameter and the majority among these bubbles experience a loss of over 99% of their initial CH_4 content while ascending through a water column of 100 meters (Weber et al., 2019).

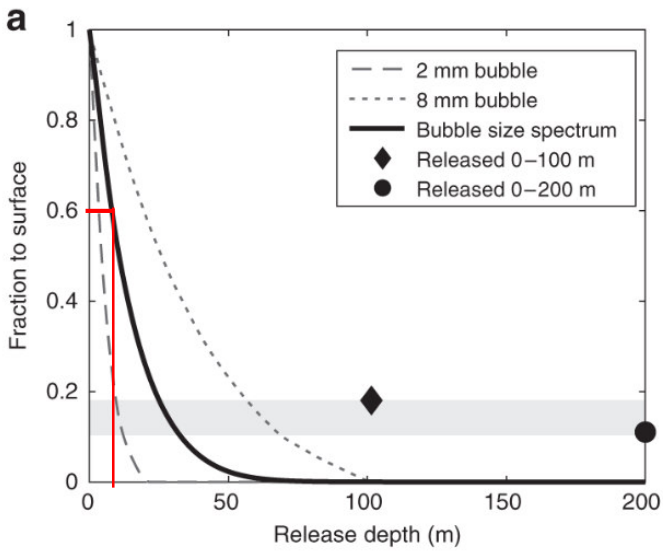

Figure 36 – Modeled transfer efficiency of CH_4 in bubbles from the seafloor to surface ocean, for 2 and 8 mm diameter bubbles, and integrated across a characteristic bubble size spectrum. Red lines represent 10 m depth (modified from Weber et al., 2019).

Considering that at Scoglio d'Affrica emissions are located approximately at 10 m depth and millimetric size bubbles prevail, it is possible to assume that at least 60% of the methane emitted reaches the atmosphere.
Considering a hypothetical contemporary active phase of mounds 1, 2 and 3, the total amount of methane emitted at Scoglio d'Affrica area is about $98 \cdot 10^6$ m^3 yr^{-1}. Anyway, taking into account the large error of the calculated emitted gas (between 65 and 70%) and the large uncertainties due to the different intermittent period of activity of the mud volcanoes, it is not possible to assume this value as the exact contribution of Scoglio d'Affrica MVs to the global greenhouse gas emissions budget. The gas flux has indeed been assessed, taking into account the active phases of the MVs.

5.5 MVs morpho-dynamics

Limited research in the literature has uncovered alterations in seabed morphology associated with the activity of submarine mud volcanoes (MVs) through the repeated mapping of the same seafloor region (Foucher et al., 2010; Feseker et al., 2014). Other few studies analyze vertical movements over time at onshore MVs (Antonielli et al., 2014; Kusumoto et al., 2015).

Foucher et al. (2010) and Feseker et al. (2014) made a comparative analysis of the bathymetry and backscatter maps at the Håkon Mosby Mud Volcano located at 1250 m water depth in the Barents Sea during 2003 and 2010. According to them, subtle changes in the overall crater morphology of the mud volcano are interpreted as outcomes of mud eruption events. Abrupt uplift of the seabed, occurring at rates ranging between 0.2 and 0.7 m h^{-1}, has been identified. Across four major events over years, the cumulative uplift reached 1.3 m. However, gradual deflation of the seafloor occurred between these events. By 2010, the seafloor had only gained 0.2 m in increased height compared to the start of the time series in 2009.

They also suggested that the lack of evidence of significant mud accumulations within the mud volcano, and the lack of indications of mud flow outside of the volcano imply that the substantial upward and lateral movements of mud recorded must be counteracted by an equal and opposite recycling of mud volume within the mud chamber of the mud volcano, so that the overall volume is conserved. This may involve processes such as the sinking of degassed and cooled sediment layers, which would be relatively dense at the outer periphery of the mud volcano.

Antonielli et al. (2014) detected ground deformation related to the activity of the onshore mud volcanoes of Azerbaijan and compared it with known deformation in magmatic systems. The displacement patterns, observed from 2003 to 2005, primarily manifest as uplift, reaching cumulative values up to 20 cm at the Ayaz–Akhtarma mud volcano and 10 cm at the Khara-Zira Island mud volcano. Conversely, certain sectors of the mud volcanoes structures experience subsidence.

Significant deformation events are linked to surface brittle faulting and fracturing and are attributed to fluid pressure and volume fluctuations observed in two scenarios. First, they present as pre-eruptive uplift in connection with main eruptive events; second, short-lived deformation pulses interrupted periods of quiescence.

Another recorded movement during MVs evolution is the formation of a subsidence caldera. Calderas take place as a consequence of an eruption event. They can encompass the complete MV edifice (Camerlenghi et al., 1995; Ivanov et al., 1996) revealing also peripheral ring fault systems (Prior et al., 1989; Neurauter and Bryant, 1990; Davies and Stewart, 2005; Mazzini et al., 2009; Loher et at., 2018a), or they can form as summit calderas on top of the extrusive edifices (Evans et al., 2008).

The 100 m high twin cones of Venere mud volcano, for instance, situated at 1,600 m water depth within the Squillace Canyon, are surrounded by a subsidence caldera composed of

inward-dipping ring faults. Gas bubble emissions and ecosystems supported by chemosynthesis have been observed at various locations around the caldera (Loher et al., 2018c). The caldera walls measure heights from 11 to 42 m in the east and less than 1 m in the south and west. Assuming an average and symmetric caldera subsidence on the order of 25 m and given the caldera diameter of 3 km, this conceptual caldera corresponds to a cylinder shape with the same volume as the MV edifice. Due to compaction, loss of pore fluids upon extrusion, interbedded marine sediments, and caldera infilling, these estimates are subject to large uncertainties. Nevertheless, they suggest the same order of magnitude between subsurface sediment mobilization, edifice buildup, and caldera subsidence (Loher et al., 2018c).

5.5.1 Vertical movements over the period 2017-2019 at mound 3

The increase in depth that characterized mound 3 between 2017 and 2019, is well represented in the difference surface derived from the bathymetric maps (fig. 37). It shows that the central part of the mound reached a vertical difference up to +2.5 ± 0.8 m (fig. 37). As a matter of fact, in 2017 the shallowest point of the crater reached -7.5 ± 0.4 m b.s.l.. The same point in 2019 was at -10.0 ± 0.4 m b.s.l.

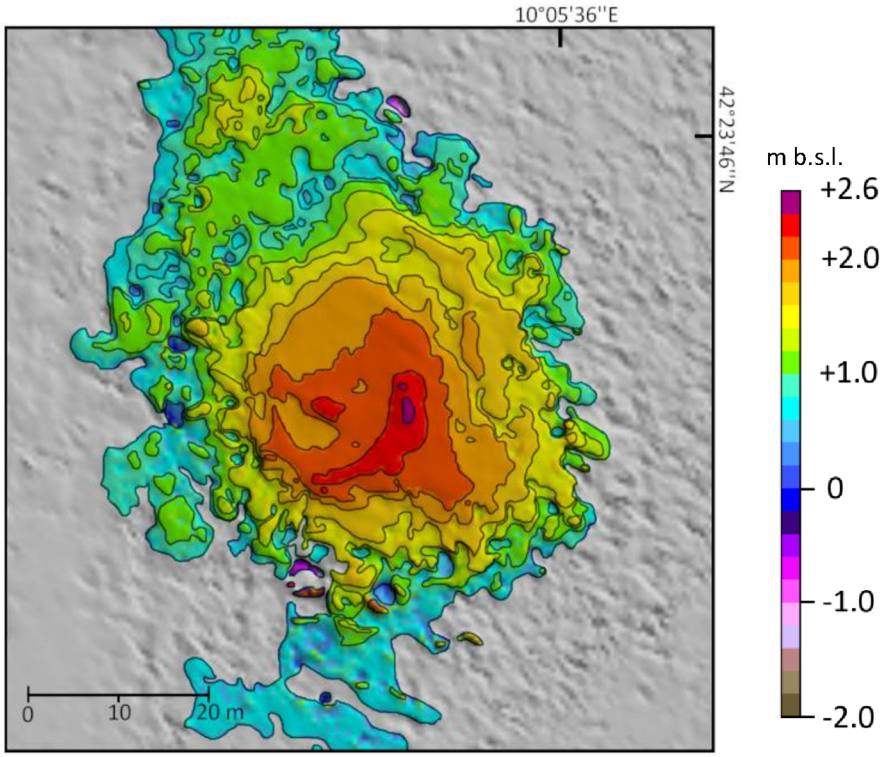

Figure 37 – Difference surface between 2017 and 2019 at mound 3.

This decrease of the central part of the crater could be controlled by several dynamics. Post-extrusive subsidence and caldera formation (Prior et al., 1989; Bonini, 2008; Evans et al., 2008; Mazzini et al., 2009) have been argued to result from sediment mobilization, fluidification and material withdrawal in the subsurface (Woolsey et al., 1975; Van Rensbergen et al., 2003; Perez-Garcia et al., 2009), erosion of the side walls of the conduit

(Brown, 1990), reductions in pore fluid pressures (Fukushima et al., 2009), extrusive loading (Galindo-Zaldivar et al., 1996; Blouin et al., 2020; Cartwright et al., 2023) and formation of deplation zones (Kirkham et al. 2017; Dupuis et al., 2019; Cartwright et al., 2023).

As mud volcanoes are the outcome of sedimentary eruptions of liquefied material, the occurrence of mud volcanism is evidently tied to the establishment of overpressure, a factor that aids in mobilizing sediment by weakening the strength within the overpressured layer. This overpressure is crucial for the extrusion of mud, serving as a necessary counterbalance to the mud load (Deville et al., 2009).
Overpressure generation is linked to fast sedimentation rates leading to compaction disequilibrium (sedimentary loading) and tectonic movements. Tectonic activity plays a crucial role in mud volcano development. Shear stresses for example can create significant overpressures in sedimentary rocks, causing undercompacted sediments to flow under critical state conditions (Yassir, 1987).

According to Deyhle et al. (2003), the depth and origin of mud volcanic processes could involve both relatively shallow (e.g. 1-2 km below seafloor in the Mediterranean Ridge mud volcanoes) and deep remobilization of material (e.g. 3-5 km below seafloor in the Anaximander Mountains).
At Scoglio d'Affrica MVs, sediment mobilization and MVs formation probably occurred due to a combination of the overpressure generated by the high sedimentation rate and the extensional tectonic activity prevailing over the years. The recent eruption events in the area, and especially the documented event in 2017, expelled a quantity of fresh mud clearly visible during ROV observations of the top of the mound in 2017 and deductible from the extension of the lobate flows accumulated at slopes (more than 350 m from the edge of the crater, see fig. 16). Although some rock samples were taken during hydro-oceanographic campaigns, the poor conservation state of the fossils in the mudstones samples prevents in-depth classification, thus it was neither possible to date them nor correctly and consistently correlate them with the stratigraphical units (Saroni et al., 2020). Sediment and gas mobilization and expulsion to the surface implicate a volume loss in the mud chamber/stratigraphic units that implement a general subsidence. As Woolsey et al. (1975) reported in their experiments, gas-filled cavities with arched roofs formed below the surface and the fluidization cells beneath these voids ascended slowly. Concentric subsidence occurred around the conduit, and surface blocks were transported along its margins.

Apart from sediment mobilization, subsidence can be caused by the weight of the extruded mud. After the 2017 eruption event, an overburden set in place on the seabed and especially on the top of the mound 3. In order to have a general idea of the amount of material expelled, we can consider the difference volume in the crater of mound 3 between 2017 and 2019. The overall volume can be approximated to a tronco-conical shape with a top area of ~170 m^2, a bottom area of ~2370 m^2 and an average height of ~2 m. The resulting volume is about $2 \cdot 10^3$ m^3 with a consequent extrusion rate of mud and gas of

1000 m^3 yr^{-1}. Milano and Napoli MVs in the Eastern Mediterranean rates from 2000 to 8000 m^3/year and 6000 to 15000 m^3 yr^{-1} for the respective mud breccia extrusion (Kopf, 1999; Wallmann et al., 2006). Anyway, calculation of loading contribution in literature demonstrates that it is difficult to explain the observed meters of decrease solely by the loading effect. Fukushima et al. (2009) for example calculate a possible maximum displacement of 29.0 cm at LUSI mud volcano caused by the weight of the mud expelled. Considering the estimated volume of the expelled gas ($5 \cdot 10^7$ m^3 yr^{-1}), which is four order of magnitude bigger than the estimated depletion volume, it is possible to affirm that the gas expulsion clearly contributed to the depletion of the area.

The mechanism of crater evolution at mound 3 between 2017 and 2019 could be explained as a combination of collapse (due to sediment and gas mobilization and extrusive loading) and compaction following the 2017 eruption event. This combination of processes is similar to the hypothesis in Mazzini et al. (2009), with a gradual sagging of the fluidized sediments at the end of each eruption event and the consequent squeezing out of the remaining fluids in the fluidized sediments. Moreover, loss of volume of the freshly erupted mud and the consequent compaction of it has been documented during 2018 campaign and in the comparison of visual observations between 2017 and 2021.

Other mechanism such as erosional processes caused by bottom currents are not consistent with the area. Offshore MVs have been found to possibly be shaped by bottom currents when they represent a topographic barrier and impact significantly on the bottom current circulation, such as the Mediterranean Outflow Water (MOW) (Vandorpe et al., 2016; Sanchez Guillamon et al., 2023). These conditions are not present in the Scoglio d'Affrica area.

5.5.2 Vertical movements over the period 2019-2022 at mound 3

The decrease in depth (inflation of the seabed) that mound 3 underwent over the years, is well represented in the difference surfaces between 2019 and 2022 derived from the bathymetric maps (fig. 38). The difference surface shows that the crater of the mound had a decrease in depth between 2019 and 2022 of a maximum of -1.8 ± 0.8 m amplitude (fig. 38).

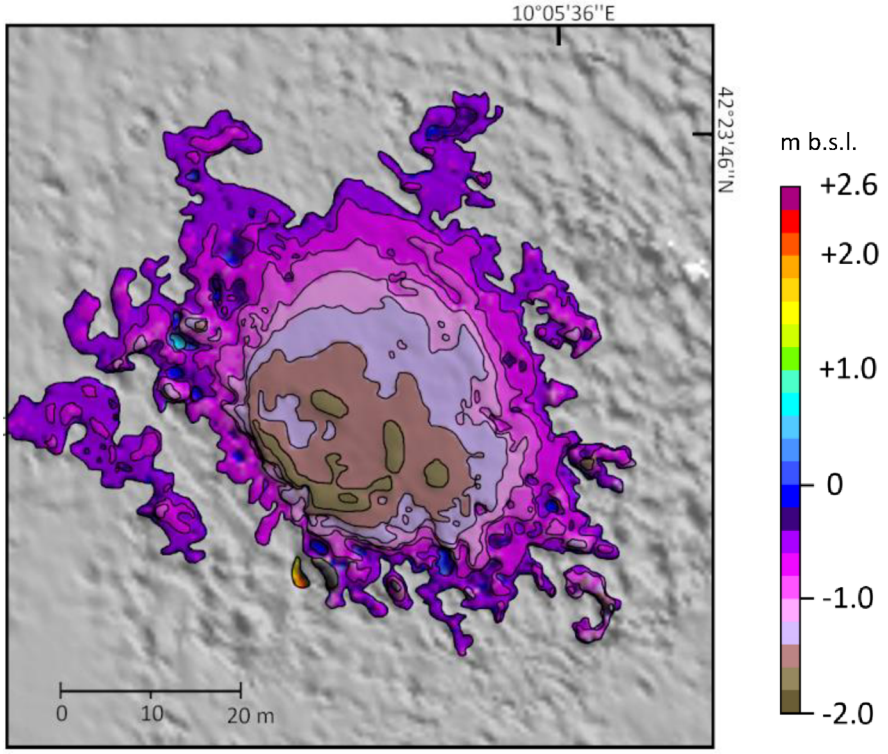

Figure 38 – Difference surface between 2019 and 2022 at mound 3.

Concerning the inflation of seabed, Woolsey et al. (1975) conducted a series of experiments utilizing fluidization techniques. The experiments demonstrated the early development of surface doming accompanied by ring and radial fractures due to the migration of fluidized sediment towards the surface.

Moreover, several studies involve self-sealing in evolutionary schemes for cold seeps (Hovland, 2002; Bayon et al., 2009; Loher et al. 2018b), also followed by fracturing (Bahr et al., 2010), that can cause an overpressure and a consequent inflation of the seabed.

Indeed, the presence of methane fluxes in seafloor areas is often associated to carbonates (or methane-derived authigenic carbonates) caused by the anaerobic oxidation of methane by sulfate ions (Boetius et al., 2000; Hiruta and Matsumoto, 2023).

At the Venere MV site, authigenic carbonates are present in multiple cold seep locations along the MV periphery, aligning with subcircular patches exhibiting notably high backscatter intensity (Loher et al., 2018c). Hydroacoustic observations suggesting gas flare presence along the perimeters of high backscatter patches have been interpreted as indicating the release of gas bubbles at the edges of carbonate pavements in other methane emission locations (Naudts et al., 2008; Naudts et al., 2010; Römer et al., 2014).

In general, these accumulations can reduce the overall permeability of sediments over time by carbonate precipitation in the pore space, inducing a sealing process in the primary migration pathways and consequently an increasing in pressure (Bahr et al., 2007; Hovland, 2002; Bayon et al., 2009).

Between 2019 and 2022 the difference volume inside the crater is about $1 \cdot 10^3$ m^3, considering an average height of ~1.4 m, which is less than the difference reached between 2017 and 2019, as also underlined in the difference surface image (fig. 38). This could be explained by two hypotheses:

1. the system is charging and the crater has not yet reached the maximum height;
2. another eruption has already occurred and the seabed is getting lowered again.

Considering that the bathymetry did not show new sign of gravitative morphologies in 2022, the second hypothesis is discarded.

5.5.3 Morpho-dynamic evolution over the period 2017-2022 at mound 3

At mound 3 the comparison of the bathymetric maps produced in 2017, 2019 and 2022 (fig. 18-19-20) shows that the morphology of the outer regions of the mud volcanoes has not changed significantly through years; in contrast, the crater at mound 3 has undergone several changes in the bathymetry of the seabed (fig. 39).

The deflation of the seabed at mound 3 occurred after the eruption event in 2017 and the following inflation, especially of the south-west part of the crater, occurred between 2019 and 2022. It is plausible to consider these five years as a complete cycle of an eruption event and that in 2022 or later on another eruption occurred or will occur in the area. Antonielli et al. (2014) observed that ground uplift can manifest up to one year before the eruption. This cycle of eruption is consistent with other mud volcanoes recurrent emission events such as the onshore Lokbatan MV (Mazzini et al., 2021). Cyclic patterns at frequencies of decades are reported for large and catastrophic events, while patterns of minutes are typical during quiescent phases for gas and mudflows (Deville and Guerlais, 2009).

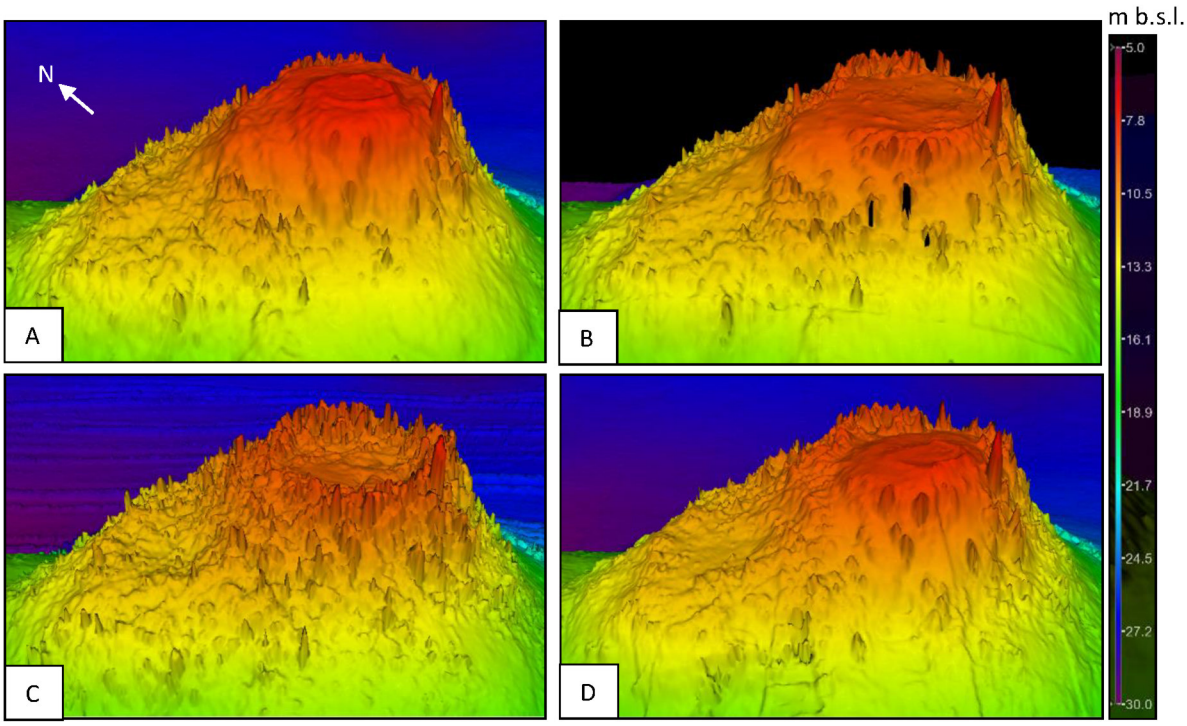

Figure 39 – 3D reproduction of mound 3 (5x vertical exaggeration) in 2017 (A), 2018 (B), 2019 (C) and 2022 (D).

After the cycle of deformation occurred between 2017 and 2022, the seafloor had only gained less than 1 m in decreased height, as visible in the difference surface between 2017 and 2022 (fig 40).

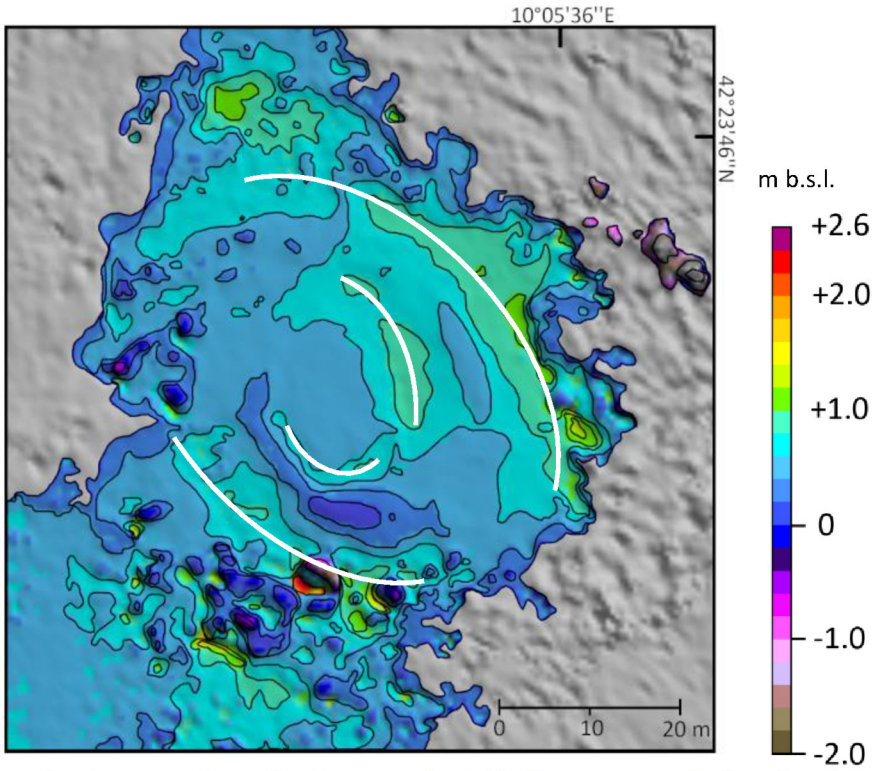

Figure 40 – Difference surface between 2017 and 2022 at mound 3. White lines represent the lineation of maximum movements.

While the characteristic fault system observed around the structure and within the crater of other submarine mud volcano calderas (e.g., Venere MV; Loher et al., 2018a) is not distinctly evident in this case, there is a possibility of an underlying system of fractures in the subsurface. This inference arises from the observed predominant elliptical vertical movements on the difference surfaces, potentially attributable to the existence of a cylindrical mud conduit, as documented for LUSI MV in Fukushima et al. (2009).
Moreover, figure 40 shows that also external part of the crater is interested by overall decreasing concentric vertical movements, suggesting the formation of the typical subsidence around the MV edifice (Perez-Garcia et al., 2009; Foucher et al., 2010; Feseker et al., 2014).

In conclusion, mound 3 is characterized by the presence of a principal crater of emission surrounded by an evident rim and secondary peripheral seeps. The crater undergoes cyclic ground deformations of at least 5 years connected to the major eruptive events that are recorded by the lobate deposits in the mound flanks.

5.5.4 Vertical movements over the period 2017-2022 at mound 2

The bathymetry of mound 2 remains essentially stable over the years, with the exception of 2022, when a peak that reaches a maximum of -9.3 ± 0.4 m depth appears in the northern part of the mound (in 2019 the same point was at -11.0 ± 0.4 m depth). The peak is about 10 m of diameter with a difference surface of about -1.7 ± 0.8 m. The hypothesis of a diversion in the fluid migration pathways from mound 3 conduit toward mound 2 conduit, with the consequence loss of feeding material at mound 3, is discarded because of the absence of other substantial morphological changes in the area. The corresponding volume of the peak could not justify the difference volume occurred at mound 3 between 2017 and 2019.
The formation of the new cone is more probably due to the fact that the expulsion of the fluids in the last tens of metres close to the surface generates several conduits corresponding probably to a fracture system. The migration dynamics in the fracture system can cause changes in the fluid flow at short period of time and also changes in the location of the seeps.

5.5.5 Absence of vertical movements over the period 2017-2022 at mounds 1, 2 and 4

Fig. 41 shows the bathymetry evolution at mound 1 from 2017 to 2022. During these five years there were no substantial changes in the morphology of the area.

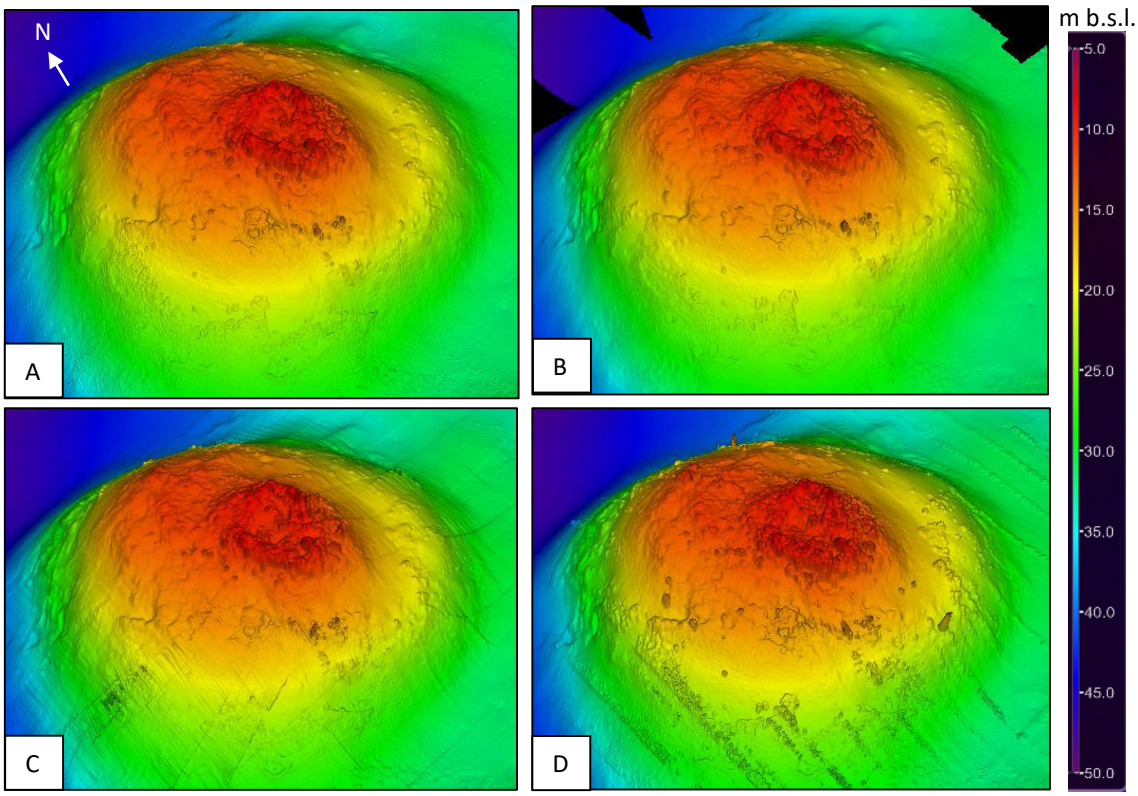

Figure 41 – 3D reproduction of mound 1 (5x vertical exaggeration) in 2017 (A), 2018 (B), 2019 (C) and 2022 (D).

Mound 1 showed a similarity to mound 3 during 2011 emission event, when mud flows and several emission points were detected, but, differently from mound 3, there were no recent changes in morphology. In addition, the emission activity was much reduced during 2018 campaign.

This phenomenon could be explained by the intermittent activity of the MV due to the recharge of the system (dormant phase), as reported in literature. Historical data onshore Trinidad, for example, reported that mud volcanoes can have different phases of activity, including, for some of them, catastrophic events followed by a progressively decreasing activity between two eruptions (Yassir, 1987; Deville and Guerlais, 2009; Mazzini and Etiope, 2017). Furthermore, based on the historical data in Deville and Guerlais (2009), it seems that each eruptive mud volcano experiences its own distinct period of catastrophic activity, that can last for more than 10 years, consistently with mound 1 MV at Scoglio d'Affrica (fig. 42). This period varies significantly from one volcano to another. Overall, their observations indicate that mud volcanoes exhibiting a consistently and continuously high rate of mud expulsion have not been identified as strongly eruptive. This is the case of mound 2, that shows a continuous activity over the five years monitored. The only morphological change in the area was detected in 2022, as already previously described. As in Foucher et al. (2010) and Feseker et al. (2014), the lack of indications of mud flow

outside of the volcano edifice at mound 2 could imply an overall conservation of the volume.

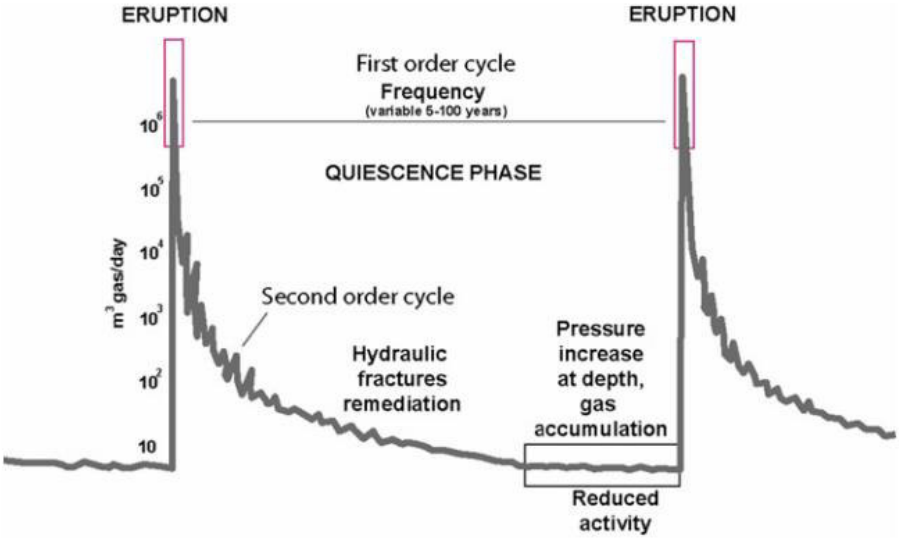

Figure 42 – Conceptual sketch of over-imposed cycles of activity of mud volcanoes in which catastrophic eruptions occurred (from Deville and Guerlais, 2009).

Mound 4 also does not reveal any morphological change between 2017 and 2022 (fig. 43). In this case there is no evidence of the presence of recent mud flows from the bathymetry. During 2018 campaign Van Veen grab sampler were used at the top of the mound revealing the presence of *Posidonia oceanica* and sand-gravel-mud sediments. The mound presents significant fracturing at the top and at the N-W slope bottom. It could be possible that the activity of the mound diminished over time and therefore the structure collapsed creating fractures and depression forms. Multibeam echosounder during 2019 surveying revealed the presence of flares on the south-west part of the top of the mound, meaning that some emissions are still present and that the mud volcano is not completely extinct.

m b.s.l.

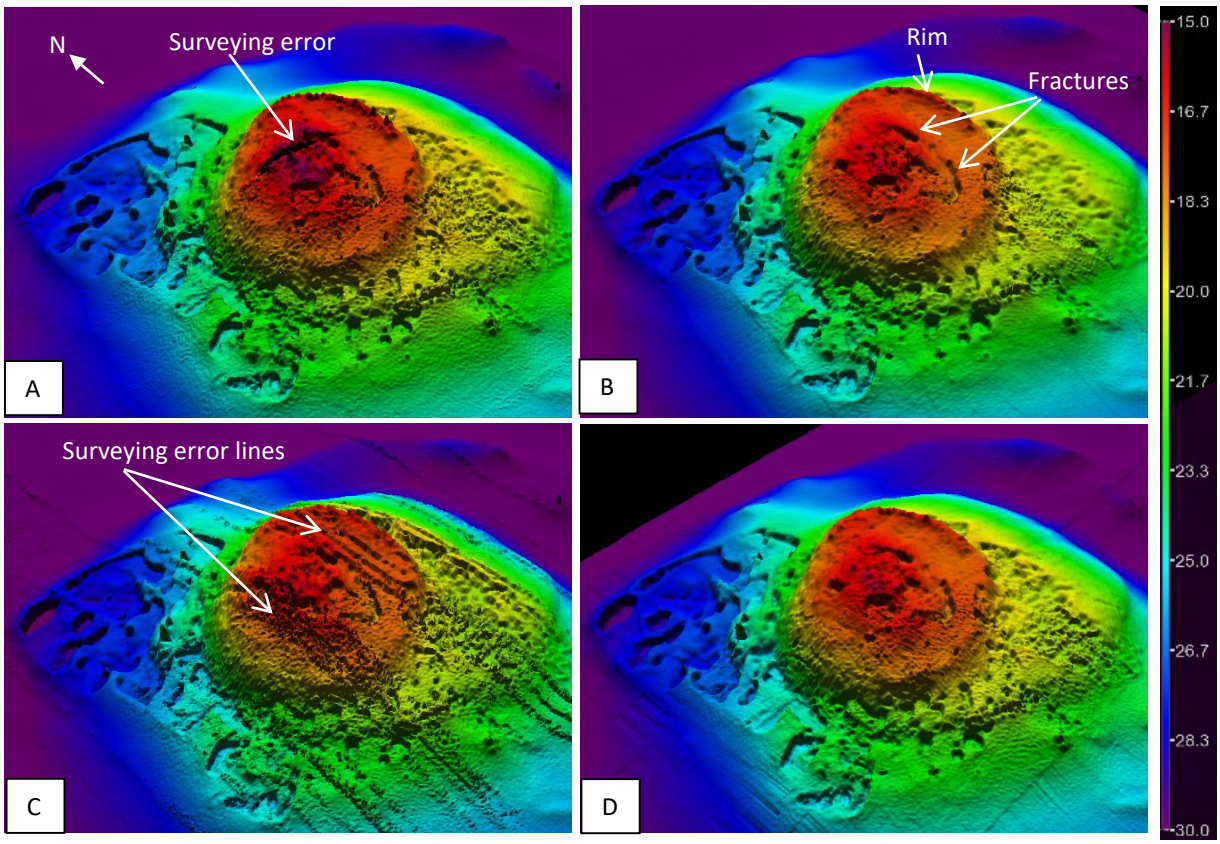

Figure 43 – 3D reproduction of mound 4 (5x vertical exaggeration) in 2017 (A), 2018 (B), 2019 (C) and 2022 (D).

6. CONCLUSION

6.1 MV morpho-dynamics

Visual and acoustic observations during idro-oceanographic campaigns over five years confirm the existing evidence of four mounds corresponding to Scoglio d'Affrica MVs. The emitted gas is dominated by methane and it involves the mobilization of instable sedimentary rocks (mud expulsion) and the presence of breccia. Other deep fluids emitted are in minor quantity, because there were no detected anomalies in salinity and conductivity in the water column. All the emissions do not show significant changes in temperature compared to the average seawater temperature, so they can be considered as cold seeps.

According to our observations and results the emission activity correspond to a coexistence of a shallow and a deep dynamic.

6.1.1 Deep dynamic

The faults system in the Scoglio d'Affrica area (Cornamusini et al., 2002; Barletta et al., 1969), could be considered the initial preferred path for fluids and sediment to rise to the surface. All four mounds are indeed aligned north-south, as one of the two preferred fault orientations derived by the overall result of the crustal stretching in the Northern Tyrrhenian Sea (Keller and Coward, 1996 and references therein).

The minor thermogenic component of the emitted gas indicate that methane also originate at > 1800 m depth. The gas could be stored in a deep reservoir in Eocene deposits and rises probably thanks to the fault systems in the area mixing with the shallower secondary microbial methane.

6.1.2 Shallow dynamic

The emitted methane mostly originates by secondary microbial processes at a depth < 1600 m and it is stored at shallow depth in Miocene-Oligocene deposits. Together with the fluidized sediment, this reservoir is considered to be mainly responsible for seabed uplift in pre-eruptive phase and subsidence during quiescent phases at mound 3, leading to a vertical difference up to 2.5 m. This cyclicity of fluid migration within the mud volcano conduits leads to predominantly concentric vertical movements that show the typical system of faults and fractures of calderas. The presence of a system of fractures justifies the fact that shallowing mixing processes between interstitial seawater and deep fluids prevail. The overall depletion volume observed at mound 3, approximately $2 \cdot 10^3$ m^3 over two years, cannot be adequately explained by a mere overburden in place. Furthermore, the calculated volume of the expelled gas ($5 \cdot 10^7$ m^3 yr^{-1}) following a primary eruption is four orders of magnitude greater than the estimated depletion volume. Therefore, it can be asserted that gas expulsion significantly contributed to the depletion of the area. The evolution of the crater at mound 3 from 2017 to 2019 can be attributed to a combination of collapse and compaction mechanisms.

The shallow reservoir is also responsible for the little morphological changes at mound 2, due to alterations in fluid flow and the relocation of seep locations according to migration dynamics within the fracture system located in the final tens of meters near the surface.

6.2 MV undersea features

Different dynamic during fluids upwelling led to two type of undersea features represented by mound 2 and mound 3. Moreover, a type 3 of undersea feature can be identified as an extinguishing mud volcano represented by mound 4.

6.2.1 Type 1 (Mound 2)

Type 1 is characterized by the following features:

- presence of several mud cones structures (at least ten) and smaller seepages;
- diffusely expulsion of the gas in small quantities ($8 \cdot 10^6$ m^3 yr^{-1});
- absence of mud flow deposits over the flanks of the mound;
- localized variations of the seabed due to the shallow fracture system dynamics;
- continuous emission of fluids.

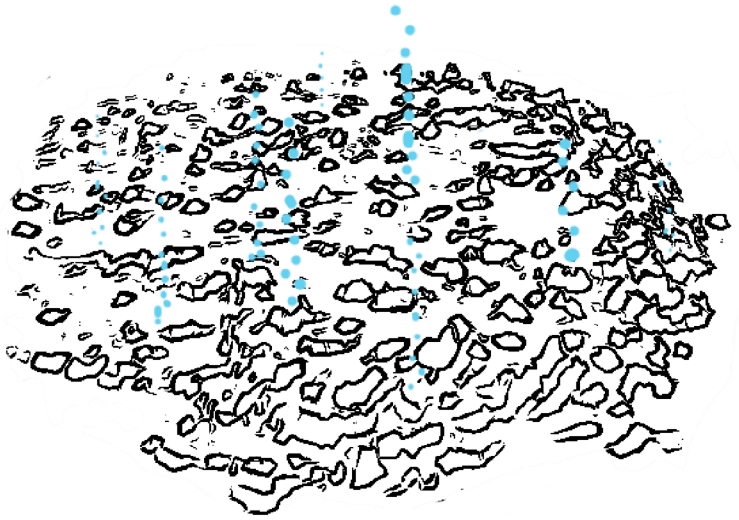

Figure 44 – 3D schematic representation of type 1 seafloor.

6.2.2 Type 2 (Mound 3)

Type 2 is characterized by the following features:

- presence of a single crater of emission and a defined rim;
- major quantity of gas and mud emitted ($100 \cdot 10^3$ m^3 d^{-1});
- presence of records of lobate flows in the flanks of the volcano;
- ground deformation associated to the mud flowing in shallow reservoirs (pre-eruptive vertical uplift and subsidence);
- cyclic vertical movements of years (at least 5 years) linked to explosive eruption events.

Figure 45 – 3D schematic representation of type 2 seafloor.

6.2.3 Type 3 (Mound 4)

Mound 4 differs from the other mounds in the area because presents significant fracturing at the top and at the N-W slope bottom. It has also a flat top compared to the other mounds. I suggest that these characteristic are due to a reduction of the eruption activity with a consequent collapse of the structure and prevalent erosion processes. The hypothesis is consistent with the presence of *Posidonia oceanica* at the top of the mound, suggesting a long inactive phase that permitted the colonization of the area by the seagrass.

Type 3 is characterized by the following features:

- presence of a defined rim and a flat top;
- presence of fractures and depressions both at the top and in the flanks of the volcano;
- absence or very reduced gas emission;
- absence of recent mud flow deposits over the flanks of the mound;
- presence of seagrass colonization.

Figure 46 – 3D schematic representation of type 3 seafloor.

6.3 Evolution model of the MV at mound 3

This study enhances the evolutionary model of a mud volcano by incorporating a depiction of the dynamics occurring post-formation. Building upon the representation of mud volcano formation in Mazzini and Etiope (2017) (fig. 47), figure 48 introduces two additional stages depicting the establishment of cyclic events following its formation and introducing a shallow dynamic into the system (fig. 48E-F). During a MV formation, usually tectonic forces lead to the accumulation of fluids and sediments in underground chambers, creating a pressurized system that seeks release through the mud volcano vent.

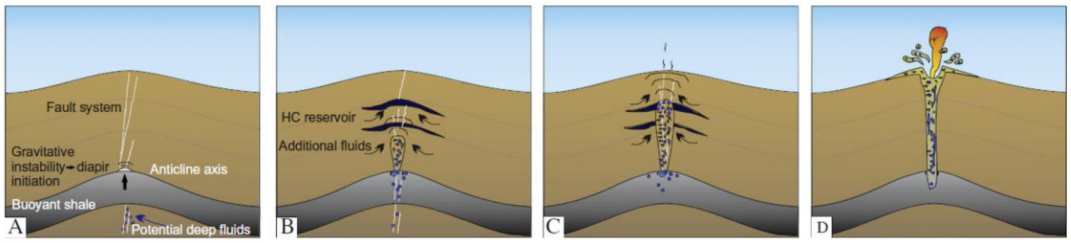

Figure 47 – Schematic formation of a mud volcano (from Mazzini and Etiope, 2017).

The new model is based on the results of mound 3 dynamics over five years. The model involves a shallow mud and gas chamber in the Miocene-Oligocene deposits that is compliant with the geochemical results of the analysed gas (Saroni et al., 2020) and the gas found in AGIP wells at Scoglio d'Affrica area and a deeper reservoir of thermogenic methane. The generation and migration of these hydrocarbons contribute to an increase in pore fluid pressure, influencing sediment mobilization and seabed deformation.

The considered cycle begins after a violent eruption event similar to the one that happened in 2017, when a column of gas, mud and water of 10 m height a.s.l. was seen by a fisherman (fig. 48D). After the eruption, an overburden subsidence is induced by degassing, dewatering and loss of volume of the freshly erupted mud.

The fracture system that opened during the eruption undergoes partial remediation over several years or even decades. The closure of the fracture system and the compaction

of surface or shallow-subsurface sediments enables the retention of fluids associated with a subsequent pressure increase. A rise of the seabed follows, caused by the generated overpressure, setting the stage for a potential new eruption (fig. 48F).

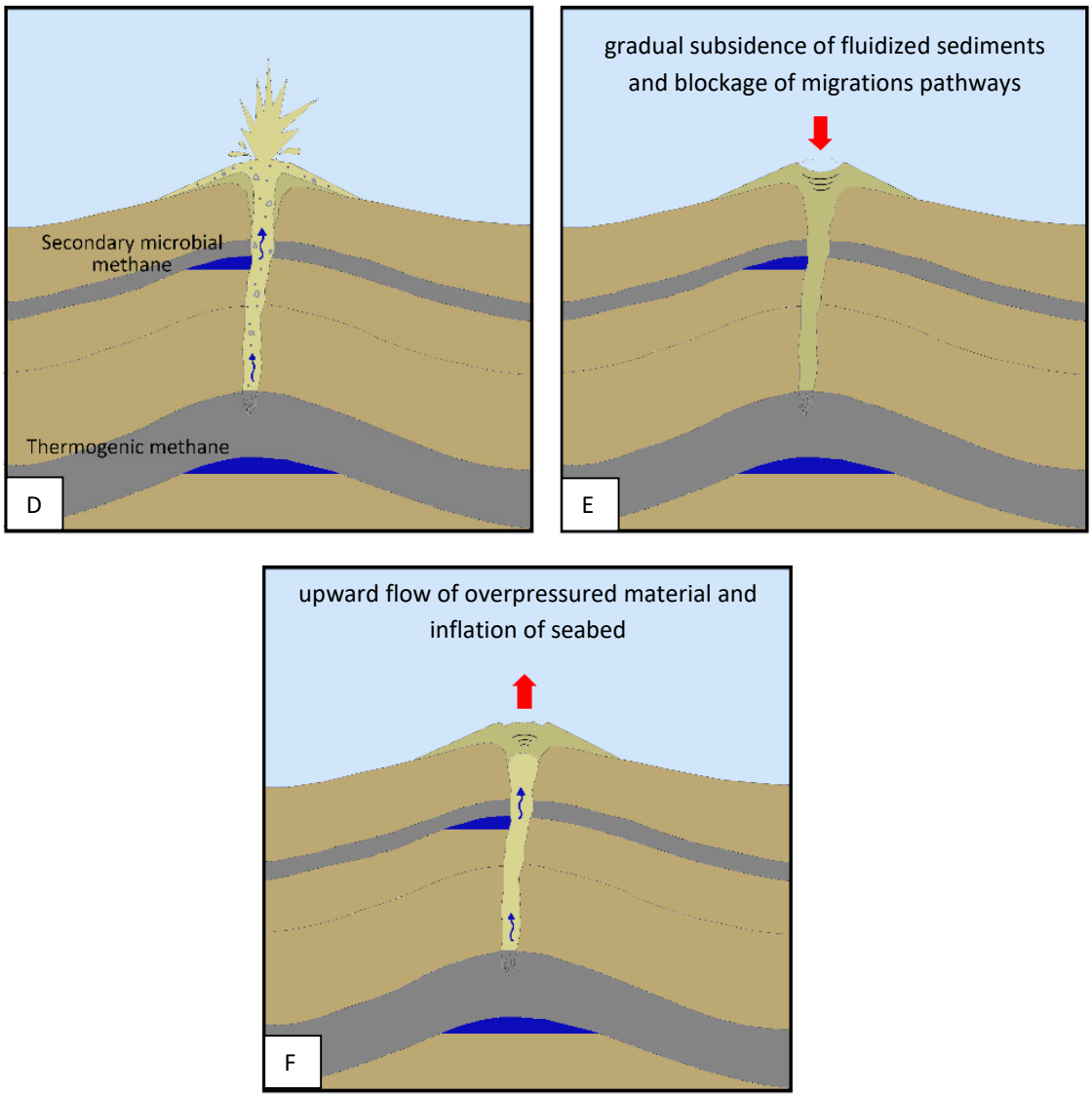

Figure 48 – Evolution model of the mud volcano at mound 3 over five years.

6.4 Global implications of the research

This study contributes to the limited research currently present in the literature of monitoring of mud volcanoes' seafloor and provides insights on their dynamic evolution. The results of this study underscore the importance of repeated monitoring of mud volcano systems in the marine environment and the effectiveness of a multidisciplinary approach, especially, when there is a combination of shallow water, violent eruptive events and human presence that could generate a hazard, as in the case of the Scoglio d'Affrica area.

The obtained findings establish evidence for preventing violent eruptive events by focusing on the activity, the morpho-dynamics and the undersea features of the mud volcano, especially at mound 3, and they may be useful in mitigating navigation safety.

It can be asserted that in the Scoglio d'Affrica mud volcano system, two mounds (mound 1 and 3) should be carefully monitored because of the evidence of violent eruptive events. Differently from mound 1, that is experiencing a quiescent period lasting minimum 10 years, mound 3 follows a 5-year cycle of activity and it was possible to model its evolution by introducing the establishment of cyclic events following its formation and the presence of a prevailing shallow reservoir responsible for ground deformation. Mound 2 can be considered less dangerous due to the continuous emission of gas and mud, while mound 4 is experiencing an inactive phase.

These results show that even in the same mud volcano system there can be different type of and temporal activities, confirming the complexity of a direct monitoring approach. The shallow water setting of the Scoglio d'Affrica allowed the validation with visual data of the high-resolution data collected by the multibeam acoustic echosounder and the correlations made between undersea features and mud volcano dynamic, confirming the fact that this technique can also be applied to monitor deep-water environments.

In fact, the undersea feature types identified in this study are representative of different activities and dynamics of a mud volcano and they can also be applied to other submarine mud volcanoes, found in both shallow and deep waters. In particular, the type 3 of undersea feature can be useful to identify inactive/extinguishing mud volcanoes, while type 1 and 2 represent different shallow dynamics during fluids upwelling: a continuous emission activity with several shallow fractures from which the gas and the mud are emitted (type 1) and a more consistent but intermittent emissive activity coming from a shallow reservoir and a preferred emission conduit (type 2).

Finally, the quantification of the gas emitted at Scoglio d'Affrica points to the need for repeated monitoring in order to reduce uncertainties regarding submarine gases contribution to the global emission budget. Indeed, considering a hypothetical contemporary active phase of mounds 1, 2 and 3, the total amount of methane emitted at Scoglio d'Affrica area is about $98 \cdot 10^6$ m^3 yr^{-1}. However, it's worth mentioning that mound 1 is experiences a quiescent period lasting at least 10 years, whereas mound 3 follows a 5-year cycle of activity.

A more realistic calculation of the contribution can be evaluated with the following assumptions:

- a density of methane of 0,668 kg m^{-3} (20°C, 1 atm);

- continuous emission of mound 2 ($8 \cdot 10^6$ m^3 yr^{-1});
- 15 years-cycle of mound 1 ($2 \cdot 10^6$ m^3 yr^{-1});
- 5 years-cycle of mound 3 ($11 \cdot 10^6$ m^3 yr^{-1});
- an average methane percentage of 96.28 % of the total gas emitted;
- 60% of the total methane emitted reaches the atmosphere.

The resulting methane emitted to the atmosphere is about 0.008 Tg yr^{-1}, which is the 0.03% relative to the total methane emissions emitted from submarine mud volcanoes far from the coast (27 Tg yr^{-1}; Milkov et al., 2003; Judd, 2004). This value can be considered underestimated because big eruption event of mound 1 and 2 are not included, only the post eruption residual active phase has been taken into account.

REFERENCES

AGIP S.p.A. (1987). Relazione tecnica relativa al secondo periodo di vigenza, Permesso E.R39.AG., Rel. GERC n.47/87, https://www.videpi.com/videpi/cessati/fascicolo.asp?titolo=60 (28/10/2023).

Al-Haj, A. N., Fulweiler, R. W. (2020). A synthesis of methane emissions from shallow vegetated coastal ecosystems, *Glob. Change Biol., 26*, 2988–3005.

Antonielli, B., Monserrat, O., Bonini, M., Righini, G., Sani, F., Luzi, G. (2014). Pre-eruptive ground deformation of Azerbaijan mud volcanoes detected through satellite radar interferometry (DInSAR), *Tectonophysics*, *637*, 163–177.

Bahr, A., Pape, T., Abegg, F., Bohrmann, G., van Weering, T., and Ivanov, M. K. (2010). Authigenic carbonates from the eastern Black Sea as an archive for shallow gas hydrate dynamics - Results from the combination of CT imaging with mineralogical and stable isotope analyses: *Marine and Petroleum Geology*, *27* (9), 1819-1829. https://doi.org/10.1016/j.marpetgeo.2010.08.005

Bahr, A., Pape, T., Bohrmann, G., Mazzini, A., Haeckel, M., Reitz, A., and Ivanov, M. (2007). Authigenic carbonate precipitates from the NE Black Sea: a mineralogical, geochemical, and lipid biomarker study, *International Journal of Earth Sciences*, *98* (3), 677. https://doi.org/10.1007/s00531-007-0264-1

Bayon, G., Henderson, G.M., Bohn, M., 2009. U-Th stratigraphy of a cold seep carbonate crust. *Chem. Geol., 260*, 47–56. http://dx.doi.org/10.1016/j.chemgeo.2008.11.020

Barletta, S., Del Bono, G. L., Salvati, L. (1969). Nota preliminare sui lavori geomorfologici e geominerari subacquei effettuati dal Servizio Geologico d'Italia dal 1964 al 1969. *Boll. Serv. Geol. It. CX*, 83-89.

Bernard, B., Brooks, J.M., Sackett, W.M. (1977). A geochemical model for characterization of hydrocarbon gas sources in marine sediments. In: 9th Annual OTC Conference, vol. 2934, pp. 435–438.

Bernard, B.B., Brooks, J.M., Sackett, W.M. (1978). Light-hydrocarbons in recent Texas continental-shelf and slope sediments. *J. Geophys. Res.-Oceans, 83*, 4053–4061.

Blouin, A., Sultan, N., Pierron, A., Imbert, P., & Callot, J.-P. (2020). Evolution model for the Absheron mud volcano: from stratified sediments to fluid mud generation. *Journal of Geophysical Research: Earth Surface*, *125*, e2020JF005623. https://doi.org/10.1029/2020JF005623

Boetius, A., Ravenschlag, K., Schubert, C.J., Rickert, D., Widdel, F., Gieseke, A., Amann, R., Jørgensen, B.B., Witte, U., and Pfannkuche, O. (2000). A marine microbial consortium apparently mediating anaerobic oxidation of methane, *Nature*, *407*, 623–626. https://doi.org/10.1038/35036572

Bonini, M. (2008). Elliptical mud volcano caldera as stress indicator in an active compressional setting (Nirano, Pede-Apennine margin, northern Italy), *Geology*, *36*, (2), 131-134. https://doi.org/10.1130/G24158a.1

Bousquet, P., Ciais, P., Miller, J. B., Dlugokencky, E. J., Hauglustaine, D. A., Prigent, C., Van der Werf, G. R., Peylin, P., Brunke, E.-G., Carouge, C., Langenfelds, R. L., Lathière, J., Papa, F., Ramonet, M., Schmidt, M., Steele, L. P., Tyler, S. C., White, J. (2006). Contribution of anthropogenic and natural sources to atmospheric methane variability*. Nature 443*, 439–443.

Brown, K. M. (1990). The nature and hydrogeologic significance of mud diapirs and diatremes for accretionary systems. *Journal of Geophysical Research*, *95* (B6), 8969-8982. https://doi.org/10.1029/JB095iB06p08969

Camera dei Deputati, 24 settembre 1984. Resoconto stenografico (Allegato). IX Legislatura, 185° Seduta, p. 24. https://legislature.camera.it/_dati/leg09/lavori/stenografici/sed0185/rsi0185.pdf (28/11/2023).

Camerlenghi, A., Cita, M. B., Dellavedova, B., Fusi, N., Mirabile, L., and Pellis, G. (1995). Geophysical Evidence of Mud Diapirism on the Mediterranean Ridge Accretionary Complex, *Marine Geophysical Researches*, *17*, (2), 115-141. https://doi.org/10.1007/Bf01203423

Capaccioni, B., Tassi, F., Cremonini, S., Sciarra, A., Vaselli, O. (2015). Ground heating and methane oxidation processes at shallow depth in Terre Calde di Medolla (Italy): Observations and conceptual model. *J. Geophys. Res. Solid Earth, 120*(5), 3048-3064. https://doi.org/10.1002/2014JB011635

Carminati, E., Doglioni, C. (2012). Alps vs. Apennines: the paradigm of a tectonically asymmetric Earth. Earth Sci. Rev. 112, 67–96.

Cartwright, J., Kirkham, C., Espinoza, D., N., James, D., Hodgson, N. (2023). The evolution of depletion zones beneath mud volcanoes. *Marine and Petroleum Geology, 155*, 106351.

Casalbore, D., Ingrassia, M., Pierdomenico, M., Beaubienc, S. E., Martorelli, E., Bigic, S., Ivaldi, R., De Marte, M., Chiocci, F. (2020). Morpho-acoustic characterization of a shallow-water mud volcano offshore Scoglio d'Affrica (Northern Tyrrhenian Sea) responsible for a violent gas outburst in 2017, *Marine Geology, 428*, 106277.

Clarke, W.B., Jenkins, W.J., Top, Z. (1976). Determination of tritium by mass spectrometric measurement of ^{3}He. *Int. J. Appl. Radiat. Isot., 27* (9), 515–522.

Cornamusini, G., Lazzarotto, A., Merlini, S., Pascucci, V. (2002). Eocene-Miocene evolution of the north Tyrrhenian Sea. *Boll. Soc. Geol. It., Volume Speciale n. 1*, 769-787.

Cornamusini, G. and Pascucci, V. (2014). Sedimentation in the Northern Apennines–Corsica tectonic knot (Northern Tyrrhenian Sea, Central Mediterranean): offshore drilling data from the Elba–Pianosa Ridge. *International Journal of Earth Sciences, 103*, 821-842.

Cuffaro M., Billi. A., Bigi, S., Bosman, A., Caruso, C. G., Conti, Al., Corbo, A., Costanza, A., D'Anna, G., Doglioni, C., Esestime, P., Fertitta, G., Gasperini, L., Italiano, I., Lazzaro, G., Ligi, M., Longo, M., Martorelli, E., Petracchini, L., Petricca, P., Polonia, A., Sgroi, T. (2019). The Bortoluzzi Mud Volcano (Ionian Sea, Italy) and its potential for tracking the seismic cycle of active faults*, Solid Earth, 10*, 741–763. https://doi.org/10.5194/se-10-741-2019

Davies, R. J., and Stewart, S. A. (2005). Emplacement of giant mud volcanoes in the South Caspian Basin: 3D seismic refelction imaging of their root zones, *Journal of the Geological Society*, *162*, 1-4.

Del Bono, G. L., Giammarino, S. (1968). Rinvenimento di manifestazioni metanifere nelle Praterie di Posidonie sui fondi marini prospicienti lo "Scoglio d'Africa" nell'Arcipelago Toscano, *Atti Ist. Geol. Univ. Genova, VI* (1), 11.

Deville, E. P., Guerlais, S.-H. (2009). Cyclic activity of mud volcanoes: Evidences from Trinidad (SE Caribbean), *Marine and Petroleum Geology, 26* (9),1681-1691.

Deyhle, A., Kopf, A., Aloisi, G. (2003). Boron and boron isotopes as tracers for diagenetic reactions and depth of mobilization, using muds and authigenic carbonates from eastern Mediterranean mud volcanoes, *Geological Society London Special Publications, 216,* (1), 491-503

Dieckmann, V. (2005). Modelling petroleum formation from heterogeneous source rocks: the influence of frequency factors on activation energy distribution and geological prediction, *Mar. Pet. Geol., 22*, 375–390.

Dieckmann, V., Schenk, H. J., Horsfield, B., Welte, D. H. (1998). Kinetics of petroleum generation and cracking by programmed-temperature closed-system pyrolysis of Toarcian Shales. *Fuel, 77*, 23–31.

Dimitrov, L.I. (2002). Mud volcanoes–the most important pathway for degassing deeply buried sediments. Earth Sci. Rev. 59, 49–76.

Dupré, S., Woodside, J., Klaucke, I., Mascle, J., Foucher, J.-P. (2010). Widespread active seepage activity on the Nile Deep Sea Fan (offshore Egypt) revealed by high-definition geophysical imagery. *Mar. Geol., 275* (1/4), 1–19.

Dupuis, M., Imbert, P., Odonne, F., Vendeville, B. (2019). Mud volcanism by repeated roof collapse: 3D architecture and evolution of a mud volcano cluster offshore Nigeria, *Marine and Petroleum Geology, 110*, 368–387.

Etiope, G. (2009), Natural emissions of methane from geological seepage in Europe, *Atmos. Environ., 43*, 1430–1443.

Etiope, G., and Klusman, R. W. (2002), Geologic emissions of methane to the atmosphere, *Chemosphere*, *49*, 777–778.

Etiope, G., T. Fridriksson, F. Italiano, W. Winiwarter, and J. Theloke (2007), Natural emissions of methane from geothermal and volcanic sources in Europe, J. Volcanol. Geotherm. Res., *165*, 76 –86.

Etiope G., Feyzullayev A., Baciu C. L. (2009a). Terrestrial methane seeps and mud volcanoes: a global perspective of gas origin. Mar. Pet. Geol., *26*, 333–344.

Etiope, G., Feyzullayev, A., Milkov, A.V., Waseda, A., Mizobe, K., Sun, C.H. (2009b). Evidence of subsurface anaerobic biodegradation of hydrocarbons and potential secondar methanogenesis in terrestrial mud volcanoes. Mar. Pet. Geol., *26*, 1692–1703.

Etiope, G. and Sherwood Lollar, B. (2013). Abiotic methane on Earth, Rev. *Geophys., 51,* 276-299.

Etiope, G. and Schwietzke, S. (2019). Global geological methane emissions: An update of top-down and bottom-up estimates. *Elem Sci Anth, 7* (47). https://doi.org/10.1525/elementa.383

Evans, R. J., Stewart, S. A., and Davies, R. J. (2008). The structure and formation of mud volcano summit calderas, *Journal of the Geological Society*, *165*, 769-780. https://doi.org/10.1144/0016-76492007-118

Ferretti, O., Manfredi, Frattarelli, F. M. (1993). Caratterizzazione granulometrica e mineralogica dei sedimenti marini superficiali tra l'isola d'Elba e l'Argentario (Tirreno settentrionale). In: Arcipelago toscano: studio oceanografico, sedimentologico, geochimico e biologico. ENEA, serie Studi ambientali: 171-184.

Ferretti, R., Caccia, M., Coltorti, M., Ivaldi, R. (2021). New Approaches for the Observation of Transient Phenomena in Critical Marine Environment, *J. Mar. Sci. Eng., 9*, 578.

Feseker, T., Boetius A., Wenzhöfer, F., Blandin, J., Olu, K., Yoerger, D.R., Camilli, R., German, C.R., de Beer, D. (2014). Eruption of a deep-sea mud volcano triggers rapid sediment movement. *Nat Commun., 5*, 5385.

Foucher, J.-P., Dupré, S., Scalabrin, C., Feseker, T., Harmegnies, F., Nouzé, H. (2010). Changes in seabed morphology, mud temperature and free gas venting at the Håkon Mosby mud volcano, offshore northern Norway, over the time period 2003–2006, *Geo-Marine Letters, 30* (3-4), 157-167.

Fukushima, Y., Mori, J., Hashimoto, M., Kano, Y. (2009). Subsidence associated with the LUSI mud eruption, East Java, investigated by SAR interferometry, *Marine and Petroleum Geology*, *26*, 1740–1750.

Fusi N., Kenyon N. H. (1996). Distribution of mud diapirism and other geological structures from long-range sidescan sonar (GLORIA) data, in the Eastern Mediterranean Sea. *Mar. Geol.*, *132*, 21–38.

Galindo-Zaldivar, J., Nieto, L., and Woodside, J. (1996). Structural features of mud volcanoes and the fold system of the Mediterranean Ridge, south of Crete, *Marine Geology*, 132, 95-112.

Garcias-Bonet, N. and Duarte, C. M. (2017). Methane production by seagrass ecosystems in the Red Sea. *Frontiers in Marine Science, 4*, 340.

GeoThopica. Banca Nazionale dei Dati Geotermici a cura del CNR – Istituto di Geoscienze e Georisorse ed in collaborazione con ENI S.p.A. http://palici.igg.cnr.it/wm_geothopica/map.phtml?winsize=large&language=it&config= (Accessed 12 november 2023).

Gutsalo L. K., Plotnikov A. M. (1981). Carbon isotopic composition in the CH4-CO2 system as a criterion for the origin of methane and carbon dioxide in Earth natural gases (in Russian). Doklady Akademii Nauk SSSR, 259, 470–473.

Head, I. M., Jones, M., Larter, S. (2003). Biological activity in the deep subsurface and the origin of heavy oil, *Nature, 426*, 344–352.

Hiruta, A. and Matsumoto, R. (2023). Seafloor activity and deep-subsurface geology of gas hydrate areas revealed from δ13C of methane-derived authigenic carbonates along the eastern margin of the Sea of Japan, *Marine Geology, 464*, 107124.

Horsfield, B., Schenk, H. J., Zink, K., Ondrak, R., Dieckmann, V., Kallmeyer, J., Mangelsdorf, K., di Primio, R., Wilkes, H., Parkes, R. J., Fry, J., Cragg, B. (2006). Living microbial ecosystems within the active zone of catagenesis: implications for feeding the deep biosphere, *Earth Planet Sci. Lett., 246*, 55–69.

Hovland, M. (2002). On the self-sealing nature of marine seeps, *Continental Shelf Research*, *22*, (16), 2387-2394. https://doi.org/10.1016/S0278-4343(02)00063-8

Huguen, C., Mascle, J., Chaumillon, E., Kopf, A.,Woodside, J., Zitter, T. (2004). Structural setting and tectonic control of Mud Volcanoes in the central Mediterranean Ridge (Eastern Mediterranean). *Mar. Geol., 209*, 245–263.

HYDRA Institut für Meereswissenschaften, Affrichella Mudvolcano HYDRA Expedition 2011. 25 March 2017. (Video file). http://www.youtube.com/watch?v=SG5JzRqWWHc (15/10/2023)

Ivanov, M. K., Limonov, A. F., and van Weering, T. C. E. (1996). Comparative characteristics of the Black Sea and Mediterranean Ridge mud volcanoes, *Marine Geology*, *132*, 253-271.

Judd, A. (2004). Natural seabed gas seeps as sources of atmospheric methane. *Environ. Geol.*, *46*, 988–996.

Keller, J. V. A. and Coward, M. P. (1996). The structure and evolution of the Northern Tyrrhenian Sea. *Geological Magazine, 133* (1), 1-16.

Kim, J.-H., Torres, M. E., Choi, J.Y., Bahk, J.J., Park, M.H., Hong, W.L. (2012). Inferences on gas transport based on molecular and isotopic signatures of gases at acoustic chimneys and background sites in the Ulleung Basin. *Org. Geochem., 43*, 26–38.

Kirkham, C., Cartwright, J., Hermanrud, C., Jebsen, C. (2017). The spatial, temporal and volumetric analysis of a large mud volcano province within the Eastern Mediterranean, *Marine and Petroleum Geology, 81*,1-16

Kirschke, S., Bousquet, P., Ciais, P., Saunois, M., Canadell, J. G., Dlugokencky, E. J., et al. (2013). Three decades of global methane sources and sinks. *Nat. Geosci., 6*, 813–823

Kopf, A. J. (1999). Fate of sediment during plate convergence at the Mediterranean Ridge accretionary complex: volume balance of mud extrusion versus subduction and/or accretion, *Geology*, *27*, (1), 87-30.

Krylov, A. A., Ananiev A. R., Chernykh, D. V., Alekseev, D. A., Balikhin, E. I., Dmitrevsky, N. N., et al. (2023). Complex of Marine Geophysical Methods for Studying Gas Emission Process on the Arctic Shelf. *Sensors, 23* (8), 3872. https://doi.org/10.3390/s23083872

Kusumoto, S., Hamamoto, T., Fukuda, Y., Takahashi, A. (2015). Vertical movements of the Murono mud volcano in Japan caused by the Naganoken Kamishiro Fault Earthquake in 2014, *Earth, Planets and Space,* 67-53.

Larter, S. R., Head, I. M., Huang, H., Bennett, B., Jones, M., Aplin, A. C., Murray, A., Erdmann, M., Wilhelms, A., di Primio, R. (2005). Biodegradation, gas destruction and methane generation in deep subsurface petroleum reservoirs: an overview. In: Dore AG, Vining B (eds) Petroleum geology: Northwest Europe and global perspectives: proceedings of the 6th petroleum geology conference. Geological Society, London, pp 633–640

Lazzarotto, A., Liotta, D., Pascucci, V. and Torelli, L. (1995). Le sequenze sedimentarie Neogenico-Quaternarie nella Piattaforma del Tirreno Settentrionale. *Studi Geologici Camerti, speciale volume 1*, 499-507.

Loher, M., Pape, T., Marcon, Y., R¨omer, M., Wintersteller, P., Praeg, D., Torres, M., Sahling, H., Bohrmann, G. (2018a). Mud extrusion and ring-fault gas seepage – upward branching fluid discharge at a deep-sea mud volcano. *Sci. Rep., 8*, 6275.

Loher, M, Marcon, Y, Pape, T, Römer, M, Wintersteller, P, dos Santos Ferreira, C, Praeg, D, Torres, M, Sahling, H and Bohrmann, G. (2018b). Seafloor sealing, doming, and collapse associated with gas seeps and authigenic carbonate structures at Venere mud volcano, Central Mediterranean. *Deep Sea Research Part I: Oceanographic Research Papers*, 137. 76-96. https://doi.org/10.1016/j.dsr.2018.04.006

Loher, M., Ceramicola, S., Wintersteller, P., Meinecke, G., Sahling, H., Bohrmann, G. (2018c). Mud Volcanism in a Canyon: Morphodynamic Evolution of the Active Venere Mud Volcano and Its Interplay With Squillace Canyon, Central Mediterranean, *Geochemistry, Geophysics, Geosystems, 19*, 356–378. https://doi.org/10.1002/2017GC007166

Lykousis, V., Alexandri, S., Woodside, J., de Lange, G., Dählmann, A., Perissoratis, C., Heeschen, K., Ioakim, C., Sakellariou, D., Nomikou, P., Rousakis, G., Casas, D., Ballas, D., Ercilla, G. (2009). Mud volcanoes and gas hydrates in the Anaximander mountains (Eastern Mediterranean Sea). *Mar. Petrol. Geol., 26*, 854–872.

Mamyrin, B.A., Tolstikhin, I.N. (1984). Helium Isotopes in Nature, Elsevier, New York, p. 273.

Mabry, J., Lan, T., Burnard, P., Marty, B. (2013). High-precision helium isotope measurements in air, *J. Anal. Atom. Spectrom., 28*, 1903. https://doi.org/10.1039/c3ja50155h

Madigan, M., Martinko, J., Bende,r K., Buckley, D., Stahl, D. (2015). Brock biology of microorganisms (p. 1030). Harlow: Pearson Education Limited.

Mahlstedt, N. (2020). Thermogenic Formation of Hydrocarbons in Sedimentary Basins. In H. Wilkes (ed.), Hydrocarbons, Oils and Lipids: Diversity, Origin, Chemistry and Fate, Handbook of Hydrocarbon and Lipid Microbiology, Springer, Cham., 493-522.

Mascle, J., Mary, F., Praeg, D., Brosolo, L., Camera, L., Ceramicola, S., Dupré, S. (2014). Distribution and geological control of mud volcanoes and other fluid/free gas seepage features in the Mediterranean Sea and nearby Gulf of Cadiz. *Geo-Marine Letters, 34* (2-3), 89-110.

Mauffret, A., Contrucci, I., Brunet, C. (1999). Structural evolution of the Northern Tyrrhenian Sea from new seismic data. *Mar. Petrol. Geol., 16*, 381–407.

Mazzini, A. and Etiope, G. (2017). Mud volcanism: an updated review. *Earth-Science Reviews, 168*, 81-112.

Mazzini A., Ivanov M. K., Parnell J., Stadnitskaia A., Cronin B.T., Poludetkina E., Mazurenko L., van Weering T.C.E. (2004). Methane-related authigenic carbonates from the Black Sea: geochemical characterisation and relation to seeping fluids. *Marine Geology, 212*, 153– 181.

Mazzini, A., Svensen, H., Planke, S., Guliyev, I., Akhmanov, G. G., Fallik, T., and Banks, D. (2009). When mud volcanoes sleep: Insight from seep geochemistry at the Dashgil mud volcano, Azerbaijan, *Marine and Petroleum Geology*, *26*, (9), 1704-1715. https://doi.org/10.1016/j.marpetgeo.2008.11.003

Mazzini, A., Akhmanov, G., Mangac, M., Sciarra, A., Huseynova, A., Huseynov, A., Guliyev, I. (2021). Explosive mud volcano eruptions and rafting of mud breccia blocks, *Earth and Planetary Science Letters*, *555*, 116699.

Mazurenko, L. L., Soloviev, V. A., Belenkaya, I., Ivanov, M. K., Pinheiro, L. M. (2002). Mud volcano gas hydrates in the Gulf of Cadiz. *Terra Nova*, *14* (5), 321–329.

Meister, P., Wiedling, J., Lott, C., Bach, W., Kuhfuß, H., Wegener, G., Böttcher, M. E., Deusner, C., Lichtschlag, A., Bernasconi, S. M., Weber, M. (2018). Anaerobic methane oxidation inducing carbonate precipitation at abiogenic methane seeps in the Tuscan Archipelago (Italy), *PLoS One, 13.*

Mellors, R., Kilb, D., Aliyev, A., Gasanov, A., Yetirmishli, G. (2007). Correlations between earthquakes and large mud volcano eruptions. *J. Geophys. Res., 112*. https://doi.org/10.1029/2006JB004489

Milkov, A.V. (2000). Worldwide distribution of submarine mud volcanoes and associated gas hydrates. *Mar. Geol. 167*, 29–42.

Milkov, A.V. (2020). Secondary microbial gas. In: Wilkes, H. (Ed.), Hydrocarbons, Oils and Lipids: Diversity, Origin, Chemistry and Fate. Handbook of Hydrocarbon and Lipid Microbiology. Springer, Cham., 613-622.

Milkov, A.V., Sassen, R., Apanasovich, T.V., Dadashev, F.G. (2003). Global gas flux from mud volcanoes: a significant source of fossil methane in the atmosphere and the ocean. *Geophys. Res. Lett., 30* (2), 1037.

Milkov, A.V. and Etiope, G. (2018). Revised genetic diagrams for natural gases based on a global dataset of >20,000 samples*. Org. Geochem., 125*, 109–120.

Motteran, G. and Ventura G. (2005). Aspetti geologici, morfologici e ambientali dello scoglio d'africa (arcipelago toscano): nota preliminare. *Atti Soc. tosc. Sci. nat., Mem., Serie A*, *110*, 51-60.

Naudts, L., Greinert, J., Artemov, Y., Beaubien, S. E., Borowski, C., and Batist, M. D. (2008). Anomalous sea-floor backscatter patterns in methane venting areas, Dnepr paleo-delta, NW Black Sea, *Marine Geology*, *251* (3-4), 253-267.

Naudts, L., Greinert, J., Poort, J., Belza, J., Vangampelaere, E., Boone, D., Linke, P., Henriet, J.-P., and De Batist, M. (2010). Active venting sites on the gas-hydrate-bearing Hikurangi Margin, off New Zealand: Diffusive- versus bubble-released methane, *Marine Geology*, *272* (1-4), 233-250. https://doi.org/10.1016/j.margeo.2009.08.002

Neurauter, T. W., and Bryant, W. R. (1990). Seismic Expression of Sedimentary Volcanism on the Continental-Slope, Northern Gulf-of-Mexico, *Geo-Marine Letters*, *10*, (4), 225-231. https://doi.org/10.1007/Bf02431069

Niemann, H., Boetius, A., 2010. Mud volcanoes. In: Timmis, K.M. (Ed.), Handbook of Hydrocarbon and Lipid Microbiology. Springer, Berlin Heidelberg, pp. 205–214.

Oremland, R. S. (1975). Methane production in shallow-water, tropical marine sediments. *Appl. Microbiol., 30*, 602–608.

Pandeli, E., Principi G., Bortolotti V., Benvenuti M., Fazzuoli M., Dini A., Fanucci F., Menna F., Nirta G. (2013). The Elba Island: an intriguing geological puzzle in the Northern Thyrrenian Sea. *Geological Field Trips,* 5 (2.1).

Pascucci, V., Merlini S., Martini I. P. (1999). Seismic stratigraphy of the Miocene-Pleistocene sedimentary basins of the northern Tyrrhenian Sea and western Tuscany (Italy). *Basin Research, 11*, 337-356.

Perez-Garcia, C., Feseker, T., Mienert, J., Berndt, C. (2009). The Håkon Mosby mud volcano: 330000 years of focused fluid flow activity at the SW Barents Sea slope. *Marine Geology*, *262*, 105–115.

Prior, D. B., Doyle, E. H., and Kaluza, M. J. (1989). Evidence for Sediment Eruption on Deep-Sea Floor, Gulf of Mexico. *Science*, *243*, (4890), 517-519. https://doi.org/10.1126/science.243.4890.517

Puma Petroleum (2007). Rapporto ambientale. Permesso di ricerca per idrocarburi d91 E.R.PU (28/10/2023) https://va.mite.gov.it/File/Documento/6451

Römer, M., Sahling, H., Pape, T., Ferreira, C. D., Wenzhofer, F., Boetius, A., and Bohrmann, G. (2014). Methane fluxes and carbonate deposits at a cold seep area of the Central Nile Deep Sea Fan, Eastern Mediterranean Sea, *Marine Geology*, *347* (0), 27-42. https://doi.org/10.1016/j.margeo.2013.10.011

Rosentreter, J. A. et al. (2021). Half of global methane emissions come from highly variable aquatic ecosystem sources, *Nat. Geosci. 14*, 225–230.

Sánchez-Guillamón, O., Palomino, D., Vázquez, J. T., León, R., Fernández-Puga, M. C., López-González, N., Medialdea, T., Fernández-Salas, L. M., Somoza, L. (2023). Morpho-sedimentary structure of new mud volcanoes on the Moroccan Atlantic continental margin (Gulf of Cadiz), *Marine and Petroleum Geology*, *148*, 106031. https://doi.org/10.1016/j.marpetgeo.2022.106031

Sano, Y., Wakita, H. (1985). Geographical distribution of 3He/4He ratios in Japan: implications for arc tectonics and incipient magmatism, *J. Geophys. Res., 90*, 8729–8741.

Sano, Y., Tokutake, T., Takahata, N. (2008). Accurate measurement of atmospheric helium isotopes. *Anal. Sci., 24*, 521–525.

Saroni, A. (2019). Shallow water methane seep in the Tuscan Archipelago: acoustic, petrographic and geochemical investigation of a mud volcano. Tesi di Laurea Magistrale in scienze geologiche, georisorse e territorio, Università degli Studi di Ferrara.

Saroni, A., Sciarra, A., Grassa, F., Eich, A., Weber, M., Lott, C., Ferretti, G., Ivaldi, R., Coltorti, M. (2020). Shallow submarine mud volcano in the northern Tyrrhenian sea, Italy. *Applied Geochemistry, 122*, 104722. https://doi.org/10.1016/j.apgeochem.2020.104722

Saunois, M. et al. (2016). The Global Methane Budget: 2000-2012, *Earth Syst. Sci. Data Discuss.* https://doi.org/10.5194/essd-2016-25

Sautkin, A., Talukder, A. R., Comas, M. C., Soto, J. I., Alekseev, A. (2003). Mud volcanoes in the Alboran Sea: evidence from micropaleontological and geophysical data. *Mar. Geol., 195*, 237–261.

Schoell, M., 1983. Genetic characterization of natural gases. *Am. Assoc. Petrol. Geol. Bull. 67*, 2225–2238.

Schoell, M. (1988). Multiple origins of methane in the Earth. *Chem. Geol. Orig. Methane Earth, 71*, 1–10.

Schorn, S., Ahmerkampa, S., Bullocka, E., Weberb, M., Lott, C., Liebekec, M., Lavika, G., Kuypersa. M. M., Grafa; J. S., Miluckaa, J. (2022), Diverse methylotrophic methanogenic archaea cause high methane emissions from seagrass meadows,

Proceedings of the National Academy of Sciences, 119 (9). https://doi.org/10.1073/pnas.2106628119

Sciarra, A., Saroni, A., Etiope, G., Coltorti, M., Mazzarini, F., Lott, C., Grassa, F., Italiano, F., (2019). Shallow water submarine seep of abiotic methane from serpentinized peridotites off the Island of Elba, Italy, *Appl. Geochem., 100*, 1–7.

Spatola, D., Casalbore, D., Pierdomenico, M., Conti, A., Bigi, S., Ingrassia, M., Ivaldi, R., Demarte, M., Napoli, S., Chiocci, F. L. (2022). Seafloor characterisation of the offshore sector around Scoglio d'Affrica islet (Tuscan Archipelago, northern Tyrrhenian sea), *Journal of Maps*. https://doi.org/10.1080/17445647.2022.2120836

Turner, A. J., Frankenberg, C., Wennberg, P. O., and Jacob, D. J. (2017). Ambiguity in the causes for decadal trends in atmospheric methane and hydroxyl. *Proc. Nat. Acad. Sci. U.S.A. 114*, 5367–5372.

Vandorpe, T., Martins, I., Vitorino, J., Hebbeln, D., Garcia, M., and Van Rooij, D. (2016). Bottom currents and their influence on the sedimentation pattern in the El Arraiche mud volcano province, southern Gulf of Cadiz, *Marine Geology*, *378*, 114-126. https://doi.org/10.1016/j.margeo.2015.11.012

Van Rensbergen, P., Hillis, R. R., Maltman, A. J., and Morley, C. K. (2003). Subsurface sediment mobilization: introduction, *Geological Society, London, Special Publications*, *216*, 1-8. https://doi.org/10.1144/Gsl.Sp.2003.216.01.01

Volgin A. V., Woodside J. M. (1996). Sidescan sonar images of mud volcanoes from the Mediterranean Ridge: possible causes of variations in backscatter intensity. *Mar. Geol., 132*, 39–53.

Wallmann, K., Drews, M., Aloisi, G., and Bohrmann, G. (2006). Methane discharge into the Black Sea and the global ocean via fluid flow through submarine mud volcanoes, *Earth and Planetary Science Letters*, *248*, (1-2), 545-560. https://doi.org/10.1016/j.epsl.2006.06.026

Weber, T., Wiseman, N. A., Kock, A. (2019). Global ocean methane emissions dominated by shallow coastal waters, *Nature Communications, 10*, 4584. https://doi.org/10.1038/s41467-019-12541-7

Whiticar, M. J., Faber, E., Schoell, M., 1986. Biogenic methane formation in marine and freshwater environments: CO_2 reduction vs. acetate fermentation — isotope

evidence. *Geochem. Cosmochim. Acta 50*, 693–709. https://doi.org/10.1016/0016-7037(86)90346-7

Whiticar, M. J. (1994). Correlation of natural gases with their source. In: Magoon, L., Dow, W. (eds). The petroleum system: from source to trap. AAPG Memoir. The American Association of Petroleum Geologists, Tulsa, 261–283.

Woolsey, T. S., McCallum, M. E., & Schumm, S. A. (1975). Modeling of diatreme emplacement by fluidization. In Physics and Chemistry of the Earth, 29–42. Pergamon Press. https://doi.org/10.1016/B978-0-08-018017-5.50007-9

Yassir, N. (1987). Mud volcanoes: evidence of neotectonic activity. In: Memoir of the Geological Society of China, 9, pp. 513–524.

Zeikus, J. G. (1977). The biology of methanogenic bacteria. *Bacteriol. Rev., 41*, 514–541.